2021

Influence of ECM Composition and Intracellular Calcium on Endothelial Biomechanics and Prediction of Cellular Stresses Using Machine Learning

Vignesh Aravind Subramanian Balachandar
University of Central Florida

STARS Citation

Subramanian Balachandar, Vignesh Aravind, "Influence of ECM Composition and Intracellular Calcium on Endothelial Biomechanics and Prediction of Cellular Stresses Using Machine Learning" (2021). *Electronic Theses and Dissertations, 2020-*. 769.
https://stars.library.ucf.edu/etd2020/769

INFLUENCE OF ECM COMPOSITION AND INTRACELLULAR CALCIUM ON ENDOTHELIAL BIOMECHANICS AND PREDICTION OF CELLULAR STRESSES USING MACHINE LEARNING

by

VIGNESHARAVIND SUBRAMANIANBALACHANDAR
BE ANNA UNIVERSITY 2015
MS UNIVERSITY OF CENTRAL FLORIDA 2017

A dissertation submitted in partial fulfilment of the requirements
for the degree of Doctor of Philosophy
in the Department of Mechanical and Aerospace Engineering
in the College of Engineering and Computer Science
at the University of Central Florida
Orlando, Florida

Summer Term
2021

Major Professor: Robert L. Steward Jr.

ABSTRACT

Endothelial cells, which form the inner layer of the vasculature, constantly interact with their external microenvironment called the extracellular matrix (ECM) by exerting contractile cell-substrate stresses called tractions and cell-cell stresses called intercellular stresses. This cellular mechanosensing can become aberrant and act as a precursor for many vascular pathological and physiological processes such as cancer metastasis, atherosclerosis, cell differentiation, migration, and morphogenesis. Also, intracellular calcium signalling plays an important role in endothelial cell motility and in maintaining vascular tone. Alteration in ECM composition has been linked to several pathologies, in fact, a transition to a fibronectin-rich matrix from a type I collagen-rich and elastin-rich matrix in coronary artery disease, for example. However, the influence of ECM compositions and intracellular calcium levels on cell mechanics is not clearly understood. The first study will shed light on ECM composition and its influence on endothelial mechanical properties including traction, intercellular stresses, cell velocity, and various morphological parameters. The second study will enhance our knowledge on the role calcium signaling plays on cellular tractions. The final chapters will focus on the development and utilization of Machine Learning (ML) models for the predictions of tractions and intercellular stresses with morphological and pharmacological predictors, which to our knowledge is the first work in the field. The results yielded from this work will further our understanding of cellular mechanics at the mesoscale by: i) Identifying the role of specific ECM molecules in mechanical signaling, ii) Understanding the influence of transient calcium signaling on tractions, and iii) Providing a machine learning framework that can be used for the prediction of tractions and intercellular stresses as a dose dependent response to a drug that is known to influence cell mechanics. These findings will be beneficial to drug development studies and targeted drug therapy for treating various vascular-related pathologies.

I dedicate this dissertation in memory of my beloved childhood friend Raam Gautham. Thank you for being a faithful, caring, and supportive friend all these years. You will be forever in our hearts.

ACKNOWLEDGMENTS

I express my deepest gratitude to my advisor Dr. Robert L. Steward Jr. for all the guidance and support. I sincerely thank you for your knowledge, expertise, and constant motivation without which this work would not have been possible. I extend my thanks to Dr. Luigi Perotti, Dr. Dazhong Wu, and Dr. Ellen Kang for being a part of my dissertation committee.

I would also like to thank my lab mates Jingwen Wu, Sean Beverung, Dilshan Ranadewa, and Bradley Mooney for all the knowledge, help, and support. A special thanks to Miku for allowing me to use his experimental data for the Machine Learning project and Todd Condon Jr., for helping me with the calcium experiments.

I want to thank my mother Santha Balachandar for being a pillar of strength of my life, getting me through difficult times, and for all the sacrifices and love. I would also like to thank my father Balachandar, sister Iswarya Balachandar, family, and friends for their continuous love, support, and motivation all these years.

This work was supported by the University of Central Florida start-up funds, and the National Heart, Lung, And Blood Institute of the National Institute of Health under award K25HL132098, and NSF CAREER award 2045750.

TABLE OF CONTENTS

LIST OF FIGURES

LIST OF TABLES

CHAPTER ONE: INTRODUCTION

Blood vessels are made up of layers of endothelial cells (EC), Extra Cellular Matrix (ECM), and smooth muscle cells separated by elastic membranes. ECM including type IV collagen, Fibronectin (FN), and laminin are found in the outer layer (tunica externa or adventitia) and type I Collagen (Col I) & elastin are found in the inner layer (tunica intima) of the blood vessel respectively [1-3]. The variation in ECM composition could play a role in biological and pathological processes like morphogenesis, angiogenesis, and atherosclerosis. Col I and elastin accounts for 50% of the dry weight of a blood vessel [4]. FN enriched matrix developed during lesion development due to smoking, lifestyle, or aging, for example, promotes atherogenesis and reduces endothelial permeability [5]. The endothelium layer of the blood vessel is constantly under mechanical shear stresses due to blood flow. EC present in the blood vessel respond to mechanical shear stress and strain. The stresses and strains on the blood vessel produce a cycle of numerous biochemical pathways at the subcellular level. It has been shown that wall shear stress (due to axial blood flow) and circumferential stretch (attributed to pulsatile flow) trigger many common biochemical pathways which regulate vasoactive molecules like nitric oxide (NO), prostacyclin (PGI_2), (vasodilators), and endothelin-1 (ET-1, vasoconstrictor) [6, 7]. Release of vasoactive hormones, chemokines, cytokines, growth factors, reactive oxygen species, and antibiotic peptides as a response to infection, injury, smoking, stress, aging, hyperglycemia, etc. can regulate the ECM composition by activating matrix metalloproteinases and intracellular calcium levels leading to dysfunctional endothelial mechanics resulting in cardiovascular diseases such as coronary artery disease (CAD) and heart failure [8-10].

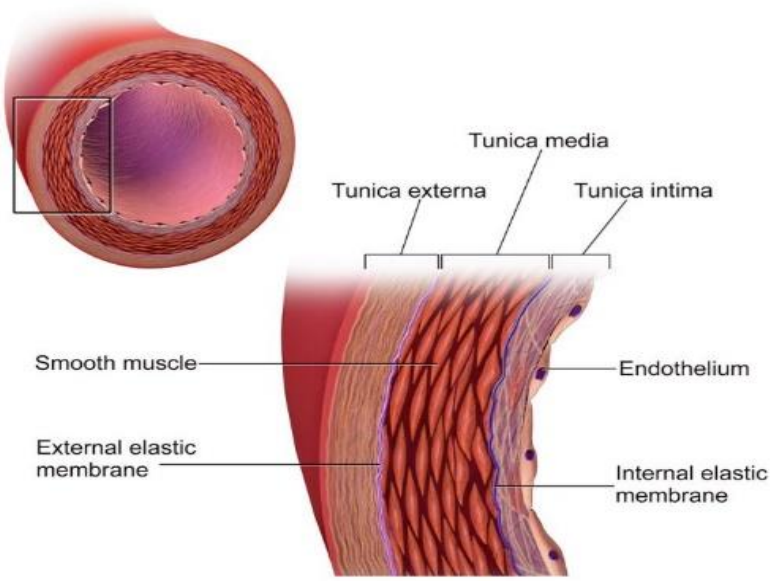

Figure 1: Cross-section of a blood vessel with inner endothelium layer [11]

Shear stresses also increased intracellular Ca^{2+} in endothelial cells impairment of which could affect the vascular tone, vascular remodeling, and vasodilation [12]. The link between endothelial contractile forces, intercellular (cell-cell) forces and microenvironmental factors such as ECM composition, substrate stiffness, thickness, density, porosity, etc. has not been completely understood. The endogenous contractile force response translated as traction stresses on the substrate is sensitive to ECM properties, biochemistry, and external mechanical signals which are currently being studied to understand basic biological processes and disease proliferation. The mechanics of the endothelial monolayer at the mesoscale is also nebulous. Group of cells in contact with each other behave like a collective unit and their dynamics are also altered by ECM properties, monolayer geometry, and bio-chemicals or drugs. Monolayer mechanics study is important in understanding the mechanics of cancer invasion where cells display significantly higher velocity and tractions even at lower stiffnesses [13]. ECM stiffness is altered during the development of cardiac diseases, asthma, or cancer. In vitro experiments of cell, mechanics can help understand the role of proteins, biochemical pathways, and cell cortex in mechanosensing and collective behavior.

Disease propagation through disruption of endothelial (cell) mechanics has not been clearly understood and the physics aspect of CVD (cardiovascular diseases) has not been extensively studied in the scientific community. Understanding mechanotransduction at the subcellular level could be key to unraveling the interplay between ECM-FA mechanosensing and other biochemical responses. Demystification of mechanical signaling could pave way for more effective and targeted drug therapy by understanding the mechanics of diseases at the molecular level [14].

Traction Force Microscopy (TFM) and Monolayer Stress Microscopy (MSM) are one of the common methods to quantify traction stresses and intercellular stresses. Although TFM, MSM, and other methods can quantify tractions and intercellular stresses very few models have been developed to predict the cell mechanics from predictors such as drug concentration, substrate stiffness, the geometry of the monolayer sheet, fluid flow rate, cell shape, curvature, spread area, circularity, etc. A model capable of encasing one or many of such predictors could be crucial to understanding the interplay between various factors associated with cell mechanics.

In this thesis, to understand the mechanics of endothelial cells at mesoscale, TFM & MSM are performed by varying ECM composition. We also developed a relationship between transient intracellular Ca^{2+} levels and tractions as a dose-dependent reaction to a known concentration of Ca^{2+} antagonist or agonist. This study is fundamental to the understanding of how cells regulate contractile forces using myosin motors. A novel machine learning (ML) based approach is proposed which has the potential to predict tractions and intercellular stresses by utilizing any of the predictors or predictors from the phase-contrast images. The predictive capability of the ML is demonstrated using two ML models: Stepwise Linear Regression (SLR) and Quadratic Support Vector Machine (QSVM) utilizing two different training sets. The first training set: Single Area Training (SAT) utilizes drug concentration, monolayer area, and monolayer perimeter as the predictors. The second training set: Multiple Area Training (MAT) uses window-based area and perimeter computed from small overlapping windows as predictors in addition to the drug concentration.

CHAPTER TWO: LITERATURE REVIEW

Mechanosensing

The living cells including endothelial cells require mechanical contractile forces generated from the cytoplasm extending to the leading edge of the cell or the lamellipodium to continuously probe the environment (substrate) which is important for migration, growth, differentiation, and morphogenesis [15]. The cells find a new anchor point and attach to the substrate's extra cellular matrix (ECM) with the help of focal adhesion proteins (FA) inside the cell and transmembrane proteins like integrin connect the anchor points of the cell to the ECM.

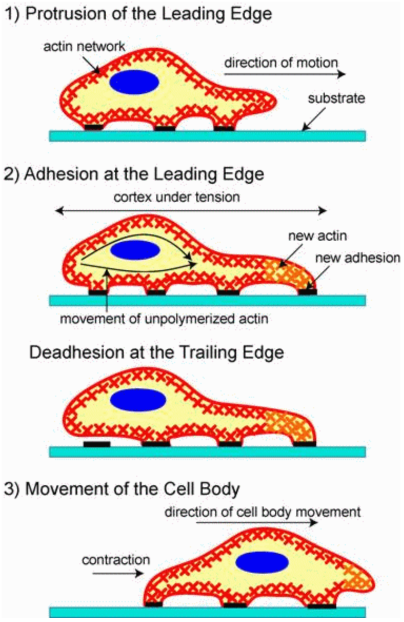

Figure 2: Cell forward movement using contractile forces and focal adhesions [16]

Although not all the contractile forces are expressed as the tractions on the surface due to dissipation of forces inside the cell due to protein slippage, disassembly, fraying, and translocation [17]. However, the tractions measured on the substrate are directly correlated to the contractile forces exerted from inside of the cell. The ability of the cell to sense mechanical cues based on conformal changes to the proteins binding to the receptors at the cell-substrate interface is termed mechanosensing. The tractions on the substrate have been used as the measure of the cell's contractile forces and captured using one of the most common techniques: Traction Force Microscopy (TFM). Although TFM is relatively easier to measure tractions it requires a lot of pre-processing like the use of fluorescent beads to estimate the displacement field in the substrate from which tractions are evaluated. The living cells also use mechanical forces to communicate with neighboring cells leading to collective pack-like behavior which is currently being investigated. The junctions between cells in a monolayer enable fast, long-distance communication [18]. Monolayer Stress Microscopy (MSM) is a widely used method to recover the local intercellular stresses with their principal stress orientations from the tractions measured by TFM. The sensitivity of cell attachment, spreading, and contractile forces to substrate stiffness have been documented in [19, 20]. The generation of endogenous forces inside the cytoskeleton of the cell is regulated by ECM properties, external forces, and binding affinity of the adhesion molecules (proteins) to the matrix ligands (receptors). Contractile actomyosin filaments modulated by polymerization and depolymerization processes bind to FA (adaptor) proteins like vinculin which are dubbed as molecular clutches that enable mechanosensing or crosstalk between ECM-cell and cell-cell interface. The contractile forces exerted by the cells on the substrate at leading and trailing edges are transferred to the neighbouring cells [21]. The cell-cell communication via mechanical signals through adherens junction (cadherins) is responsible for collective behavior observed in monolayer sheets of cells influenced by cells close to the leader cells (free edge of the moving monolayer) several rows ahead of the followers [22].

Endothelial Mechanics and Cardiovascular Diseases

Endothelial cells are very important in maintaining homeostasis, oxidative balance, and protection of vasculature through Nitric Oxide release. Abnormality in blood flow or wall compliance due to change in wall stiffness can be associated with cardiovascular diseases (CVD). Elevated ECM thickness (collagen and elastin) and wall thickness were observed after pulmonary vascular remodeling due to induced hypoxia in endothelial NO synthase (eNOS) null mice. eNOS is one of the three factors involved in the production of NO [23]. EC response to shear stress is important for the healthy functioning of the circulatory system.

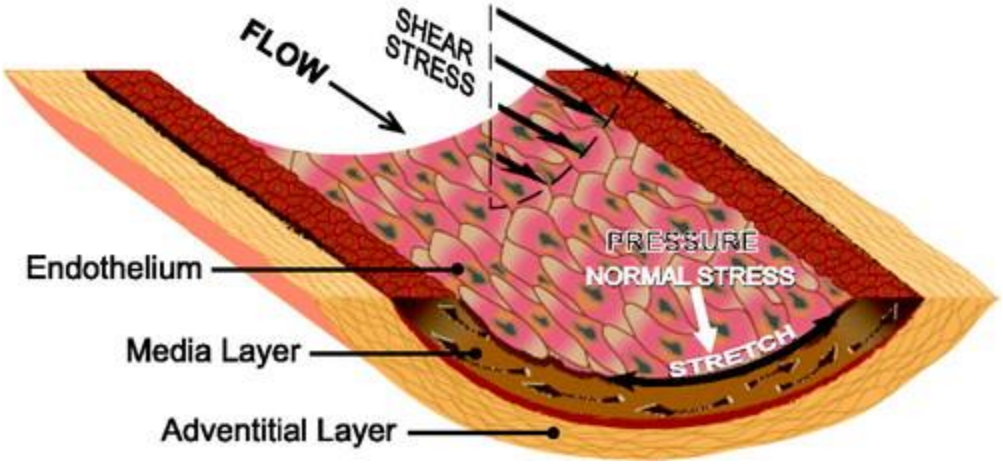

Figure 3: Cross-section of a blood vessel with inner endothelium under constant shear [3]

Anomaly in EC’s response to mechanical stresses can potentially lead to hypertension, hyperplasia, thrombosis, and atherosclerosis. Even though atherosclerosis is caused by the deposition of abnormal bold clots and low-density lipoproteins it has been observed that change in blood flow rate leading to wall and circumferential stresses enable the atherosclerosis formation at specific locations like bifurcations and anastomosis where the likelihood of vortices or turbulence are very high [7]. It has also been shown that EC alters their physical structure, function, and even gene expression based on the magnitude of shear stresses [12]. Shear stress due to blood flow-induced morphology change increased NO and thrombomodulin (known for anti-thrombotic properties) levels, decrease in VCAM-1 (Vascular Cell Adhesion Molecule) and mRNA while promoting differentiation of embryonic stem cells (ES) into EC type. According to [12] roughly 3% of genes responded to shear stress which corresponds to more than 600 endothelial genes. EC's response to shear forces is also linked to angiogenesis and abnormality in the process is a trademark indicator of cancer cells [12]. In vitro experiments showed glioma stem-like cancer cells endothelial migration and tube formation with elevated levels of vascular endothelial growth factor (VEGF) [24].

Mechanics of Cell Monolayers

Studying the mechanics of the collective behavior of cells is important to understand the functioning of various biological processes like morphogenesis, tissue repair, and cancer metastasis. There are various factors that are known to contribute to this collective behavior. A series of cells in a locality could be driven by the movement of leader cells or cells closed to the leader cells [22]. The movement of human umbilical vein endothelial cell (HUVEC) monolayer sheet can be influenced by stiffness gradient (durotaxis), local maximum principal stress orientation (plithotaxis), or collective drive towards unfilled space (kenotaxis) [25]. This collective motion of monolayer sheet of cells through mechanosensing is termed mechanotaxis in general.

The cell-cell normal and shear stresses recovered from the tractions through monolayer stress microscopy (MSM) provide a visual stress map of the monolayer under study. The contractile forces exerted by the cells on the ECM coated on the substrate are communicated across the monolayer through cell-cell junctions. Cell-cell forces and cell-ECM forces engage in a tug of war which should balance each other according to Newton's third law. MSM approximates the monolayer to a thin elastic plate and the intercellular stresses are solved for using a chosen elastic modulus and Poisson's ratio of the sheet that mimics biological condition and the tractions from TFM. The domination of various factors like stiffness, shear stresses, local tractions, monolayer geometry, local stress orientations, etc. on the collective cell mechanics are widely studied. The complex interplay between these factors and cell mechanics is not yet fully understood. The tractions and intercellular stresses from the monolayer are constantly regulated because of the changes in the environment like ECM thickness, stiffness, presence of external forces, etc. The dynamics of the confined monolayer are different compared to an expanding monolayer [26]. It has been reported that the competition between the cell-ECM traction forces and cell-cell forces influences the physical property of the entire monolayer sheet. The domination of one force over the other leads to a phenomenon called 'cell-jamming' where the monolayer transitions from fluid (viscoelastic) to solid-like state retaining its elastic properties as assumed in MSM [27]. Different types of collective monolayer studies can shed light on physics behind processes like cell migration, cell division, wound healing etc.

Role of ECM in Mechanobiology

ECM, which is composed of various proteins and proteoglycans, forms the underlying structure that supports the cell sheets and separates them from the connective tissue and other cell types known as the basement membrane and also provides the three-dimensional scaffolding between the cells termed as interstitial matrix [28]. The cell-ECM interaction is sensitive to external forces or stimuli. Examples include piloerector and other mechanoreceptor responses. The local changes in the conformation of ECM trigger the sensory neurons like Pacinian corpuscle as in case of pain or pressure sensation [14]. The stresses exerted on the ECM are transmitted across the cells through cytoskeleton and cell-cell junctions. As mentioned, stiffness gradient in ECM influences cell migration. It is observed that change in stiffness affects the cell traction force and cell spread area [29]. The extent of interdependency between traction forces and substrate stiffness remains unclear. Studies are being done to further elucidate the relationship between ECM stiffness and tractions. It has been documented that integrin-ECM focal adhesion and cell spreading depend on stiffness with different underlying mechanosensing mechanisms once the stiffness reaches a threshold stiffness [19]. The decoupling of cells in a monolayer, as well as a cell pair, was observed due to a significant increase in stiffness above a certain threshold as mentioned [30] which could very well shed light on fluid-solid transitioning observed in a constrained cell pack.

Endothelial Calcium Signaling

[12] show that intracellular Ca^{2+} increases in a dose-dependent manner to shear stress via P2X4 through ATP activation by endothelial cells (EC). The mechanism by which the ATP is activated in

a flow-dependent manner is unclear. It was demonstrated that inhibition of endothelial ATP release & calcium influx by blocking P2X4 and PIEZ01 affected NO formation, vascular tone, and blood pressure [12, 31]. It was shown that cell movement impediment, external shear or mechanical forces, and inflammatory mediators or biochemicals like histamine and thrombin affected the intracellular calcium transient [32, 33].

[34] show that calcium signaling serves as a cell-cell communication across different directions in a HUVEC monolayer. EC consistently exchange Ca^{2+} with neighboring cells through gap junction proteins including connexin 40,43, and 37. The mechanism behind the propagation of calcium transients in different patterns and directions across the vascular systems remains unknown. It will be useful to link cell mechanics with calcium transient propagation to better understand the collective intercellular communication among EC in a monolayer sheet.

Endothelial Response to Gap Junction (Cx43) Disruption

[35] demonstrated static endothelial monolayer response upon connexin 43 disruption in vitro using high and low doses of 2,5-dihydroxychalcone (chalcone) drug. It has been observed that higher doses of chalcone significantly decreased HUVEC intercellular stresses, substrate traction stresses, cell velocities, and strain energies highlighting the contribution of Cx43 with respect to endothelial cell mechanics. Results from [35] showed that the chalcone drug significantly impacts endothelial biomechanics.

Traction Force Microscopy and Monolayer Stress Microscopy

Cell-populated collagen gel was one of the first methods that measure the traction forces by estimating the change in diameter of the gel disk and traction forces were also quantified based on wrinkles exerted by the cells on thin silicone membrane. These methods, however, suffered because of variability, lack of accuracy, and the complexity involved [36]. Micropost force sensor arrays are also being used to measure tractions of individual cells or monolayers based on deflections from the microposts [36]. A novel Förster resonance energy transfer (FRET) sensor-based approach has also been employed to measure tractions by estimating the change in excitation energy of the fluorescent protein markers that are sensitive to external forces. However, FRET sensors were not able to differentiate forces in the pN range, and force contributions from other unmarked proteins could not be quantified [37]. TFM is one of the common methods used to quantify traction stresses exerted by a single or sheet of cells on a substrate that is coated with an extracellular matrix (ECM). The method computes the tractions based on the displacement field of fluorescent microbeads localized on the top surface of the substrate. A window-based cross-correlation method was used to calculate the bead displacements based on comparison with a stress-free image of the bead configuration [38]. The challenges in TFM including experimental and computational variability, and the influence of noise in displacement data [17].

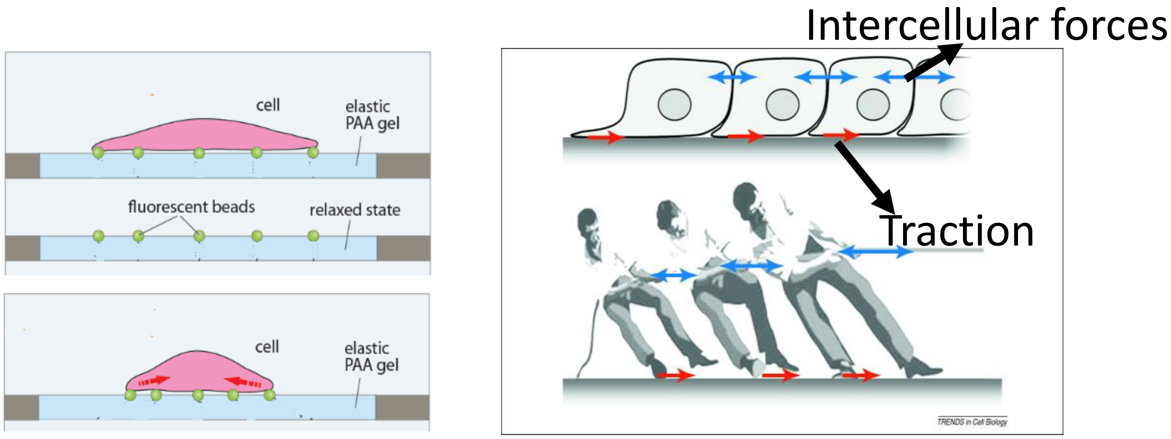

Figure 4: Schematic of traction force measurement (left) and theoretical concept of intercellular forces [39, 40]

In the MSM method, cell-cell intercellular forces were recovered from TFM tractions by assuming a monolayer sheet of cells as elastic thin plates and imposing newton’s force balance and strain compatibility equations. The effect of boundary, external noise, out-of-plane tractions & stresses, Poisson’s ratio, and elastic modulus was discussed in [41].

Predictors of Cell Mechanics

There are several external factors notably substrate stiffness, cell spread area, local cell curvature, and external forces that affect the cell mechanics including traction and intercellular stresses [42, 43]. [20, 42, 44, 45] investigated the interplay between cell shape, cell area, substrate stiffness, and traction forces. Research has also shown that traction force is also modulated by distance from the center of the cell to its perimeter and local cell curvature [42, 46]. [44] predicted traction stresses by using substrate stiffness (E) and cell area (A) as the predictors for a single EC and an EC pair. A positive correlation was observed for both stiffness and area with respect to the tractions. Contrastingly [20] reported that a larger cell spread area lowered average traction forces in human pulmonary artery endothelial cells. In addition, [42] showed that cell spread area and local curvature are better predictors of strain energy compared to the number of focal adhesions and substrate stiffness. [47] predicted traction force maps of single EC, fibroblast, and keratocyte with the first moment of area model (FMA) utilizing cell shape as the predictor. Other contour mathematical models notably the simple tension model, anisotropic tension model, tension-elasticity model, and cellular potts model provide a theoretical framework for traction forces by utilizing cell geometry [48].

More recently, Bayesian inversion stress microscopy (BISM) and Kalman inversion stress microscopy (KISM) were presented as predictive models for the internal stress field based on corresponding traction force data. BISM and KISM use experimental traction force data as likelihood function to make predictions using Bayesian statistics (Bayes' theorem). BISM can infer the internal stress field only from a single traction field image but a dimensionless regularization parameter must be calculated from the experimental data to make predictions. KISM however, is capable of estimating internal stress fields from a time-lapse of traction data (movie) with its accuracy depending on-time resolution of the traction data [49, 50].

CHAPTER THREE: RESEARCH METHODOLOGY

Traction Force Microscopy (TFM)

TFM is one of the common methods to quantify tractions or cell-ECM stresses of a single cell or a monolayer. Tractions are computed based on the displacement field of fluorescent microbeads localized on the top surface of the substrate. Butler et al., solved for the tractions from the equation $\overrightarrow{U} = \vec{K} * \vec{T}$ using Fourier Transform Traction Cytometry (FTTC) evaluated at z = 0 [38]

where,

u is the displacement field

K is the Green's function mapping traction to displacement K ($|\vec{r} - \vec{r}'|$)

* is the convolution operation

T is the traction on the surface

The inverse calculation of $\vec{T}$ from the above equation becomes easier in Butler's FTTC. The mathematical details of meshing, the integral formula for calculating displacements using Green's tensor and traction field, and Boussinesq equations depicting the Green's tensors can be found in [51]. Dembo and Wang's method requires regularization methods and smoothing functions to reduce the noise from the displacement field [51]. By contrast, Butler's FTTC can use constrained as well as unconstrained boundaries to compute the tractions based on bead displacements which require no smoothing [38]. Traction computations for cell monolayers are described in [22].

Monolayer Stress Microscopy (MSM)

MSM is used to calculate the intercellular stress components in 2-D from the tractions computed from TFM by making some assumptions. The assumptions for Boundary Conditions (BCs) and equations for calculating the intercellular stresses were described in [41]. The cell monolayers are assumed to be homogeneous, flat, and thin elastic plates. The tractions and stresses in the z-direction were assumed to be negligible (i.e., $\boldsymbol{\sigma}_{zz} = \boldsymbol{\sigma}_{zx} = \boldsymbol{\sigma}_{zy} = \mathbf{T}_z =0$) [41]. The tractions from TFM are linked to intercellular stresses using Newton's force balance in 2-D. Using the elastic assumption of the monolayer and applying Saint-Venant's compatibility relations we can get the Beltrami-Michell compatibility equation which links tractions as a function of Poisson's ratio (ν) and intercellular stresses. From Newton's stress balance, compatibility relations, and imposing BCs we can calculate the local normal and shear stresses in x and y directions. From the local stresses, the maximum and minimum principal stresses can be calculated by rotating in the direction of principal planes where the shear stresses are zero. Using the maximum and minimum principal stress orientations average normal stress and maximum shear stresses can be calculated as shown in figure 5. The computation of principal stresses is essentially an eigenvalue problem where maximum and minimum principal stresses are the eigenvalues and the orientation of the principal stresses gives the eigenvectors (direction of the eigenvalues).

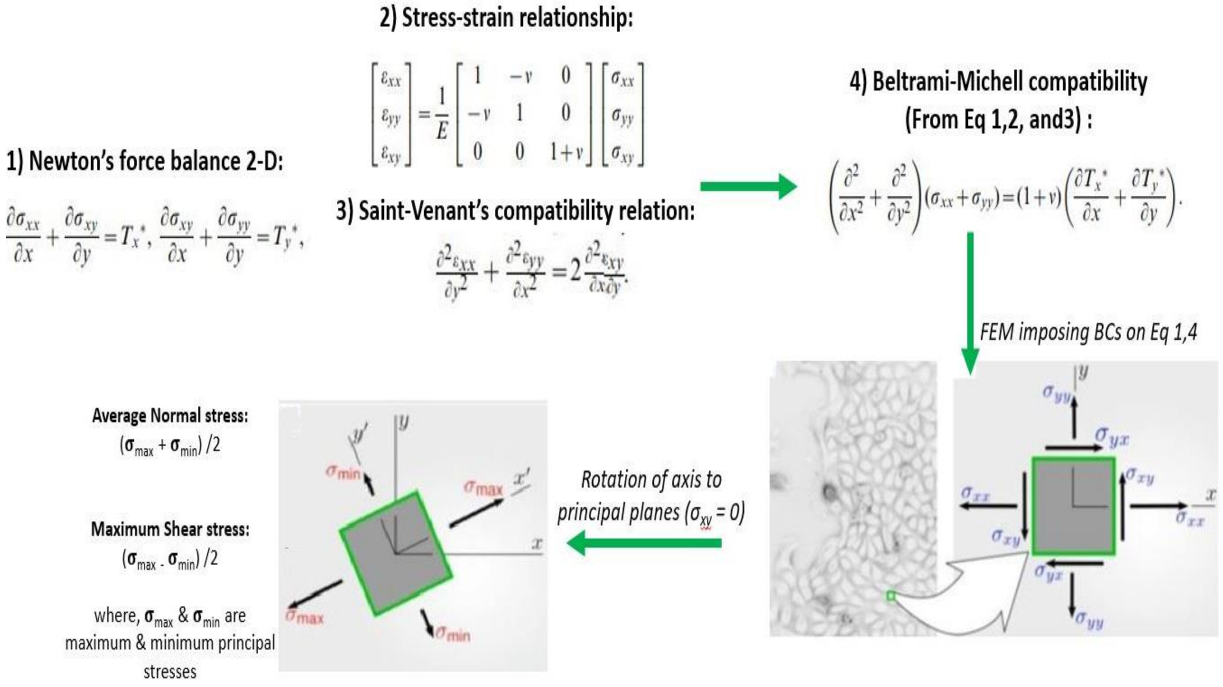

Figure 5: Mathematical depiction of intercellular stresses using MSM [41]

To sum up, the displacement fields of the fluorescent beads embedded in the elastic substrate on which the cells were attached were measured by comparing with the reference image taken at the end of the experiment by detaching the cells with trypsin 10X. Using the Particle Image Velocimetry (PIV) routine in MATLAB, the displacement fields of the beads were computed. The tractions were then recovered using TFM. The local stresses and the corresponding principal stresses were calculated using the MSM from which the average normal stress and maximum shear stresses were computed as shown in figure5.

CHAPTER FOUR: EXTRACELLULAR MATRIX COMPOSITION ALTERS ENDOTHELIAL MECHANICS

Abstract

The extracellular matrix (ECM) is the underlying scaffold that links the intima layer to the underlying media layer in the blood vessel. Endothelial cells constitute this inner blood vessel layer, and the underlying ECM is important for many physiological and pathological processes such as angiogenesis, morphogenesis, atherosclerosis, and diabetes. In fact, during plaque formation or coronary artery disease (CAD) progression the ECM composition within a blood vessel can vary over time as the native ECM contains more collagen, while the composition can transition from collagen to more of a fibronectin-rich matrix as a result of inflammatory or immunological response to lesion development due to injury, smoking, aging, or high low-density lipoprotein intake. A fibronectin-rich matrix plays an important role in atherogenesis. The ability of Human Umbilical Vein Endothelial Cells (HUVECs) and other cell types to sense mechanical cues based on conformal changes to the proteins binding to the receptors at the cell-ECM interface is termed mechanosensing. Although the ECM is well understood to influence cellular biomechanical stresses, the interplay among intercellular stresses, tractions, and ECM composition is poorly understood, especially as this ECM composition changes during some of the pathologies mentioned above. Therefore, to provide a better understanding between cell-derived mechanical forces and ECM composition we seeded HUVECs on 1.2 kPa hydrogels coated with different ratios of 0.1 mg/ml concentration of type 1 collagen (Col-I) and fibronectin (FN) and measured corresponding tractions, intercellular stresses, and morphological features such as cell area and circularity. In this study, we calculated intercellular stresses, strain energies, and

cell velocities generated by endothelial monolayers attached to hydrogels with 5 different compositions of Type 1 Col I and FN: i) 100% Col-I ii) 75% Col-I - 25% FN iii) 50% Col-I - 50% FN iv) 25% Col-I - 75% FN v) 100% FN. Our results showed that intercellular stresses, tractions, and strain energies were significantly higher for 50% Col-I- 50% FN but had the lowest cell velocities relative to all other compositions. Also, cells cultured on 50% Col-I - 50% FN composition had the highest cell area with the least average cell circularity. In comparison, endothelial cells cultured on 100% Col-I had the lowest tractions, and the highest velocities, while cells cultured on 25% Col-I and 75% had the lowest intercellular stresses. HUVECs seeded on 100% Col-I showed the smallest cell area and the highest circularity.

Introduction

ECM plays an important role in the progression of various neurological and cardiovascular pathologies. Basement membrane (a sheet on ECM deposition that supports epithelial cells) and interstitial connective matrix (matrix surrounding cells in porous 3-D space) are the two types of ECM [52]. Type IV collagen, present in the basement membrane is linked to cancer metastasis [52]. Increased deposition of ECM in airways contributes to chronic obstructive pulmonary disease [52]. In pancreatic cancer, altered collagens (Col-I), fibronectin (FN), proteoglycans, and hyaluronic acid in ECM leading to desmoplasia were reported [52]. In Alzheimer's disease, amyloid plaque formation due to amyloid-beta A4 precursor protein, and aggregation of tau protein leading to neurofibrillary tangles are linked to changes in the brain ECM components [52]. Impaired healing and wound closing are trademark characteristics of diabetes which are known to alter the protein expression and activity of the ECM [52, 53]. Diabetes is linked to increased

ECM stiffness, ECM degradation, tissue fibronectin, and decreased production of collagen and elastin fibers [53].

Blood vessels are made up of layers of Endothelial Cells (EC), Extra Cellular Matrix (ECM), and smooth muscle cells separated by elastic membranes. ECM including type IV collagen, fibronectin (FN), and laminin are found in the outer layer (tunica externa or adventitia), and type I collagen (Col I) & elastin are found in the inner layer (tunica intima) of the blood vessel respectively [1-3]. EC are very important in maintaining homeostasis, oxidative balance, and protection of vasculature through Nitric Oxide release [6]. Abnormality in blood flow or wall compliance due to change in wall stiffness can be associated with cardiovascular diseases (CVD) [23]. Elevated ECM thickness (collagen and elastin) and wall thickness were observed after pulmonary vascular remodeling due to induced hypoxia in endothelial NO synthase (eNOS) null mice [23]. eNOS is one of the three factors involved in the production of NO [23]. A transition from collagen to more of a fibronectin-rich matrix was observed during Coronary Artery Disease (CAD) progression [5]. Anomaly in EC's response to external mechanical stresses due to change in wall stiffness can potentially lead to hypertension, hyperplasia, hypercholesterolemia, thrombosis, and atherosclerosis [7].

The cell-ECM interaction is sensitive to external forces or stimuli. Examples include piloerector and other mechanoreceptor responses. The local changes in the conformation of ECM trigger the sensory neurons like the Pacinian corpuscle as in case of pain or pressure sensation [14]. ECM influences signaling between molecules, communication among neighboring cells, and individual cell behavior such as cell adhesion, growth, migration, and differentiation [52, 54]. ECM also plays a crucial role in angiogenesis and vascular morphogenesis by guiding and organizing EC into a neovessel by enabling integrin-dependent mechanical force signaling among distant EC [55]. It is observed that change in stiffness affects cell migration, traction stresses, and cell spread area [17]. It has been documented that for EC, tractions and cell spreading depend on the substrate stiffness [18]. The decoupling of cells in a monolayer, as well as a cell pair, was observed due to a significant increase in the substrate stiffness above a certain threshold as mentioned in [30, 42], which could very well shed light on fluid-solid transitioning observed in the constrained cell pack.

The living cells also use mechanical forces to communicate with neighboring cells leading to collective pack-like behavior [18]. The stresses exerted on the ECM are transmitted across the cells through cell-cell junctions [18]. The junctions between cells in a monolayer enable fast, long distant communication through intercellular stresses which balance the substrate tractions on the ECM-substrate interface [18]. Studying the mechanics of the collective behavior of cells is important to understand the functioning of various biological processes like morphogenesis, tissue repair, and cancer metastasis [22]. There are various factors that are known to contribute to this collective behavior. The movement of the cell (HUVEC) monolayer can be influenced by stiffness gradient (durotaxis), local maximum principal stress orientation (plithotaxis), or collective drive towards unfilled space (kenotaxis) [21, 40]. A series of cells in a locality could be driven by the movement of leader cells or cells closed to the leader cells [22].

The tractions on the substrate have been used as the measure of the cell’s contractile forces and captured using one of the most common techniques: Traction Force Microscopy (TFM) [22, 38].

The method computes the tractions based on the displacement field of fluorescent microbeads localized on the top surface of the substrate. In Monolayer Stress Microscopy (MSM) method, cell-cell intercellular stresses were recovered from TFM tractions by assuming a monolayer sheet of cells as elastic thin plates and imposing newton's force balance and strain compatibility equations [41].

As previously shown, changes in the ECM components including Col-I and FN can alter the ECM properties such as stiffness leading to various pathologies. The extent of interdependency among tractions, intercellular stresses of EC, and the ECM coated on the substrate remains unclear. More knowledge is required to understand the relationships between tractions, intercellular stresses, and ECM concentration on the substrate. To shed more light on the implications ECM can have on the cell mechanics, in this article, we measure the endothelial mechanics of HUVEC monolayers such as substrate tractions, strain energy, intercellular stresses, and morphological parameters including cell area, circularity, and orientation for five different volume ratios of Col-I and FN coated on the hydrogel substrate: i) 100% Col-I ii) 75% Col-I - 25% FN iii) 50% Col-I - 50% FN iv) 25% Col-I - 75% FN v) 100% FN. We also computed phi (Φ), the angle difference between the maximum principal stress orientation and the resultant displacement vector orientation of the cells to see how well plithotaxis was observed for the mentioned different coating ratios of Col-I and FN. Lower Φ values suggest that more cells are aligning towards the maximum principal stress orientations or plithotaxis [56].

Materials and Methods

Cell Culture

Human Umbilical Vein Endothelial Cells (HUVECs) used in the experiments were cultured in Medium 200 with 1% penicillin-streptomycin (Corning) and 2.153% Large Vessel Endothelial Supplement (LVES) solution. HUVECS, Medium 200, and LVES were purchased from ThermoFisher. HUVECs from passages 12-14 were cultured in 0.1% Gelatin (Sigma-Aldrich) coated flasks at 37^o C and 5% CO_2 prior to running all the experiments.

Polyacrylamide Gel Fabrication

The protocol for preparing Polyacrylamide (PA) gels can be found in [57]. Glass bottom petri dishes (35 mm, Cellvis) were treated with bind silane solution for 45 minutes after which the dishes were rinsed with DI water and air-dried. PA solution is made by mixing ultra-pure water, 40% acrylamide (Bio-Rad), 2% bis-acrylamide (Bio-Rad), and fluorescent beads (yellow or Texas red with ~0.5 µm diameter, Invitrogen). The stiffness of the PA gel can be fine-tuned by changing the ratio of Bis(acrylamide) and acrylamide solutions. The PA solution is kept in a vacuum chamber for 40 minutes. 10% ammonia persulfate and TEMED (N,N,N',N'- tetramethylethane-1,2-diamine) were added to the de-gassed PA solution which initiates polymerization reaction. After the addition of ammonia persulfate, TEMED the PA solution is mixed well and plated on the petri dish wells. Hydrophobic coverslips were then placed on top of the PA solution after which the dishes were inverted to allow more fluorescent beads to settle on the top layer of the polymerizing gel. The subsequent PA-gels with stiffness ~1.2 kPa (mimicking the stiffness of the healthy endothelium) and height ~100 µm were used for the experiments [58].

Cellular Micropattern Preparation

Polydimethylsiloxane (PDMS) was used to fabricate thin micropatterns as described previously in [57, 59]. A thin cross-section of PDMS (Dow Corning) was prepared by mixing silicone base with a curing agent (20:1) and the mixture was then poured into a 100 mm petri dish. The PDMS mixture in the petri dish with no air bubbles was then incubated at 70° C overnight. Thin, circular cross-sections of cured PDMS (16 mm) were fabricated using a hole puncher. Small holes (5-6 micropatterns) were made on the circular PDMS section using a biopsy punch (world precision instruments) with a diameter of ~2 mm each. The fabricated micropatterns were gently stamped on the top layer of the PA-gels.

SANPAH Burning & Col I-FN Treatment

The petri dish samples with PDMS micropatterns stamped on PA gels were then subject to treatment with sulfosuccinimidyl-6-(4-azido-2-nitrophenylamino) hexanoate (Sulfo-SANPAH; Proteochem) dissolved in 0.1 M HEPES buffer solution (Fisher Scientific) and kept under a UV lamp for 8 mins. After SANPAH and UV treatments, the samples were treated with each of the following ratios of Collage I (Col-I) & Fibronectin (FN): 1) 100% Col-I (0.1 mg/ml) 2) 75% Col-I and 25% FN (0.075 mg/ml & 0.025 mg/ml) 3) 50% Col-I and 50% (0.05 mg/ml & 0.05 mg/ml) FN 4) 25% Col-I and 75% FN (0.025 mg/ml & 0.075 mg/ml) 5)100% FN (0.1 mg/ml).

After the treatment of Col-I (Advanced Biomatrix) or FN (ThermoFisher Scientific) or ratio of Col-I and FN overnight at 4° C, the excess protein solution was carefully removed and HUVECs were seeded at a density of ~50 × 10^4 cells/mL. After 60-75 mins, micropatterns were cautiously removed using a tweezer. The HUVEC's monolayer samples were incubated at 37° C and 5% CO_2

for at least 24 hours to allow enough time for the formation of cell-cell junctions prior to experimentation.

Time Lapse Microscopy

A Zeiss inverted microscope equipped with 5x objective & Hamamatsu camera was used to acquire phase contrast and fluorescent images for every 5 min. HUVEC monolayer samples for each Col-I -FN concentration ratio were imaged for 3 h after which the cells were subject to the treatment of 10x trypsin for 10 min. The PA-gels in the samples after trypsinization were imaged to obtain the stress-free reference configuration of the fluorescent beads on the top layer of the gel from which the displacement field of the beads and traction map on the substrate were calculated.

Substrate Displacement Computation

The 2-D displacement of fluorescent beads on the top surface of the gel was computed using a window-based PIV routine. The entire image was divided into a set number of overlapping windows depending on the crop size of the image used for the PIV analysis. Cross-correlation between each window in the reference image was computed against a window occupying the same coordinates in the fluorescent image (with cells attached) sequentially, across all the window blocks. The displacements were calculated in the x and y coordinate system in pixels using an iterative cross-correlation function. The displacement calculated from the peak cross-correlation function between each reference-fluorescence window pair was assigned to the center coordinates of those windows [36].

Traction Force Microscopy (TFM) and Monolayer Stress Microscopy (MSM)

Traction force Microscopy and monolayer stress microscopy as previously described in [22, 38, 56, 57] was used to calculate the traction maps on the PA gel substrate and intercellular stresses respectively. Briefly, the deformations on the top surface of the gel were calculated by running a window-based particle image velocimetry (PIV) routine that computes the pixel shift in fluorescent images of the gel (cells attached) with respect to the stress-free reference image (fluorescent image taken after trypsinization). Intercellular stresses were calculated as previously described in [56, 57]. The intercellular stresses were recovered from traction force maps on the substrate by using straightforward force balance equations imposed through Newton's law. The computed local two-dimensional stress tensor within the monolayer was converted into maximum principal stress (σ_{max}) and minimum principal stress (σ_{min}) along the principal plane by rotating the local coordinate system along with the principal orientation. The average normal stress $(\sigma_{max} + \sigma_{min})/2$ and maximum shear stress $(\sigma_{max} - \sigma_{min})/2$ were calculated at each point in the elements within the monolayer as discretized by the FEM code.

Measurement of Cell Velocity

The velocity of HUVECs in the monolayer was computed using a similar but modified version of the PIV routine as mentioned above in MATLAB 2019 (see supplementary figure). Cell displacements were calculated from pixel shifts between phase images at two consecutive time points. The velocity map of the cells in the monolayer was calculated by averaging the change in displacements over the time interval. Cell velocity was calculated at every 5 min interval for the entire sequences of images acquired over 3 hours.

HUVEC Area, Orientation, and Circularity Measurements

Cell features like area, circularity, and orientation were measured using a function written in MATLAB 2019a utilizing an image processing toolbox. Individual HUVEC area, orientation, and circularity were calculated from five cropped regions of 651 µm × 651 µm cross-section for each condition (5 different coating concentrations of Col-I and FN).

Image Segmentation

Phase-contrast images were converted into binary images and the individual cells were identified and isolated by utilizing the region properties and image segmentation functions in MATLAB 2019a Image Processing Toolbox. Briefly, the phase-contrast images were converted to binary images using the ‘imbinarize’ command by selecting a threshold sensitivity of 0.7-0.75. The background noise in the binary images was removed using the ‘bwareaopen’ command followed by other basic segmenting commands to enhance cell blobs and fill voids. The image was then processed using the ‘watershed’ command to separate cell boundaries.

Feature Extraction

The features of the segmented binary image, including cell area, orientation, and circularity were then extracted using the ‘regionprops’ command in MATLAB. The extracted cell features were grouped into a different number of bins with bin width and the number of bins automatically chosen by the command ‘histcounts’. Color maps were assigned to the different bins such that all cells within a bin having the same color. The different morphological features were visualized by using ‘figure’ and ‘image’ commands for MATLAB color plots. The cell features extracted from the five phase-contrast images including area, orientation, and circularity for each Col-I and FN coating concentration ratio were grouped together. The different ratio groups were tested for statistical significance with respect to the col-I 100% condition.

Unit Conversions

The cell area was calculated as the number of pixels contained in a region (sq. pixels) and converted to μm^2 based on the pixel to the micron conversion factor. The circularity was calculated using the 'regionprops' command which uses the formula: circularity = $(4\times\pi\times area)/(perimeter^2)$. The circularity (dimensionless) has values ranging from 0 to 1 with values close to 1 for perfect circles and reduces as the circularity decreases. To calculate cell orientation, the 'regionprops' command fits an ellipse onto the cells and the orientation angle was calculated based on the angle the major axis of the ellipse approximation of the cell makes with respect to the global X-axis ranging from $+90^o$ (1st quadrant) to -90^o (4th quadrant) in the clockwise direction. The rose plots with 10 bins represent the cell orientations from$+90^o$ (1st quadrant) to -90^o (4th quadrant) in clockwise direction (see supplementary figure). The radius of the rose plots represents the number of cells (count) in each of the 10 bins (bin width = 18 degrees). To calculate the average cell orientation, the angles in the 4th quadrant (negative angles from 0^o to -90^o) were converted to the 2nd quadrant (90^o to 180^o) by adding 180^o.

Statistical Analysis

The number of cells analyzed was 1057 to 1460 cells for each coating concentration ratio. Each Col-I and FN coating ratio (75% Col-I - 25%FN, 50% Col-I - 50% FN, 25% Col-I - 75% FN, 100% FN) was tested for statistical significance with respect to the 100% Col-I condition using ANOVA: Single Factor hypothesis test for cell area, cell orientation, and circularity respectively. The p-values for significance were calculated with an alpha level of 0.05 (Null hypothesis rejected for $p < 0.05$).

Computation of Phi (Φ)

Phi (Φ) is the angle difference between the maximum principal stress vector orientation and the resultant cell displacement vector orientation with respect to the global X-axis. (angles measured in quadrants I and II from 0^o to 180^o counterclockwise). The resultant displacement vectors of the cells were obtained from the PIV routine mentioned in the measurement of cell velocity section. The angle the resultant displacement vector makes with respect to the X-axis (from 0^o (1st quadrant) to 180^o (2^{nd} quadrant) in the counterclockwise direction) is calculated by taking the arctangent of the ratio Y-Displacement/X-Displacement. Also, maximum principal stress orientations with respect to the X-axis were calculated from the local normal and shear intercellular stresses recovered from MSM. We then computed phi (Φ), orientation within 651 µm × 651 cropped monolayer section for different coating ratios of Col-I and FN (refer to the supplementary section for the figures).

Results

Cell mechanics of HUVEC monolayers including average normal & maximum shear intercellular stresses and RMS traction maps on the substrate were calculated for different concentration/volume ratios of Collagen and Fibronectin (Col-I and FN) ECM solution used to coat the PA Gel surface on which the cells were seeded. The HUVEC monolayer data comprising results from a 3-hour experiment for 20 samples (5 per each condition) within a cropped section of 651 µm × 651 µm were used for the analysis. The cropped section was selected inside the circular HUVEC monolayer (seeded within the 2mm micropattern) to negate any boundary effects from the free edges. The average monolayer intercellular stresses and RMS traction exerted on the substrate were calculated based on averages in the cropped window from 5 islands (each island is a circular monolayer with free edges) for each selected Col-I and FN volume ratio. The average HUVEC monolayer velocity and cell features like cell spread area, cell orientation and circularity were also computed from 5 islands for 5 different Col-I and FN concentration ratio (Figure 6) 1) 100% Col-I (0.1 mg/ml) 2) 75% Col-I and 25% FN (0.075 mg/ml & 0.025 mg/ml) 3) 50% Col-I and 50% (0.05 mg/ml & 0.05 mg/ml) FN 4) 25% Col-I and 75% FN (0.025 mg/ml & 0.075 mg/ml) 5)100% FN (0.1 mg/ml).

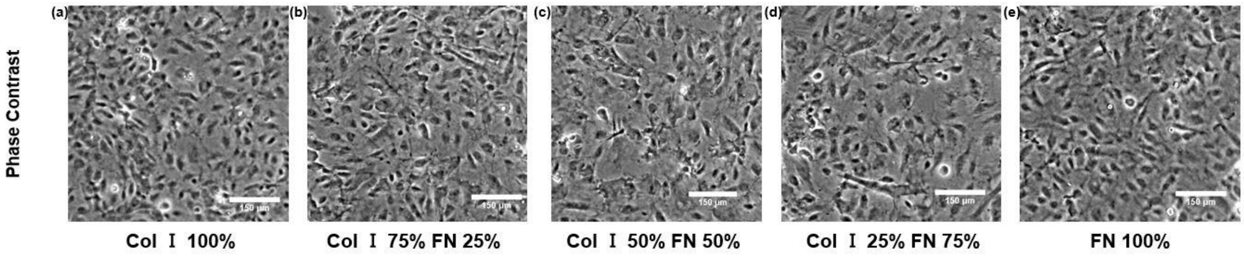

Col I 100% **Col I 75% FN 25%** **Col I 50% FN 50%** **Col I 25% FN 75%** **FN 100%**

Figure 6: Cropped HUVEC monolayer phase contrast images (within 651 × 651 µm^2) for different Col-I and FN coating concentration ratios: Col-I 100% (a), Col-I 75% FN 25% (b), Col-I 50% FN 50% (c), Col-I 25% FN 75% (d), FN 100% (e). Scale bar length = 150 µm

Col-FN Influence on RMS Traction, Strain Energy, and HUVEC Velocity

(See Figure 7 a-f) The average RMS traction was also the highest for 50% Col-I & 50% FN with 78.7±0.8 Pa. Unlike intercellular stresses, average RMS traction was the least for 100% Col-I ECM with 32.6±0.05 Pa slightly below 100% FN (35±0.06 Pa). The RMS traction was second highest for 75% Col-I & 25% FN (65.8±0.12 Pa) above 25% Col-I & 75% FN (49.3±0.2 Pa). The computed average strain energies followed the same trend as RMS tractions. 50% Col-I & 50% FN had the highest strain energy (63±1 pJ) followed by 75% Col-I & 25% FN (45.4±0.3 pJ) and 25% Col-I & 75% FN (22.58±1.6 pJ). 100% FN had the least average strain energy (9.73±0.075 pJ) followed closely by 100% Col-I with 10.25±0.083 pJ (See figure 8).

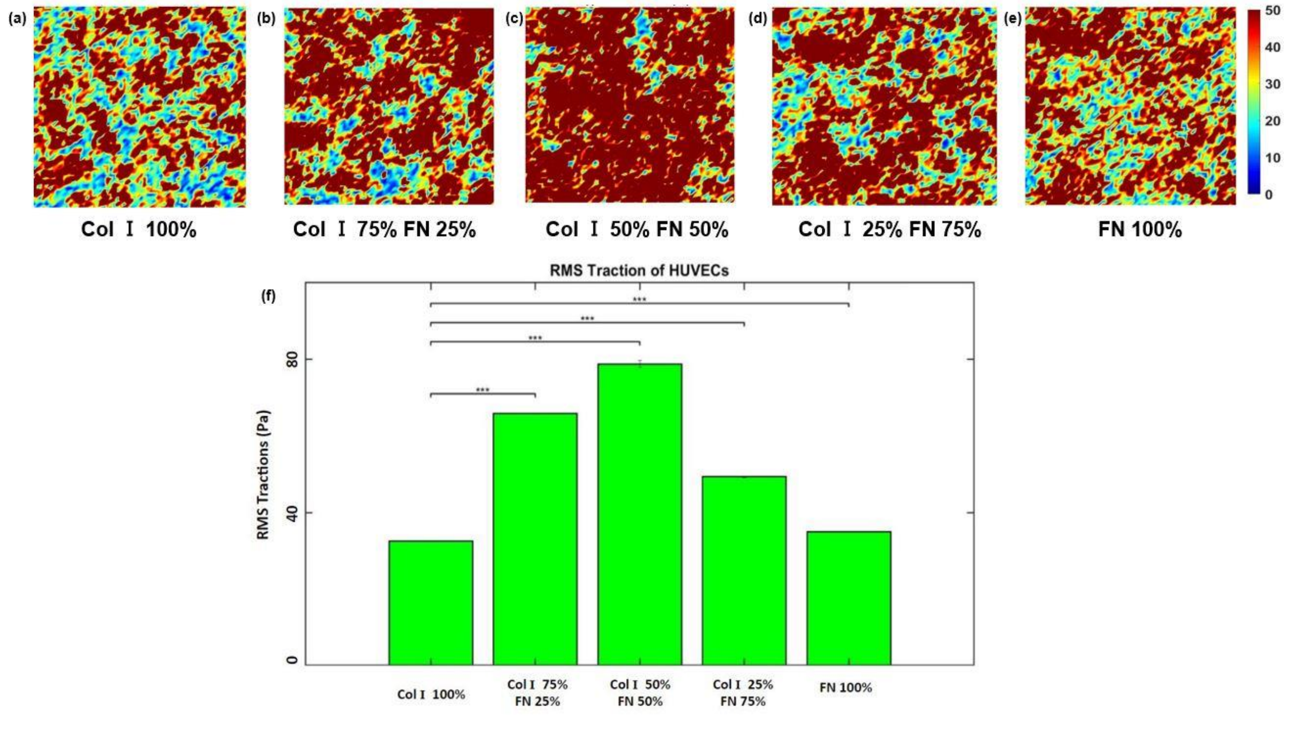

*Figure 7: RMS traction (within 651 × 651 μm^2 cropped section) distributions (Pa) for different Col-I and FN coating concentration ratios: Col-I 100% (a), Col-I 75% FN 25% (b), Col-I 50% FN 50% (c), Col-I 25% FN 75% (d), FN 100% (e) and average RMS tractions (Pa) for different Col-I and FN coating concentrations based on averages from five samples for each ratio (f). * represents statistical significance (* p <= 0.05; ** p <= 1E-2; *** p<= 1E-3, no star p > 0.05)*

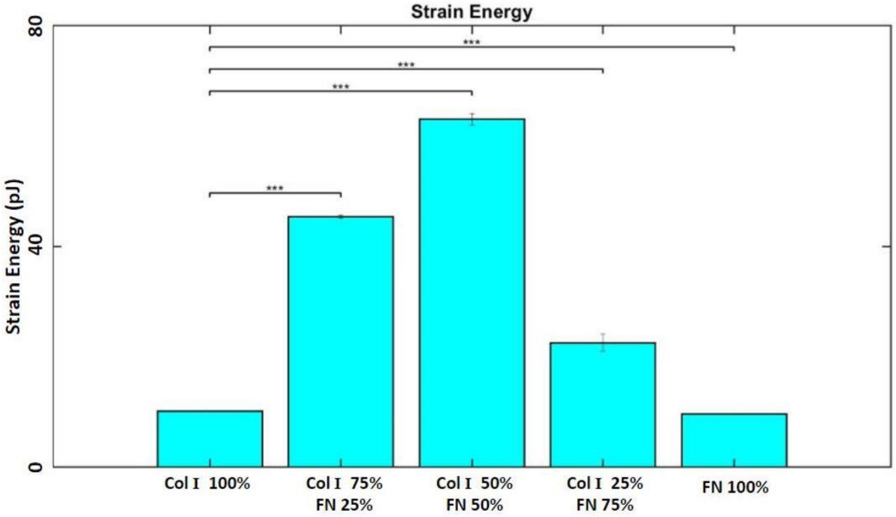

*Figure 8: Average strain energies (pJ) for different Col-I and FN coating concentrations based on averages from five samples for each ratio. * represents statistical significance (* p <= 0.05; ** p <= 1E-2; *** p<= 1E-3, no star p > 0.05)*

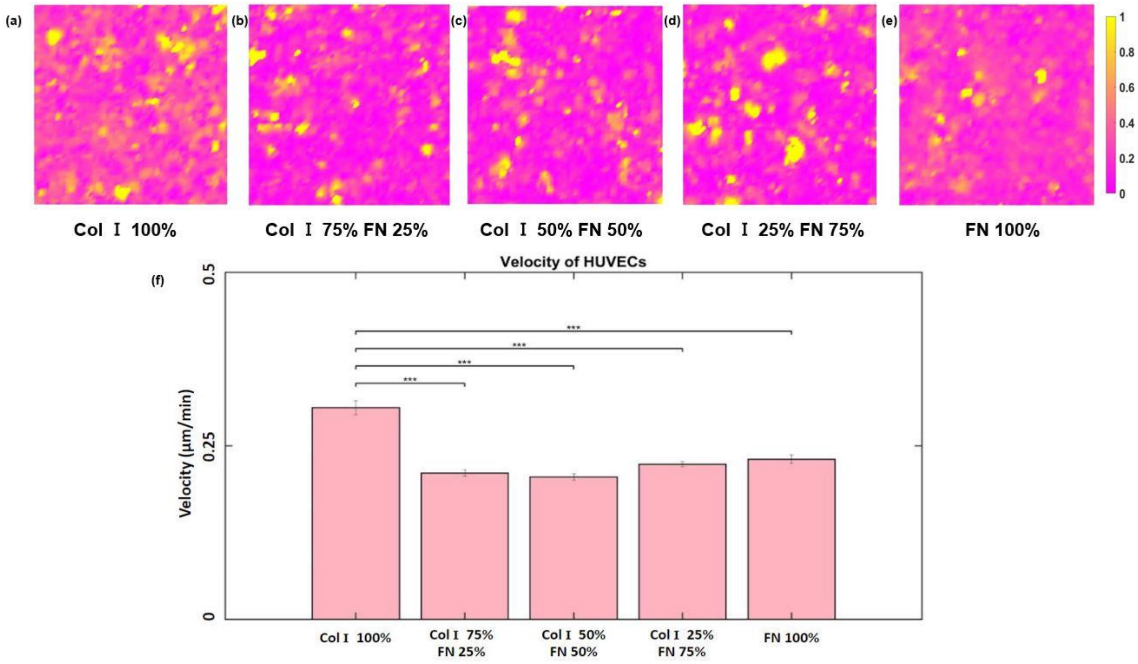

*Figure 9: RMS velocity (within $651 \times 651\ \mu m^2$ cropped section) distributions (µm/min) for different Col-I and FN coating concentration ratios: Col-I 100% (a), Col-I 75% FN 25% (b), Col-I 50% FN 50% (c), Col-I 25% FN 75% (d), FN 100% (e) and average RMS (Pa) for different Col-I and FN coating concentrations based on averages from five samples for each ratio (f). * represents statistical significance (* p <= 0.05; ** p <= 1E-2; *** p<= 1E-3, no star p > 0.05)*

The velocity was lowest for 50% Col-I & 50% FN with 0.205±0.004 µm/min and highest for 100% Col-I with 0.305±0.01 µm/min. The velocity for other ECM ratios was only slightly higher compared to 50% Col-I & 50% FN (from figure 9 a-f).

Col-FN Influence on Intercellular Stresses

From figure 10 a-f, the average normal and maximum shear intercellular stresses were highest for 50% Col-I & 50% FN (0.05 mg/ml Col & 0.05 mg/ml FN) with 596±1.6 Pa and 304.5±1.4 Pa respectively. Similarly, average normal and maximum shear intercellular stresses were lowest for 25% Col-I and 75% FN ECM ratio with 281.5±2.2 Pa and 159.7±0.7 Pa respectively. There was no statistically significant difference between 100% Col I & 75% Col-I and 25% FN with respect to average normal stress. The average normal stress was slightly lower for 100 % FN compared to 100% Col-I. The maximum shear stress was slightly higher for 100% Col-I compared to 25% Col-I & 75% FN. The maximum shear stress was the second-highest for 75% Col-I & 25% FN slightly higher than 100% FN (see figure 11 a-f).

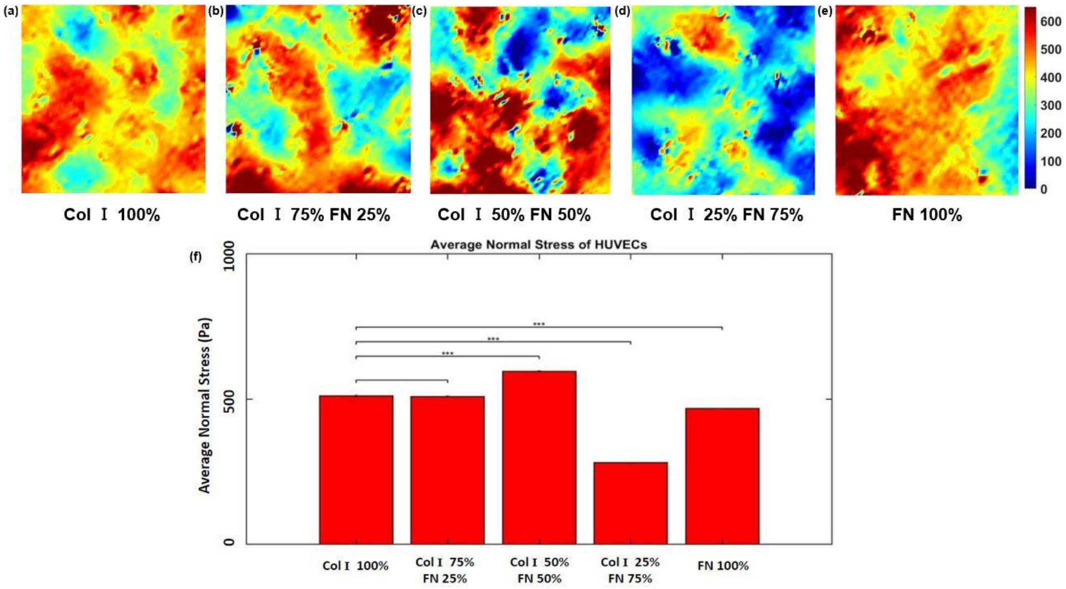

*Figure 10: Average normal stress (within 651 × 651 μm^2 cropped section) distributions (Pa) for different Col-I and FN coating concentration ratios: Col-I 100% (a), Col-I 75% FN 25% (b), Col-I 50% FN 50% (c), Col-I 25% FN 75% (d), FN 100% (e) and average normal stress (Pa) for different Col-I and FN coating concentrations based on averages from five samples for each ratio (f). * represents statistical significance (* p <= 0.05; ** p <= 1E-2; *** p<= 1E-3, no star p > 0.05)*

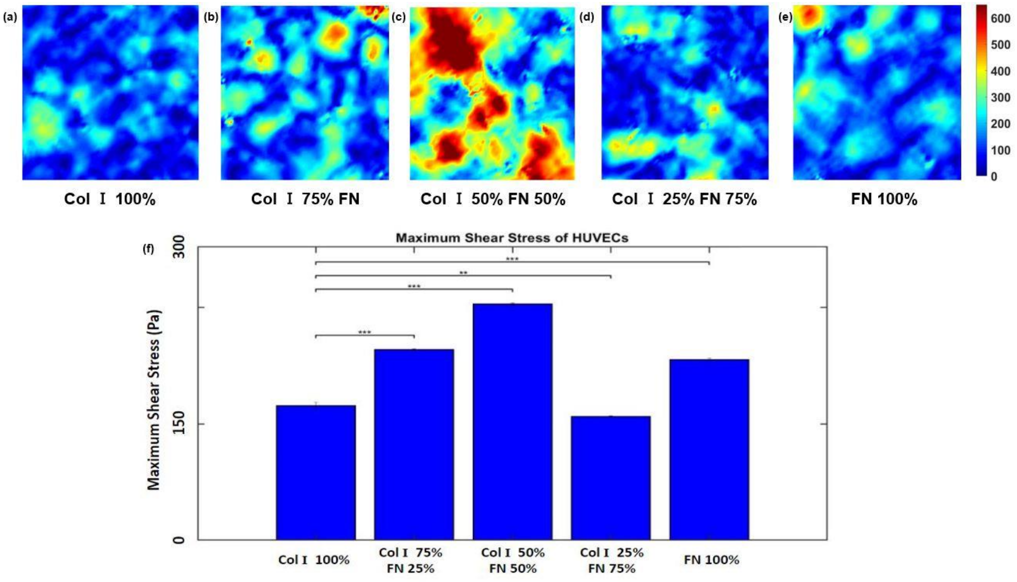

*Figure 11: Maximum shear stress (within 651 × 651 μm^2 cropped section) distributions (Pa) for different Col-I and FN coating concentration ratios: Col-I 100% (a), Col-I 75% FN 25% (b), Col-I 50% FN 50% (c), Col-I 25% FN 75% (d), FN 100% (e) and average maximum shear stress (Pa) for different Col-I and FN coating concentrations based on averages from five samples for each ratio (f). * represents statistical significance (* p <= 0.05; ** p <= 1E-2; *** p<= 1E-3, no star p > 0.05)*

Col-FN Influence on HUVEC Cell Features

Cell features like cell spread area, cell orientation, and cell circularity were computed for the five different ECM ratios under study (see figure 12-14). Cell spread area and cell circularity were statistically significant when each ECM ratio group was compared with 100% Col-I case. The average cell spread area was the highest for 50% Col-I & 50% (521±8.3 μm^2) and the lowest for Col-I 100% (425.515±4.3 μm^2) compared to other groups (see figure 12). The average cell circularity was almost an inverse behavior relative to the cell spread area. Circularity is a dimensionless number that ranges from 0 to 1 with 1 being perfect circles. The average cell circularity was the highest for 100% Col-I (0.68±0.005) contrast to what we saw in the cell spread area. Also, average cell circularity was the lowest for 50% Col-I & 50% FN (0.6±0.006) explaining the high cell spread area discussed earlier (Figure 14). No statistical significance was observed with respect to cell orientation among different groups (Figure 13). The rose plots (radius = number of cells; bin-width = 18^o) showing the orientation of HUVECs with respect to the X-axis, in +90^o (1st quadrant) to -90^o (4th quadrant) in the clockwise direction, for different ECM coating concentrations, can be seen from figure 13. No clear polarization with respect to a coating ratio was observed from the rose plots and average orientation. Also, no statistically significant difference among the groups was observed for average orientation data (shown in supplementary) because the experimental conditions were static in a constrained geometry setup, and the cells were not significantly influenced by any external or internal stresses to contribute to a preferential orientation.

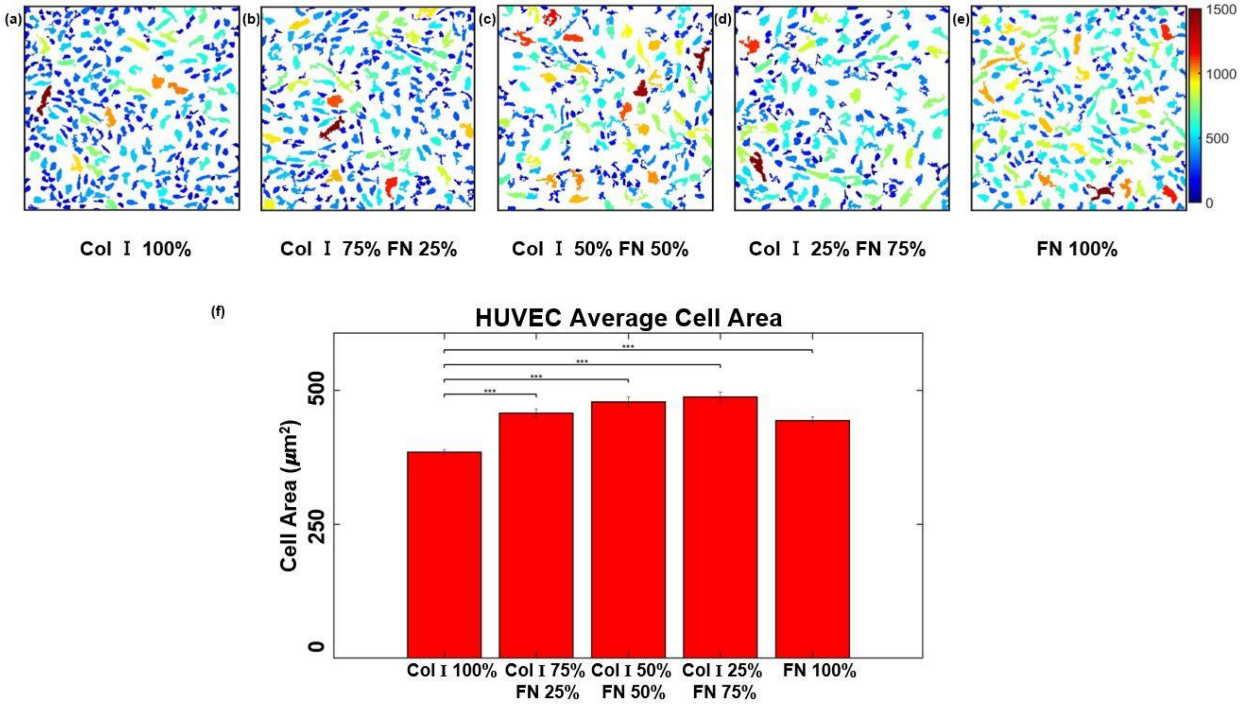

*Figure 12: HUVEC area in μm^2 (within 651 × 651 μm^2 cropped section) for different Col-I and FN coating concentration ratios: Col-I 100% (a), Col-I 75% FN 25% (b), Col-I 50% FN 50% (c), Col-I 25% FN 75% (d), FN 100% (e) and average cell area (μm^2) for different Col-I and FN coating concentrations based on averages of 1057 to 1460 cells from five samples for each concentration ratio (f). * represents statistical significance (* $p <= 0.05$; ** $p <= 1E-2$; *** $p<= 1E-3$, no star $p > 0.05$)*

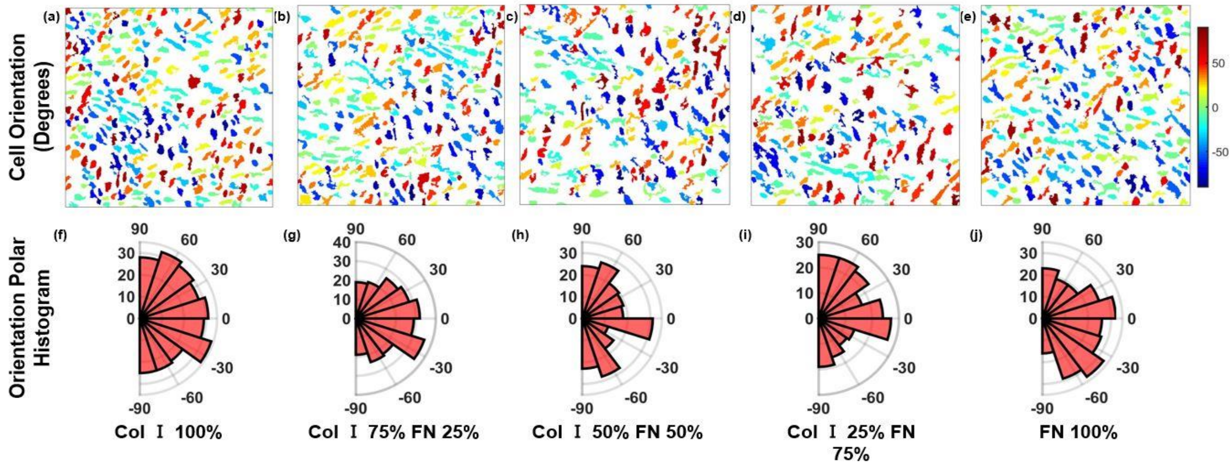

Figure 13: HUVEC orientation with respect to the X-axis, in +90^o (1st quadrant) to -90^o (4th quadrant) in clockwise direction in degrees (within 651 × 651 μm^2 cropped section) for different Col-I and FN coating concentration ratios: Col-I 100% (a), Col-I 75% FN 25% (b), Col-I 50% FN 50% (c), Col-I 25% FN 75% (d), FN 100% (e) and corresponding rose plot histograms (degrees) for different Col-I and FN coating concentrations (f-j). Radius = cell count per bin, Total number of bins per cropped section =10; bin-width = 18^o)

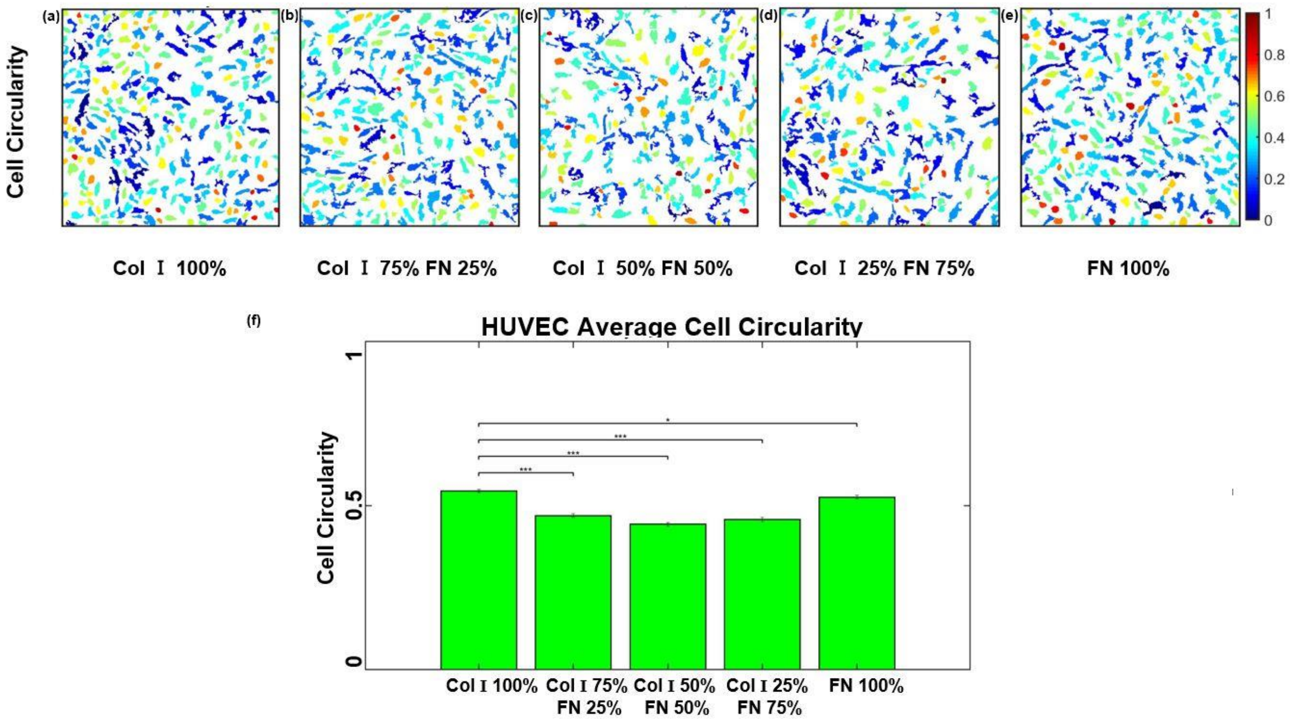

*Figure 14: HUVEC circularity (within 651 × 651 μm^2 cropped section) for different Col-I and FN coating concentration ratios: Col-I 100% (a), Col-I 75% FN 25% (b), Col-I 50% FN 50% (c), Col-I 25% FN 75% (d), FN 100% (e) and average cell circularity (dimensionless) for different Col-I and FN coating concentrations based on averages of 1057 to 1460 cells from five samples for each ratio (f). * represents statistical significance (* p <= 0.05; ** p <= 1E-2; *** p<= 1E-3, no star p > 0.05)*

Discussion

The influence of five different Col-I and FN ECM concentrations on HUVEC biomechanics and physical features were studied. Surprisingly, 50% Col-I & 50% FN consistently recorded the highest intercellular stresses (average normal & maximum shear stresses) and root mean squared tractions based on averages from five cropped cross-sections for each Col-I and FN ratio averaged over a period of 180 minutes (see figures 7, 10 and 11). The former ratio also had the highest average cell area and the least average root means square velocity and circularity. Similarly, 75% Col-I & 25% FN had the second-highest average intercellular stresses and root mean square tractions and the second least average root mean square velocity. However, the same expected trend was not observed with respect to average cell area and circularity for 75% Col-I & 25% FN. Also, no other consistent trends were observed for other Col-I and FN ratios.

The inverse correlations of intercellular stresses and tractions with respect to average RMS cell velocity and circularity observed in 50% Col-I & 50% FN could be attributed to an increase in average cell spread area which reduces the circularity of the cell as its morphology becomes more elliptical increasing the number of anchor sites. [44] showed a positive correlation between traction forces and cell spread area which was observed for 50% Col-I & 50% FN ratio and Col-I 100%. However, the same trend could not be seen with respect to the other ratios.

Kaustabh et al. [43] showed that tractions were directly proportional to the substrate stiffness, but the average cell speed was inversely proportional to the substrate stiffness. Supporting this an inverse relationship between average cell speed and tractions was observed in all the five different Col-I and FN ECM ratios. However, there was no clear evidence if tractions regulate cell speed as cell migration speed is independent of Myosin II while tractions depend on it [60]. It has been shown that average cell speed increases linearly for lower FN concentrations ($<10\ \mu g/cm^2$) which was noticeable for increasing FN concentration in the ECM ratio [61].

High tractions and intercellular stresses observed in 50% Col-I & 50% FN and 75% Col-I & 25% ECM ratios could be explained through Col-I and FN interactions. [62] show that collagen fibers co-localize favorably with FN fibrils that are stretched. As Col-I and FN fibers stabilize, mature collagen fibers act as a protective stress shield for FN fibrils [62]. This one-to-one ratio of Col-I and FN might have stabilized the ECM-substrate interface leading to high tractions and intercellular stresses within EC monolayer based on mechano-regulation of ECM proteins [62].

[63] showed that the cell traction forces on the substrate are proportional to the adsorption force of the FN. FN with a low adsorption force at the substrate interface might be desorbed during traction force transmission failing to transmit the mechanical stresses to the substrate [63]. The FN fibrils stabilized by collagen might have decreased the FN desorption in the case of 50% Col-I & 50% FN and 75% Col-I & 25% FN ECM ratios resulting in higher tractions and intercellular stresses relative to other ratios [63]. More studies investigating the dynamics between different ratios of FN-Col-I are necessary to really understand the cell-ECM mechanics.

A statistically significant difference was observed among different Col-I and FN ratio groups with respect to Col-I 100% for phi (Φ), the angle difference between cell resultant displacement orientation, and maximum principal stress orientation. The average value of Φ was much higher for all the different ECM coating ratios compared to results from Tambe et al. even for the Φ computed for top 20 percentile principal stress locations. However, data analyzed were from an unconstrained monolayer which could be the reason for a relatively lower signal. We observed that Φ was lowest for the 100% Col-I and increased as the coating concentration of Col-I decreased. The highest Φ was observed in 100% FN case followed by 50% Col-I and 50% FN coating concentration ratio (see supplementary figure 4).

Conclusion

ECM plays an important role in maintaining cell physiology and abnormality in ECM deposition or composition might lead to a host of neurological, cardiovascular pathologies, and even cancer metastasis. The link between different ECM proteins and cell mechanics is currently unknown and our knowledge of endothelial mechanics with respect to different ECM proteins is very limited. We believe, our study, can shed more light on the impact of two major ECM proteins (Col-I & FN) on endothelial mechanics which are mainly linked to coronary artery diseases. Our results clearly show that different concentration ratios of Col-I & FN coated on the cell-substrate have a differential response to endothelial cell mechanics such as tractions, strain energies, intercellular stresses, velocities, and morphological parameters such as cell area and circularity, under static conditions. However, we couldn’t clearly explain why cell mechanics was significantly higher for only a 50% coating concentration ratio of Col-I and FN. Also, more studies are required to establish the relationship between endothelial mechanics and different ECM proteins and to expand our knowledge on the role that a specific or a combination of ECM proteins play in a cell’s physiology. Such studies can be helpful in designing drugs that can alter ECM composition in a specific manner to achieve the desired biomechanical response and possibly preventing disease or decelerating disease progression by understanding the mechanism of vascular-related pathologies.

Supplementary

Overall computational methodology of tractions and intercellular stresses is shown in figure 15 below. The theory and mathematical details of the TFM and MSM were described previously in the Research Methodology section of the dissertation. Figure 15 (a-c) represents the displacement field (in pixels) computed from the reference and time-lapse fluorescence images. Figure 15 (d) represents the RMS tractions calculated using TFM.

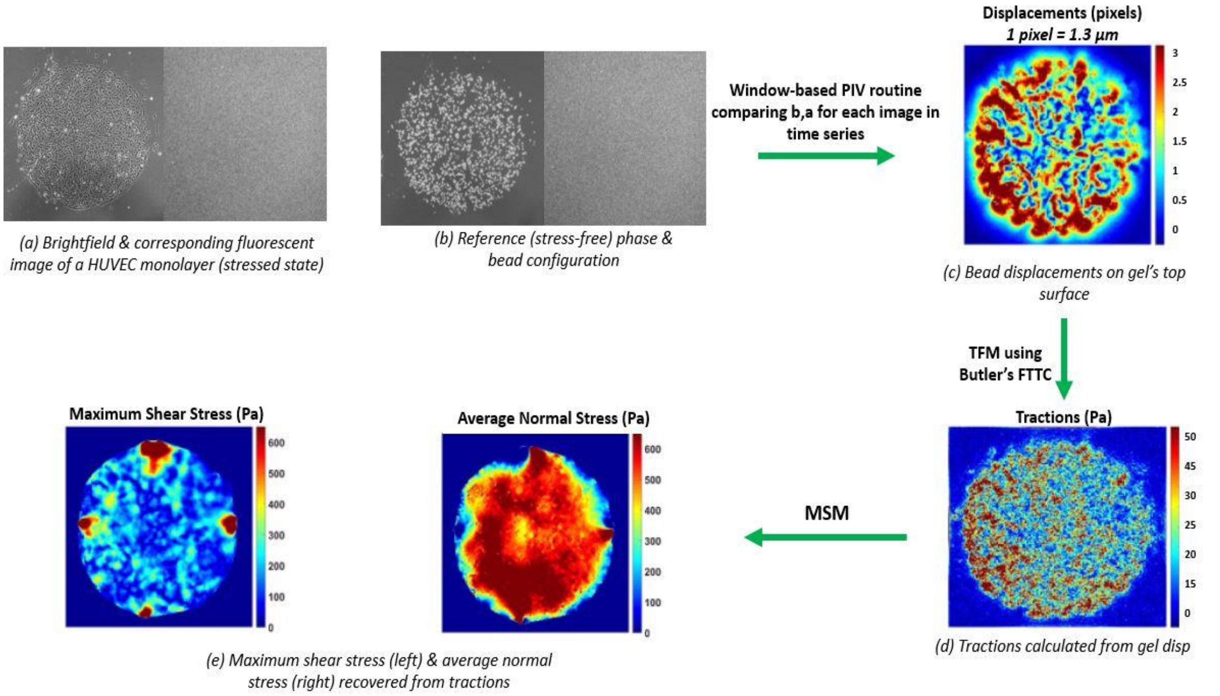

(a) Brightfield & corresponding fluorescent image of a HUVEC monolayer (stressed state)

(b) Reference (stress-free) phase & bead configuration

(c) Bead displacements on gel's top surface

(d) Tractions calculated from gel disp

(e) Maximum shear stress (left) & average normal stress (right) recovered from tractions

Figure 15: Overall computational methodology of tractions and intercellular stresses

Figure 15 (e) represents the average normal stress and the maximum shear stress recovered using MSM.

The pictorial depiction of the RMS velocity described in the materials and methods section of this chapter is shown in figure 16 below.

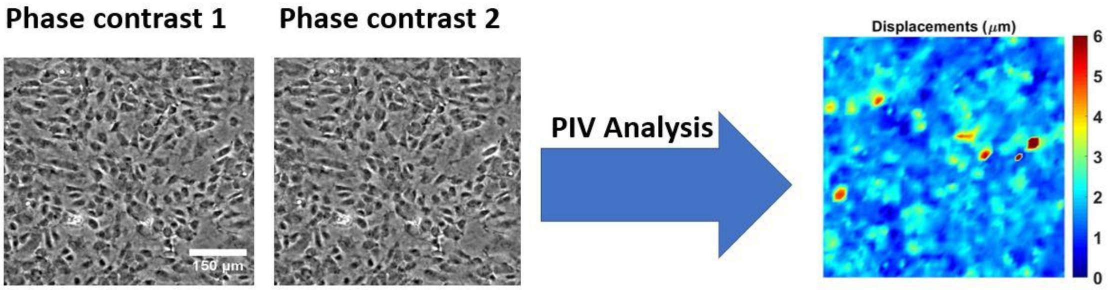

$$\boldsymbol{Displacement_{RMS} = sqrt((XDisp)^2 + (YDisp)^2)}$$

$$\boldsymbol{Velocity_{RMS}} = \frac{\boldsymbol{Displacement_{RMS}}}{\boldsymbol{Time\ interval\ between\ consecutive\ images}}$$

Figure 16: RMS velocity calculation from two phase contrast images in the time lapse

For the morphology analysis, the images were enhanced to identify the individual binarized cells in the field of view. The cell features such as cell area and cell circularity can then be calculated using the 'regionprops' command as shown in the figure.

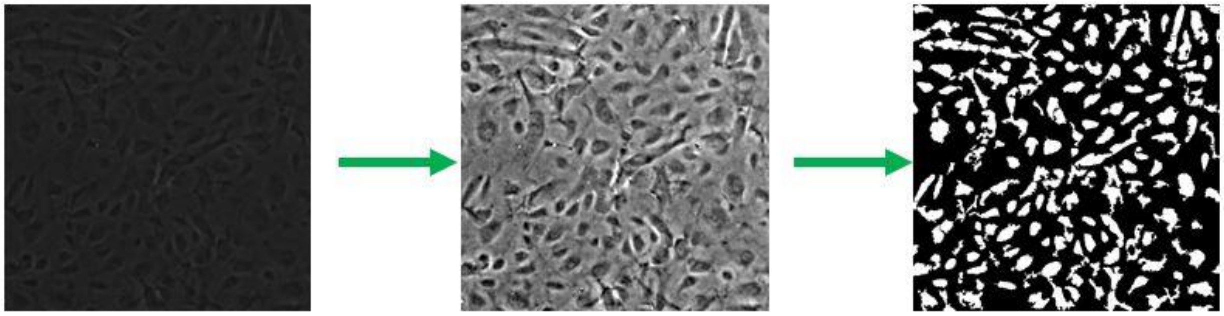

Figure 17: Phase image enhanced and binarized using image processing tools in MATLAB

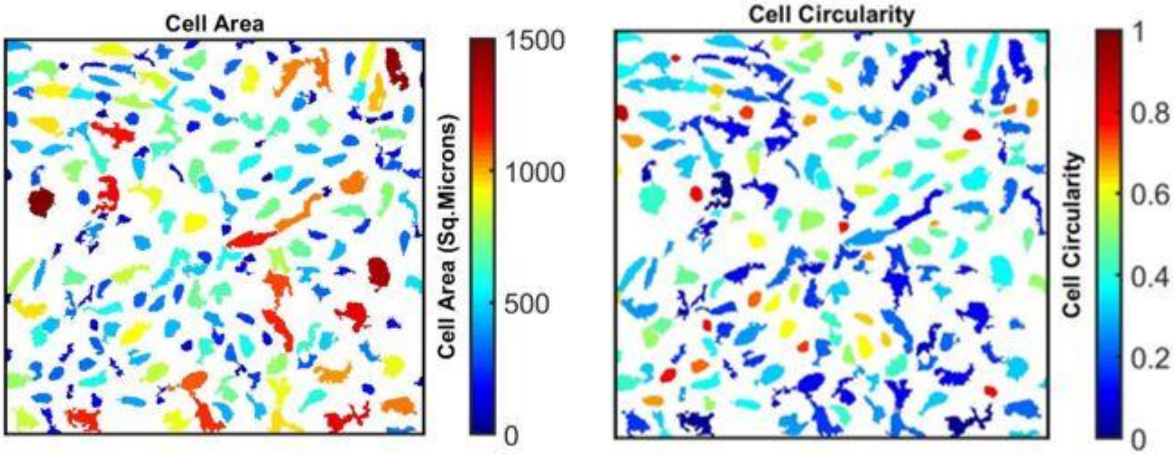

Figure 18: Corresponding cell area and cell circularity extracted for the binarized image in figure 17

From the maximum and minimum principal stresses calculated from MSM, stress ellipses can be constructed using the angle maximum principal stresses make with the X-axis (principal orientations). The magnitudes of the maximum and minimum principal stresses form the major and minor axes of the ellipse. The number of stress vectors and the corresponding angles were scaled down using bicubic interpolation in MATLAB.

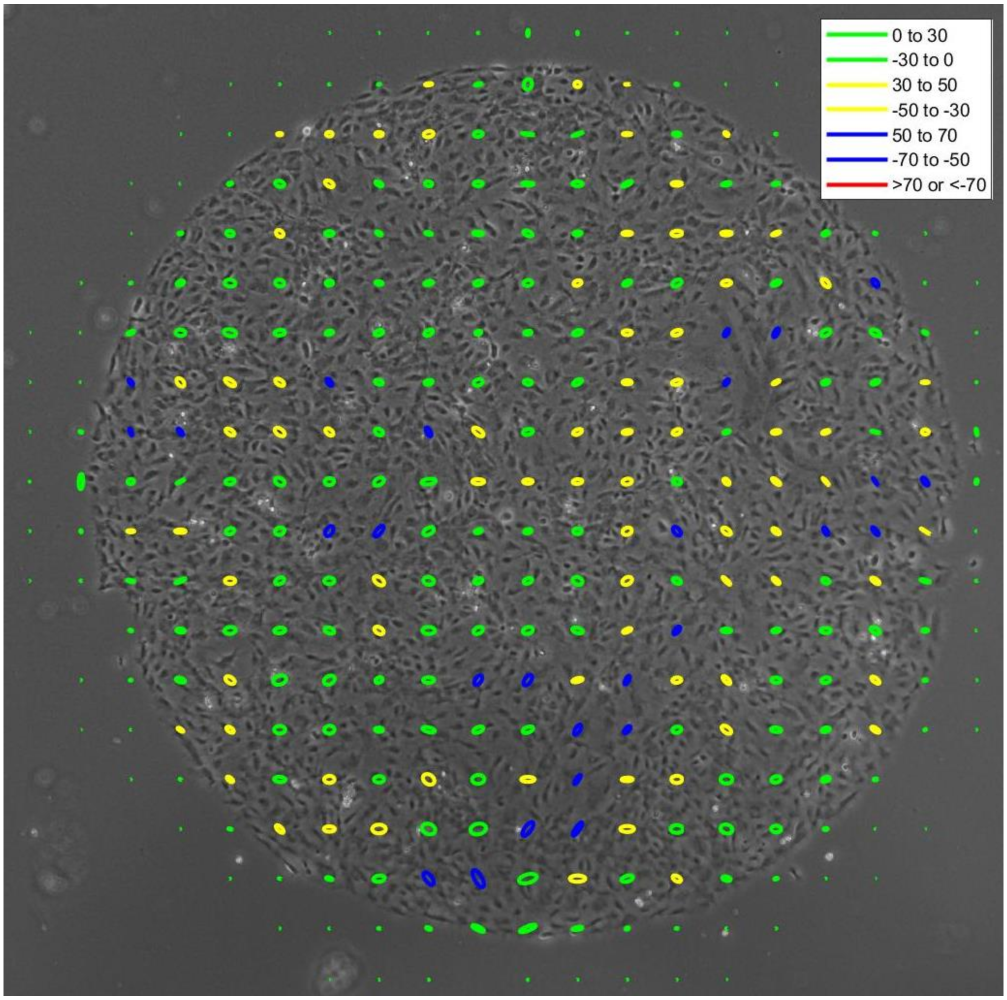

Figure 19: Stress ellipses matched to the phase contrast image with principal orientations (degrees) sorted into 7 bins from +90 to -90 (1st and 4th quadrants)

RMS traction vectors and maximum principal stress vectors can be matched to resultant displacement vectors of the cells. As mentioned in the materials and methods section in this chapter, it can be shown that 90th percentile local maximum stresses can drive the cell displacements which was termed as plithotaxis [56]. Plithotaxis signal can be quantified by calculating angle phi (Φ = difference between maximum principal stress and cell displacement vectors). Φ ranged between 0-30 degrees for top percentile stresses for expanding monolayer as shown in [56]. We observed a similar signal where Φ was mostly between 0-60. However, the signal was not as strong because the monolayer was constrained.

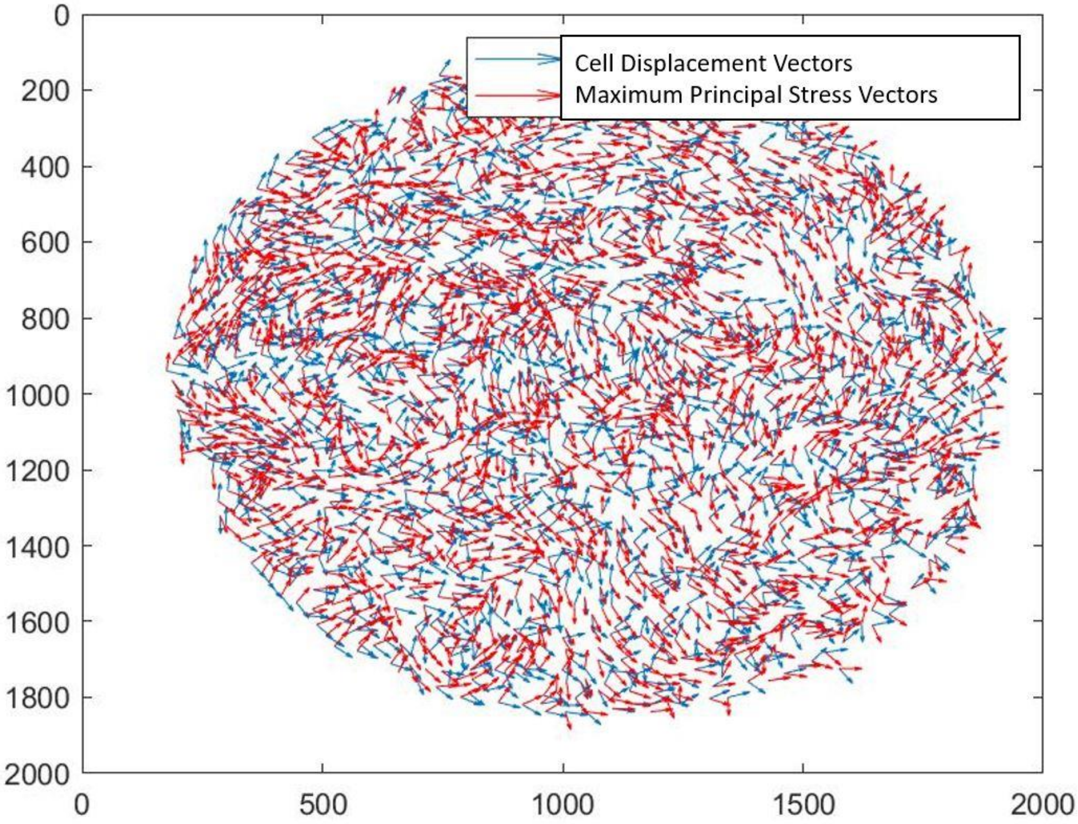

Figure 20: Visualizing the cell displacement and maximum principal stress vectors in the entire field of view

Similar to figure 20, both traction vectors and cell displacement vectors can also be matched, and their angle difference can be calculated.

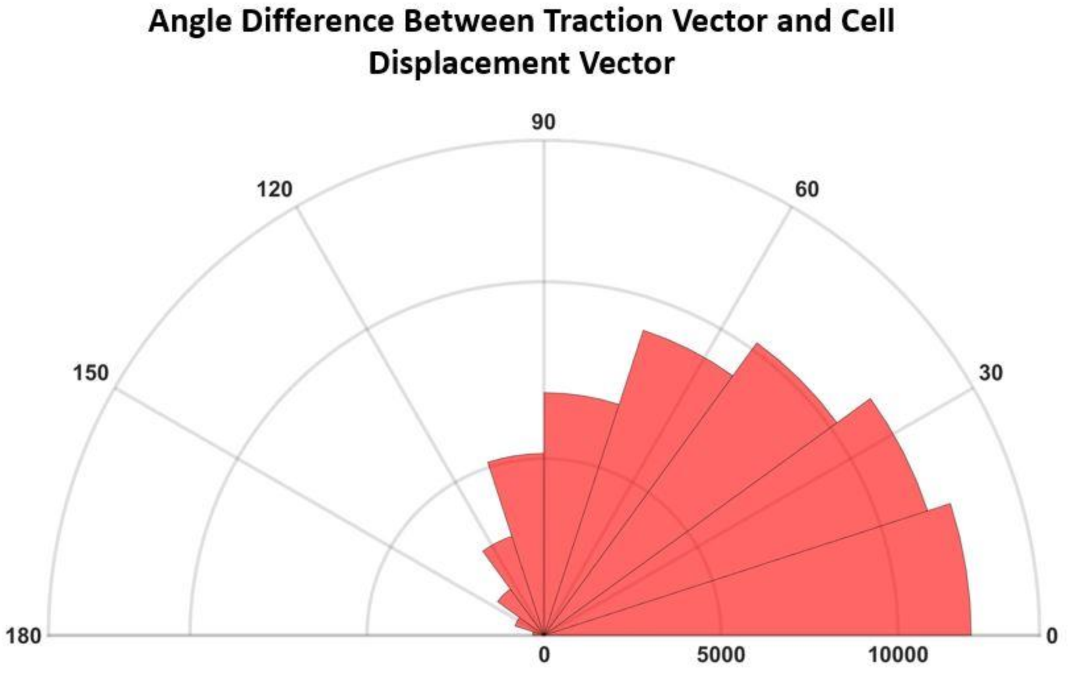

Figure 21: Difference between all tractions and the corresponding displacement vectors

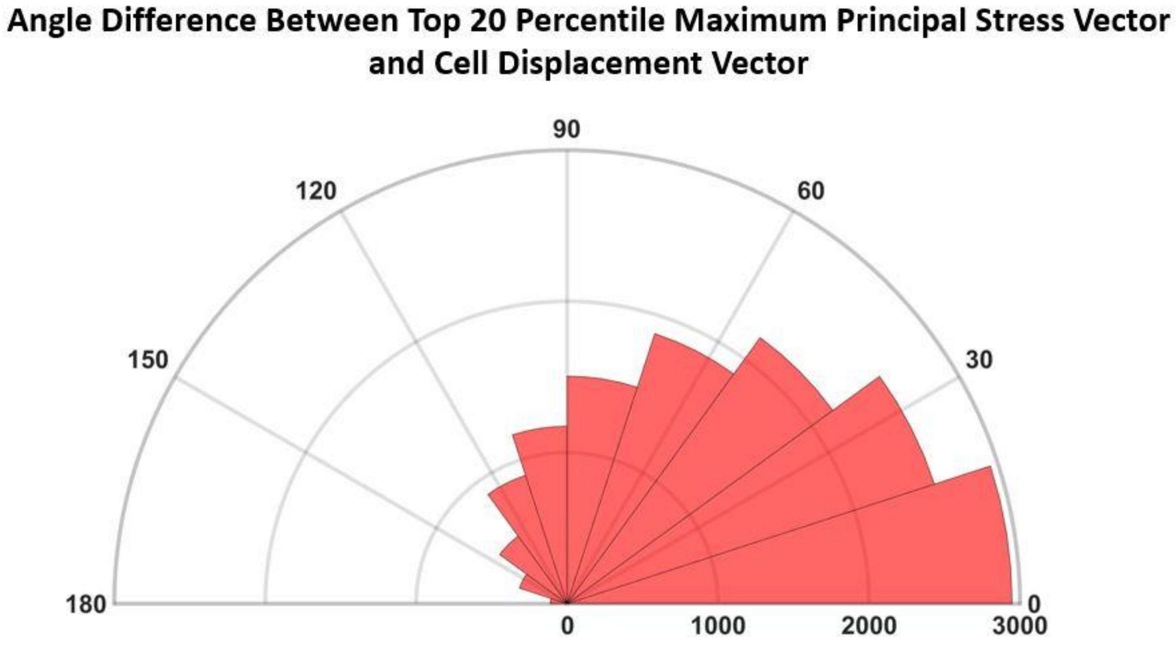

Figure 22: Difference between the top 20 percentile maximum principal stresses and the corresponding displacement vectors (Φ)

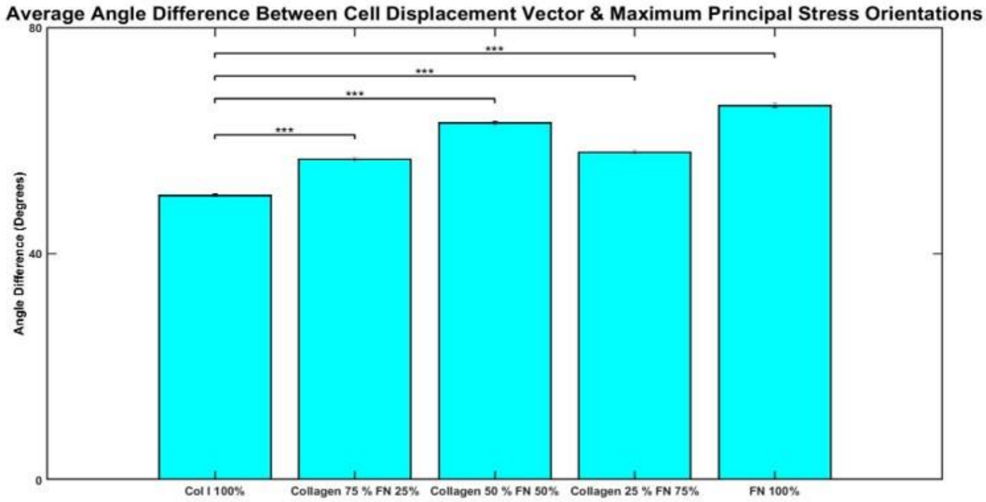

Figure 23: Average Φ calculated for the top 20 percentile stresses for different ECM compositions based on averages from 5 samples (~100-1500 cells) for each ECM ratio

The bar plots for average cell orientations for different ECM ratios didn't show any significant preferential orientations (shown in the results section of the chapter).

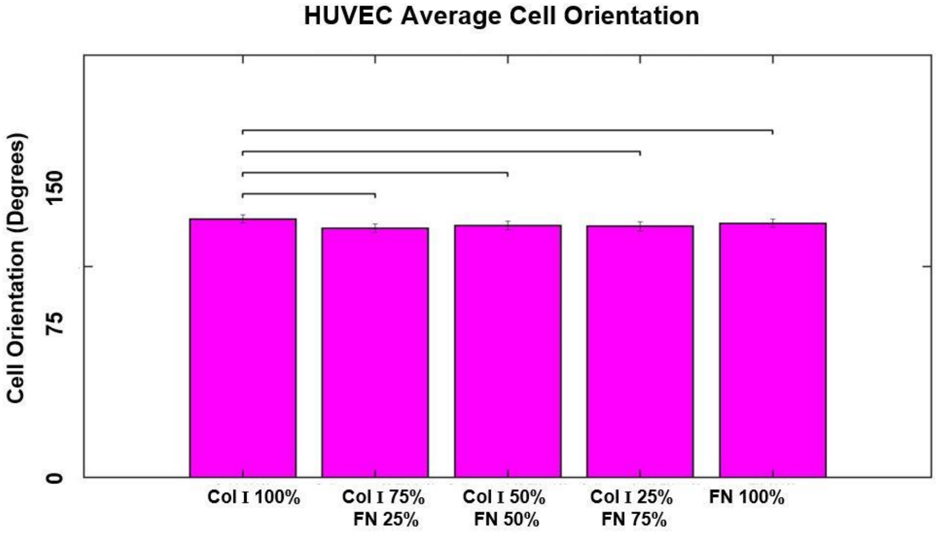

Figure 24: Average cell orientations for different ECM ratios

CHAPTER FIVE: TRACTIONS AND INTRACELLULAR CALCIUM

Introduction

Calcium signaling in the form of transportation of transient Ca^{2+} ions plays an important role in maintaining the physiology of various cell types including endothelial, epithelial, skeletal, neural, and cardiac cells [64]. The regulation of calcium ions is important for various physiological processes such a transcription, contraction (force generation), migration, apoptosis, transcription, etc. [64].

Calcium Signaling and Calcium Pumps

Calmodulin or calcium-binding proteins act as switching compounds attracting positively charged proteins owing to their negative charge [64]. The process of Ca^{2+} ions binding to specific proteins could result in the movement of amino acids and hydrophobic components into the bilayer because of the electrochemical gradient [64]. The calcium stores inside the cell are maintained by constant pumping of Ca^{2+} ions into the endoplasmic reticulum through Sarco-Endoplasmic Reticular Ca^{2+} ATPases (SERCA) pumps [64]. The calcium ions are pushed out of the cell by Plasma Membrane Ca^{2+} ATPases (PMCA) pumps. Other mechanisms include Na^+/Ca^{2+} and Na^+/Ca^{2+}-K^+ exchangers that rapidly regulate transient calcium levels [64]. The fastest exchange of calcium ions within a cell happens through voltage-gated channels called Calcium Selective Channels (CaVs) [64]. The cell to cell calcium signaling occurs via gap junction (connexins) through transmitter gated ion channels [64]. Another important channel is the Transient Receptor Potential (TRP) channel which voltage-gated the intracellular transport of Na^+ and Ca^{2+} ions via plasma membrane channels [64]. Mostly, TRP channels are activated by G-protein-coupled or tyrosine-kinase receptors (TKR) regulated by Phospho-Lipase C (PLC). It is reported that depletion of Ca^{2+} ions by PMCA at a rate faster than SERCAs pump activates the Ca^{2+} Release Activated Current (CRAC) owing to depletion of ER Ca^{2+} [64]. CRAC promotes intracellular Ca^{2+} influx in response to intracellular Ca stores depletion [64]. The G protein-coupled receptors play a primary role in intracellular calcium signaling [64]. Transient intracellular calcium (ca^{2+}) signaling also happens as a response to mechanical stretching induced by fluid shear stresses results in the release of vasoactive molecules from the endothelium which plays an important role in maintaining the vascular tone [12]. The interplay between ATP, ca^{2+}signaling via P2X4 channels were described in [12].

Calcium and Cell Motility

Ca^{2+} is known to influence the motility of the cell as well. The binding of calcium to troponin exposes the actin-binding sites to myosin heads [64]. Calcium also regulated other protein motors such as dynein and kinesin which help in material transportation [64]. Calcium levels also influence the shape of sperm and the motility of white blood cells [64]. The contraction of endothelial and smooth muscle cells is achieved by the activation of voltage-gated L-type (high voltage current) or T-type (low voltage current) calcium channels which trigger the Myosin Light Chain Kinase (MLCK) promoting myosin-ATPase activity [64-66].

Free Calcium Agonists

Thrombin, thapsigargin, and histamine are some of the widely used calcium agonists which increase intracellular free calcium [67]. An example of an antagonist that decreases intracellular calcium is BAPTA tetra-potassium salt [68]. It has been shown that histamine increases the intracellular calcium by binding G protein in the plasma membrane with the help of PLC, releasing inositol triphosphate that triggers the receptors on the endoplasmic reticulum [33]. [69] showed that histamine increases intracellular calcium by releasing calcium stores and due to the influx of extracellular calcium ions. [33] observed how histamine, and fluid shear flow magnitudes affect intracellular free calcium levels in a dose-dependent manner. Histamine is known to induce transient calcium spikes through low voltage-gated T-type calcium channels [66, 70].

Histamine Vascular Physiology

Histamine is contained in mast and non-mast cell stores of the vascular walls. It plays an important role in the body's inflammatory, allergic, and immunological response, and its actions are mediated by four receptors H1, H2, H3, and H4 [71]. Histamine also impacts the vasoactivity of the blood vessel through contraction of the Vascular Smooth Muscle Cells (VSMC). The increase in contractility of VSMC and endothelium permeability due to histamine action is mediated through Ca^{2+} signaling [71]. The transient histamine-induced contractility along with hyperpermeability aids in extravasation and edema formation of fluids during an inflammatory or allergic response [71].

Histamine-induced increase in cytosolic calcium plays an important role in initiating reorganization of actin stress fibers which are responsible for cell contraction and maintaining the integrity of cell shape and cell junctions [72]. Histamine increases the permeability in endothelial cells as evidenced by the transient formation of endothelial gaps [73]. [74] also showed that histamine influences the cell-matrix and cell-cell adhesion sites particularly through

VE-cadherin or cadherin-5. Histamine alters the binding between β-catenin (dual-functional adaptor protein attached to the tail of cadherins) and VE-cadherin resulting in reversible and transient disruption of the barriers [75]. Trans-endothelial electrical resistance was used to quantify the integrity of the cellular barriers or junctional strength [76]. A transient disruption in barrier function was observed as evidenced by a decrease in cell-cell resistance in confluent HUVEC monolayers after histamine addition [74]. However, for subconfluent monolayers where cell-cell junctions were not established, an increase in cell-ECM resistance was observed after histamine addition [74]. Histamine as mentioned earlier increases the activity of MLCK but the rate of phosphorylation is not sufficient to drastically increase the activity of the myosin motors [74]. The mechanism by which histamine alters the monolayer's resistance is not clearly known. Both cell-cell and cell-ECM junctions are believed to play a role in histamine's ability to influence the endothelium mechanics [74].

Effect of Calcium Agonist on Tractions

Doyle et al., [32] investigated the link between stretch-activated calcium intracellular transients and tractions of fish keratocytes. Doyle et al. showed a higher traction increase in the leading rear edge of the cell with peak tractions 20-40 seconds after transient intracellular calcium peaks. The increase in tractions was because of the activity of MLCK after the calcium transient increase followed by a drop in tractions due to retraction as the intracellular calcium level returns to the baseline in most samples [77]. Human Umbilical Vein Endothelial Cell (HUVEC) monolayers were subjected to thrombin which increased the intracellular calcium levels and isometric tension [77]. Increased isometric tension from the HUVEC monolayers was observed within 5 minutes of agonist thrombin addition and the peak elevated average tension lasting for about 50-60 minutes [77]. However, a dose-dependent traction response for different agonist concentrations has not been reported.

Although traction response based on calcium transients for a single cell was shown by Doyle et al., dose-dependent traction response of the cells as a function of transient calcium levels for different agonist concentrations such as histamine has never been done so far. Histamine is known to disrupt cell-cell barriers via VE-cadherins but its influence on cell-ECM junctions is unknown. This work will shed light on the relationship between transient calcium levels induced by different histamine concentrations and the subsequent change in tractions (Cell-ECM stresses) over time as the result of the Ca^{2+} intracellular transients.

Materials and Methods

Cell Culture

Human Umbilical Vein Endothelial Cells (HUVECs) used in the experiments were cultured in Medium 200 with 2.153% Large Vessel Endothelial Supplement (LVES) solution. HUVECS, Medium 200, and LVES were purchased from ThermoFisher. HUVECs from passages 12-14 were cultured in 0.1% Gelatin (Sigma-Aldrich) coated flasks at 37^o C and 5% CO_2 prior to running all the experiments.

Polyacrylamide Gel Fabrication

The protocol for preparing Polyacrylamide (PA) gels can be found in [57]. Glass bottom petri dishes (35 mm, Cellvis) were treated with bind silane solution for 45 minutes after which the dishes were rinsed with DI water and air-dried. PA solution is made by mixing ultra-pure water, 40% acrylamide (Bio-Rad), 2% bis-acrylamide (Bio-Rad), and fluorescent beads (yellow or Texas red with ~0.5 µm diameter, Invitrogen). The stiffness of the PA gel can be fine-tuned by changing the ratio of Bis(acrylamide) and acrylamide solutions. The PA solution is kept in a vacuum chamber for 40 minutes. 10% ammonia persulfate and TEMED (N,N,N′,N′- tetramethylethane-1,2-diamine) were added to the de-gassed PA solution which initiates polymerization reaction. After the addition of ammonia persulfate, TEMED the PA solution is mixed well and plated on the petri dish wells. Hydrophobic coverslips were then placed on top of the PA solution after which the dishes were inverted to allow more fluorescent beads to settle on the top layer of the polymerizing gel. The subsequent PA-gels with stiffness ~1.2 kPa (mimicking the stiffness of the healthy endothelium) and height ~100 µm were used for the experiments [58].

SANPAH Burning & Col I-FN Treatment

The petri dish with PA gels were then subject to treatment with sulfosuccinimidyl-6-(4-azido-2-nitrophenylamino) hexanoate (Sulfo-SANPAH; Proteochem) dissolved in 0.1 M HEPES buffer solution (Fisher Scientific) and kept under a UV lamp for 8 mins. After SANPAH and UV treatments, the samples were treated with 0.1 mg/ml concentration of type 1 Collagen (Col-I).

After the treatment of Col-I (Advanced Biomatrix) overnight at 4^o C, the excess protein solution was carefully removed and HUVECs were seeded at a density of ~50×10^4 cells/mL. After 60-75 mins, 2 ml of M200 was added to each petri dish. Petri dish containing HUVECs on hydrogels were incubated at 37^o C and 5% CO_2 for at least 24 hours prior to experimentation.

Loading Calcium Dyes

The HUVECs (P12) cultured on the polyacrylamide hydrogels for almost 24 hours were washed twice with PBS and treated with 5µM of Fura 2 am dye and incubated at 37° C and 5% CO_2 for 30 minutes. The 5µM of Fura 2 am was prepared by diluting 50µg of Fura 2 am in 50µL Dimethyl Sulfoxide (DMSO) and 10 mL of phenol red-free M200. After 30 minutes of loading the cells with Fura 2 am dye, the cells were washed thrice with PBS to remove any excess Fura 2 am, and fresh M200 was added. The HUVECs were incubated for another 30 minutes at 37° C and 5% CO_2 with M200 before imaging. The loading of cells with calcium dyes was performed in a dark setting to reduce photobleaching. The loaded samples were immediately imaged after 60 minutes the cells were treated with Fura 2 am. For the experiments, histamine dichloride with three different concentrations 1mg/ml (5.5 mM), 1.5mg/ml (8 mM), and 2mg/ml (11 mM) were used.

Calcium Imaging

The change in intracellular free calcium levels changes the maximum fluorescence of Fura 2 am dyes by shifting the peak of the excitation wavelength in the excitation spectrum. As the free calcium level increases, the fluorescence of Fura 2 am (measured at an emission wavelength of 510nm) also drops almost linearly for an excitation wavelength close to 380nm, and an inverse trend of linear increase in fluorescence was observed for the 340 nm excitation wavelength. The true calcium concentrations can be linked to the fluorescence of Fura 2 am measured for a single or dual wavelength. The use of two-wavelength pairs (340nm/380nm) is called ratiometric imaging and the actual calcium levels can be calculated by measuring the fluorescent intensities based on maximum, minimum, and actual ratios of the two wavelengths. The maximum (R_{max})

and minimum intensity (R_{min}) ratios along with dissociation constant (K_d), and factor β (ratio of intensities in 380nm channel for free and saturated calcium) calculated with the help of calcium buffer kits is enough to measure the calcium concentration (M). The detailed theory of the calcium calibrations with relevant formulae based on Grynkiewicz et al. [78] can be found in [79].

Similarly, for a single channel, calcium concentration (M) can be calculated as follows:

$$Ca^{2+} = \frac{[F_{Free} - F]}{[F - F_{Sat}]} \times K_d$$

where F_{Free} is the intensity of the channel with free Fura 2 am (no calcium)

$F_{Saturated}$ is the intensity of the channel with maximum Ca^{2+} levels from the buffer kit (saturated calcium)

K_d is the dissociation constant (268 nM at 37^{o}C and pH = 7),

F is the fluorescence intensity measured during the experiments,

For our experiments, a single LED channel with a 385 nm excitation wavelength was used to quantify the change in calcium levels.

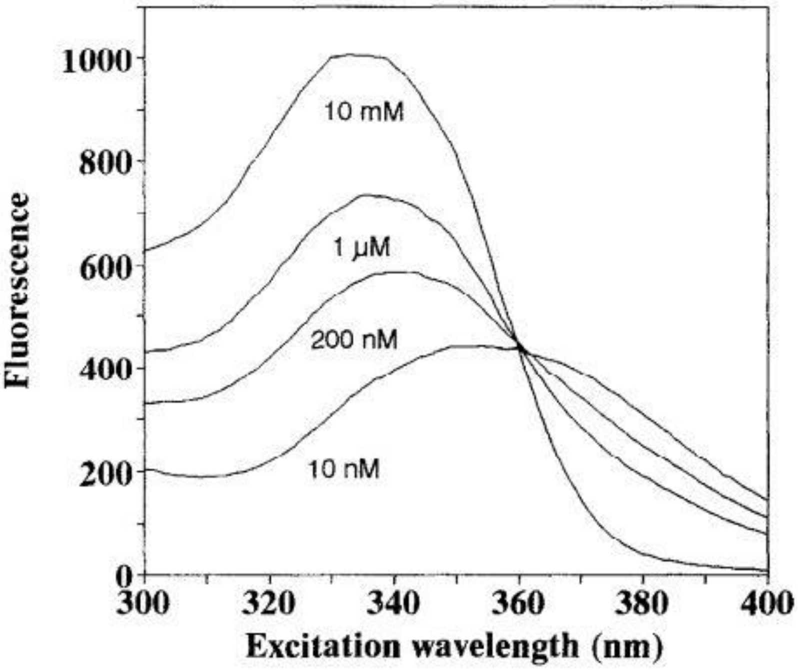

Figure 25: Fura 2am excitation spectra for select Ca^{2+} concentrations [79]

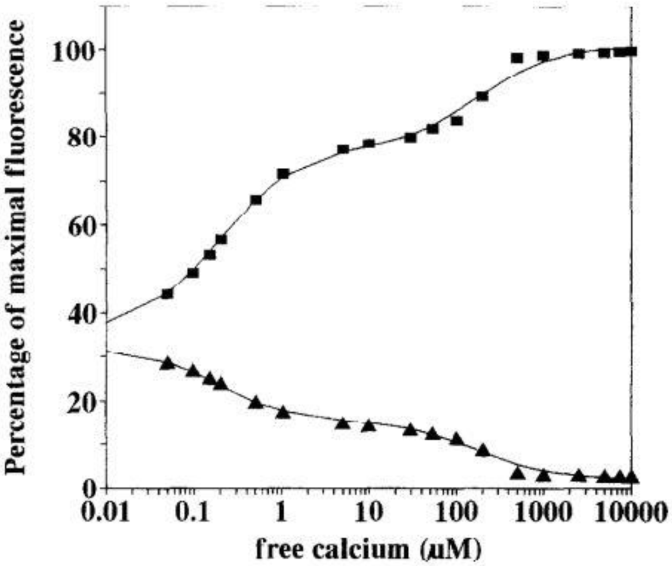

Figure 26: Fura 2am maximal fluorescence response for different free calcium levels using 340nm(squares) and 380nm(triangles) excitation channels and emission at 510nm [79]

Imaging Methodology

The HUVEC samples were imaged with the help of a Zeiss inverted microscope with 20X objective & Hamamatsu camera with 4×4 binning. Images were taken every 2 seconds using a 385nm excitation (50% intensity) channel with emission fluorescence measured at 510nm for Fura 2 am calcium imaging and 594nm channel (100% intensity) for fluorescent bead displacements. The exposure was set close to ~40-50 ms for each channel. The histamine-mediated calcium response was very quick, and the time interval of 2 seconds was chosen to be able to capture the transient increase in calcium levels as reported in other journals [32]. Histamine dichloride (Ca^{2+} agonist) and BAPTA tetrapotassium salt (Ca^{2+} antagonist) were both diluted in PBS.

Experimental Protocol

The samples were imaged after drawing the region of interest (ROIs) of the individual cells in the field of view. Histamine dichloride was added at the end of the 10th cycle (~20 seconds) since acquiring the first image. The same volume of PBS was also added around the 150th cycle (~300 seconds) and the cells were trypsinized at the end of the 160th cycle (~320 seconds) to capture the reference bead configuration for the traction stresses computation. The calcium imaging was done in a static setting and the addition of histamine (pipetted by hand in one steady motion) induced noise in tractions. Hence a vehicle control with PBS was also done to show the drop in fluorescence due to histamine and traction noise-induced due to pipetted fluids. Data were acquired for each of the three histamine concentrations: 1mg/ml, 1.5mg/ml, 2mg/ml. The chosen concentrations were several folds higher than what was mentioned in shear flow experiments. However, because of the static conditions, the Fura 2 am -calcium fluorescence in the cells was only sensitive to histamine concentrations above 0.5mg/ml. Also, the 385nm Colibri LED channel produces a lesser fluorescence signal compared to xenon arc lamp-based imaging as shown [80].

Data Analysis

For calcium imaging, a blank rectangular ROI (Region of Interest) was chosen which was subtracted from the intensities measured in the rest of the ROIs across the entire time series to reduce the impact of background noise on the measured fluorescence. The mean calcium intensities from the 385nm channel were also normalized on the scale of 0 to 100 to compare with the background-subtracted calcium response from other histamine concentrations.

For the traction analysis, traction data from the 20th cycle to the 80th cycle (20-140 seconds after histamine addition or 40 to 160 seconds since imaging) to compare the influence of histamine concentrations and calcium levels on tractions. The initial 20-second traction data after histamine addition were neglected for final comparison due to noise-induced by pipetted fluids. Also, from the fluorescence response shown in the figures, it was observed that an increase in calcium levels was sustained for ~20 seconds before calcium levels drop back to the baseline (Figure 30). According to Doyle et al., the increase in tractions was mostly observed for tractions around the 90th percentile. Hence, only maximum traction contribution within each ROI was considered for the data analysis for the select time. However, maximum RMS and average RMS tractions observed were almost similar irrespective of the histamine concentration (shown in figures 34 and 35 and also in the supplementary).

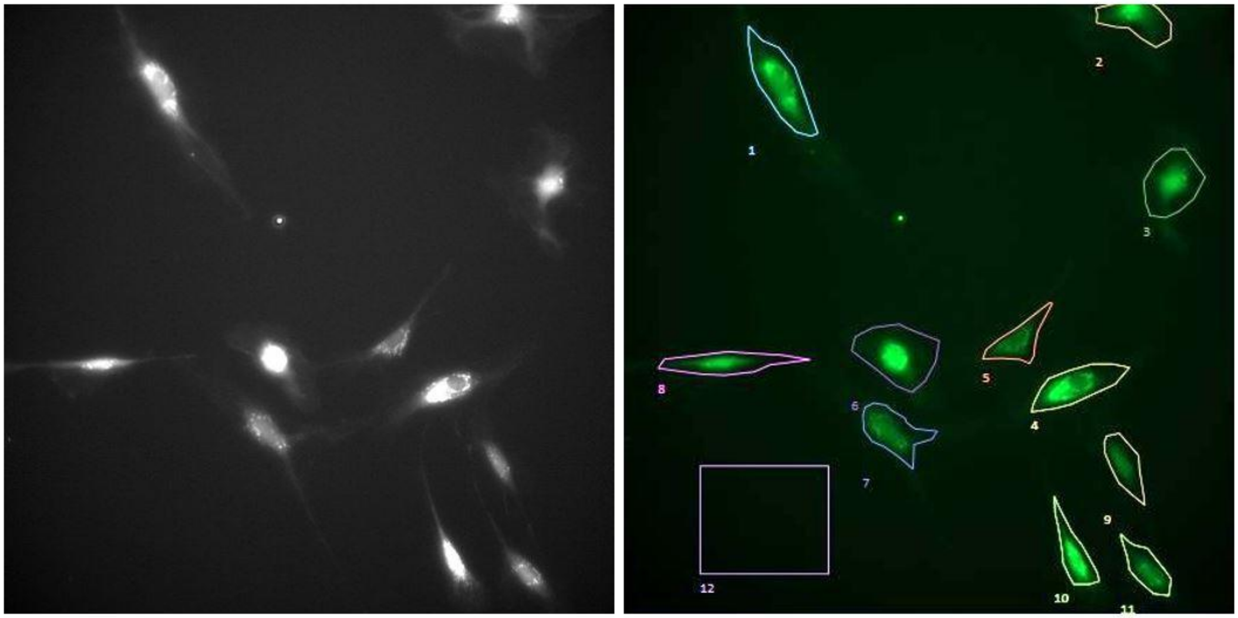

Figure 27: Fluorescence intensity of Fura 2am measured using 385nm channel(left) and ROIs selected for the intensity measurements along with a background ROI(right)

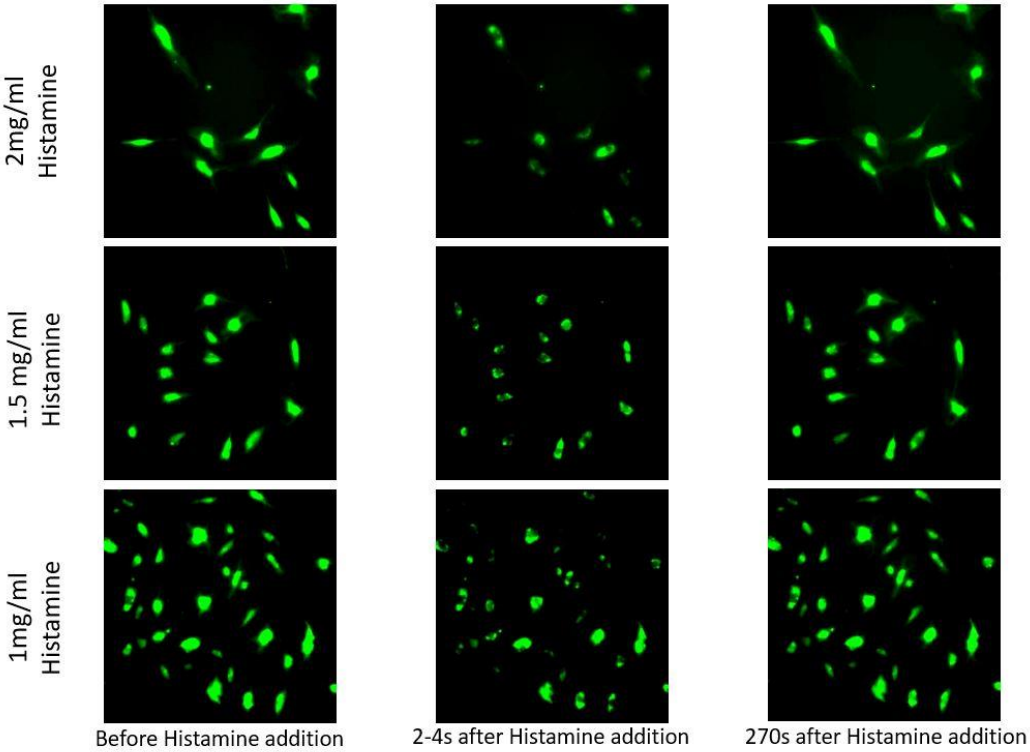

Before Histamine addition

2-4s after Histamine addition

270s after Histamine addition

Figure 28: Fura2am fluorescence response to different doses of histamine

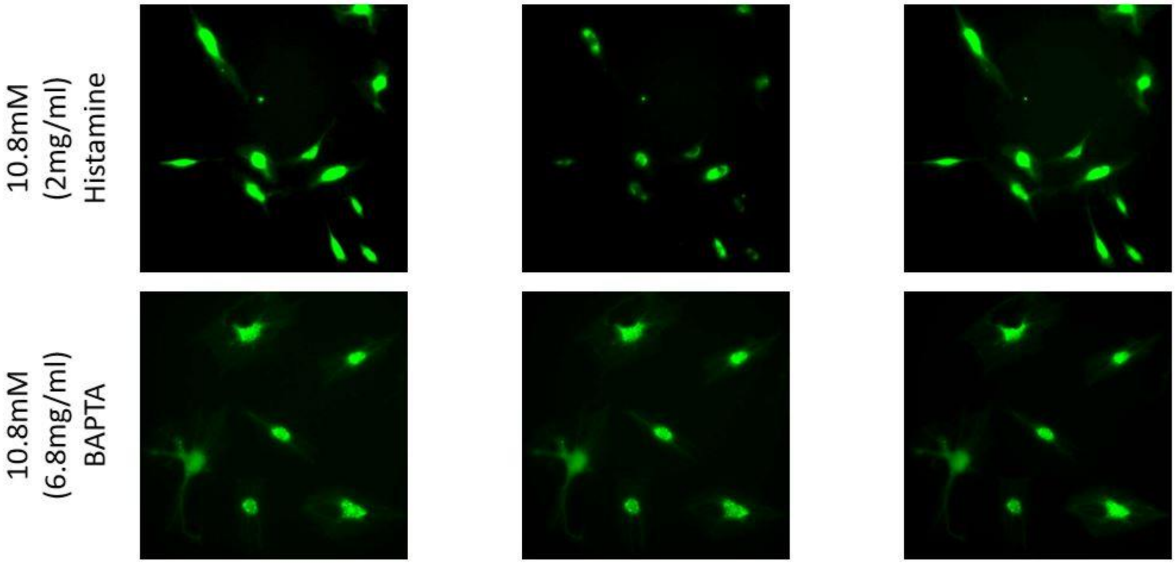

Before Histamine/BAPTA addition

2-4s after Histamine/BAPTA addition

270s after Histamine/BAPTA addition

Figure 29: Fura2am fluorescence response to 10.8mM doses of histamine and BAPTA

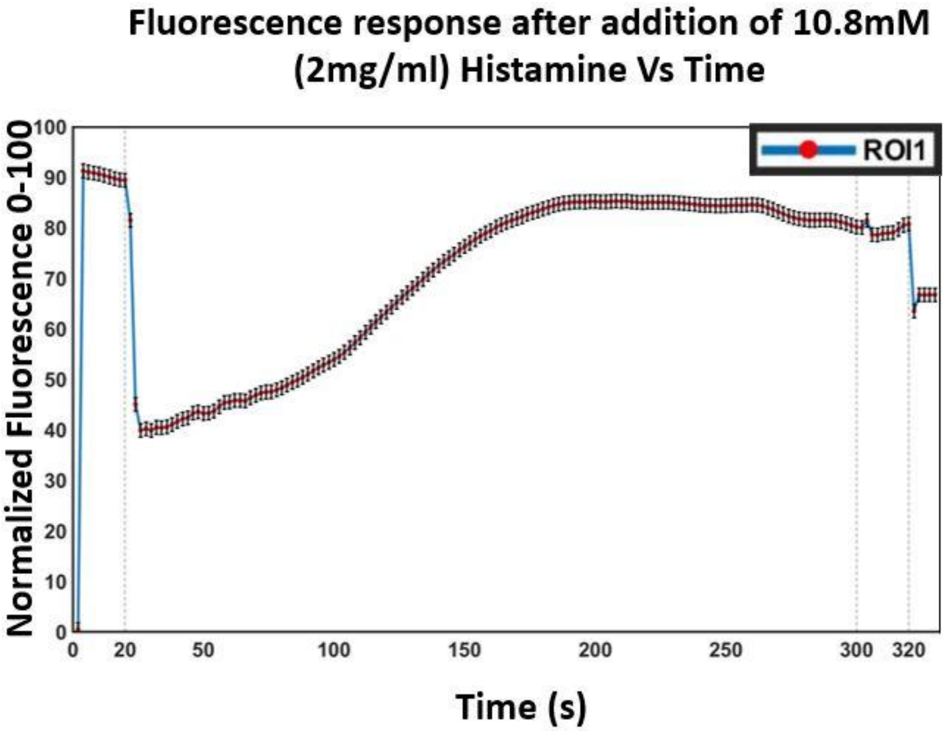

Figure 30: Normalized Fluorescence response to 10.8M (2mg/ml) Histamine Vs Time

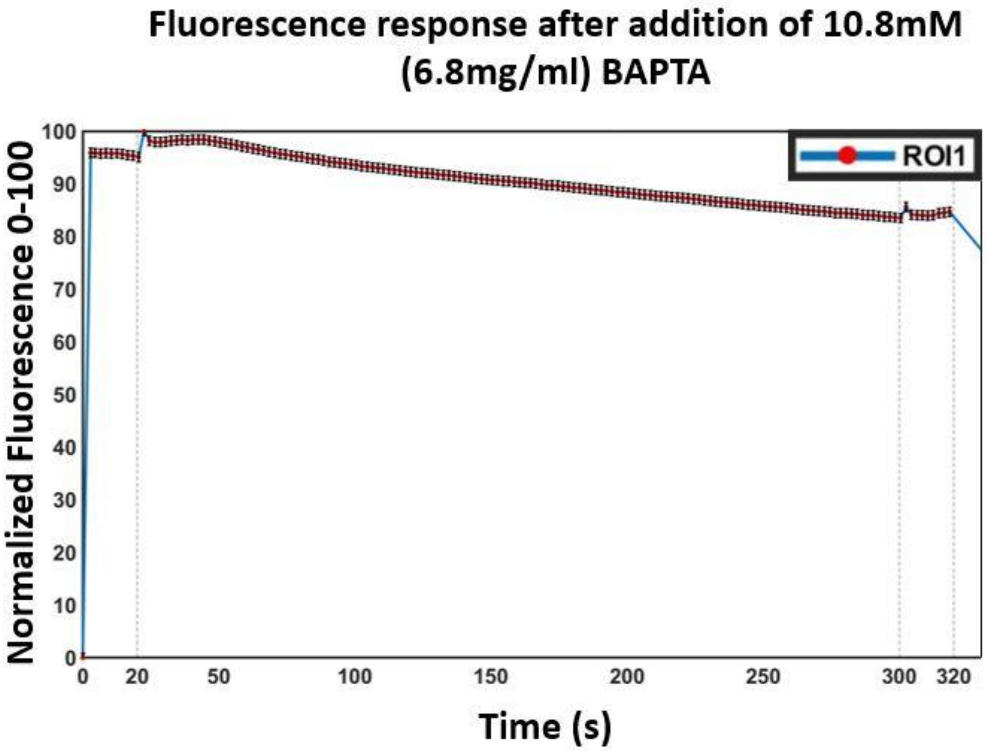

Figure 31: Normalized Fluorescence response to 10.8M (6.8mg/ml) BAPTA Vs Time

In figures 30 and 31, the three vertical dotted lines represent the time histamine/BATA diluted in PBS (20th second), PBS (300th second), and 10X Trypsin (320th second) were added. From figures 28 and 30, it is evident that histamine dichloride acts as an agonist increasing the intracellular calcium levels (drop in measured Fura 2 am fluorescence to 385nm channel excitation). Similarly, calcium chelator BAPTA Tetrapotassium salt (calcium chelator) acts as an antagonist reducing the intracellular calcium levels as evidenced by a small spike in measured fluorescence (refer to figures 29 and 31).

Results

A drop in the fluorescence intensity of Fura 2 am was observed after histamine addition based on excitation from the calcium 385nm channel which was consistent with what was reported previously [79]. The average percentage drop in fluorescence intensities varies for different histamine concentrations used. As expected, the highest drop was observed with 2mg/ml histamine concentration followed by 1.5mg/ml and 1 mg/ml respectively. Also, a slight increase in maximum RMS tractions was observed for three different histamine concentrations and again the increase in tractions was the highest for 2mg/ml concentration. Only the time between 40-160 seconds was chosen for the analysis as the slight increase in tractions was only seen during that period as background RMS noise starts to settle (figures 34 and 35).

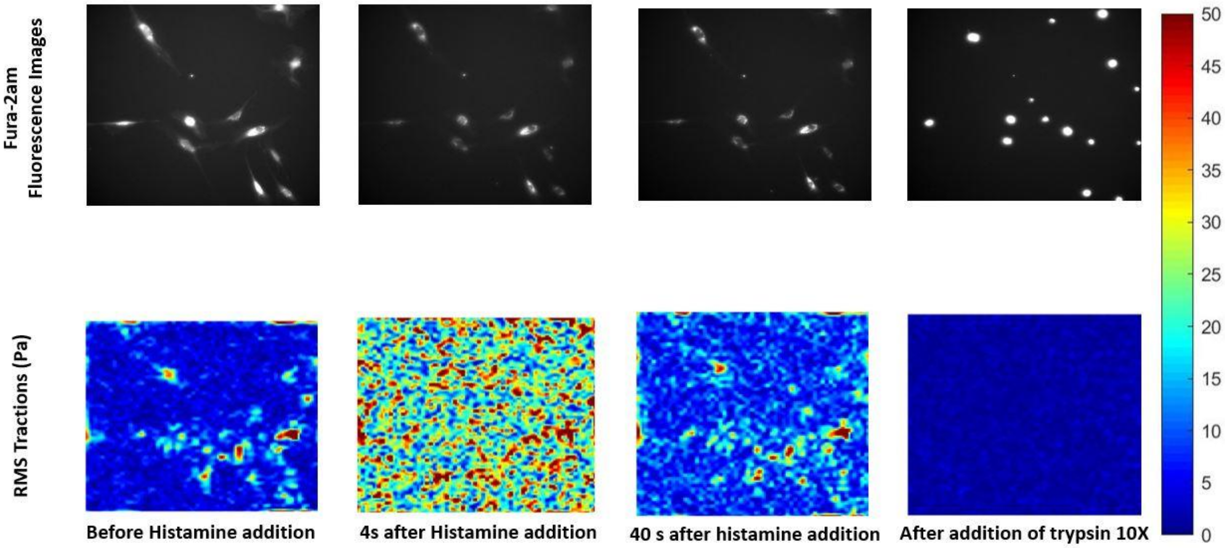

Figure 32: RMS traction (Pa) at select times for 2mg/ml histamine addition

Figure 32 shows the RMS tractions measured from TFM and the corresponding fluorescence response from 385nm wavelength excitation. From the RMS tractions for the entire field of view, maximum and average RMS traction contributions for each individual cell ROI were extracted.

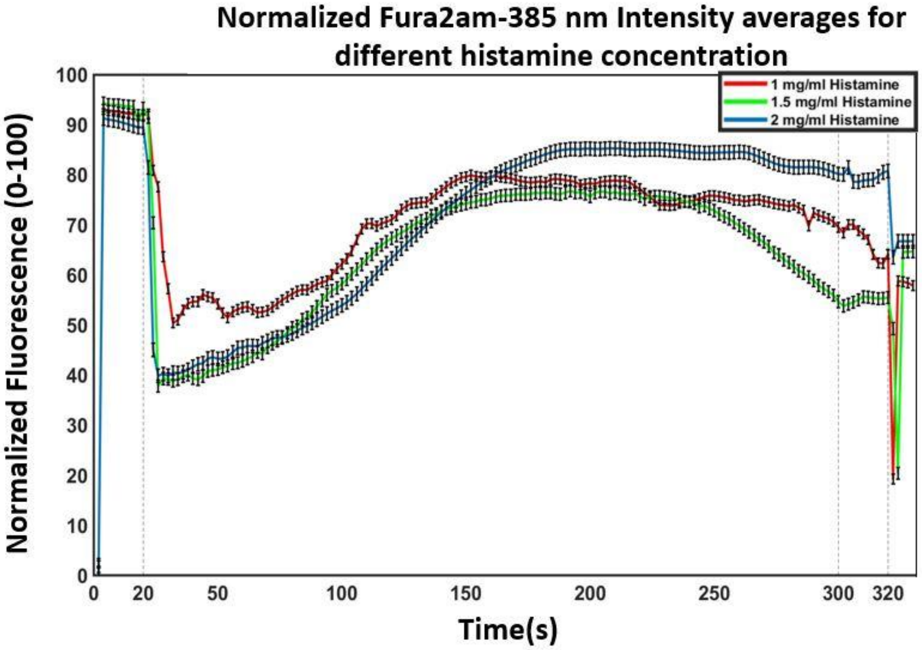

Figure 33: Overall average fluorescence intensity response (normalized) for different histamine concentration: 1mg/ml (red line 63 ROIs), 1.5mg/ml (green line 24 ROIs), and 2mg/ml (blue line 43 ROIs)

Figure 33 shows the overall intracellular free calcium levels in terms of normalized fluorescence drop from the 385nm excitation channel for different histamine concentrations. It is seen that the peak fluorescence drop due to histamine (calcium agonist) action was sustained for ~30 seconds (20-50 seconds in figure 23).

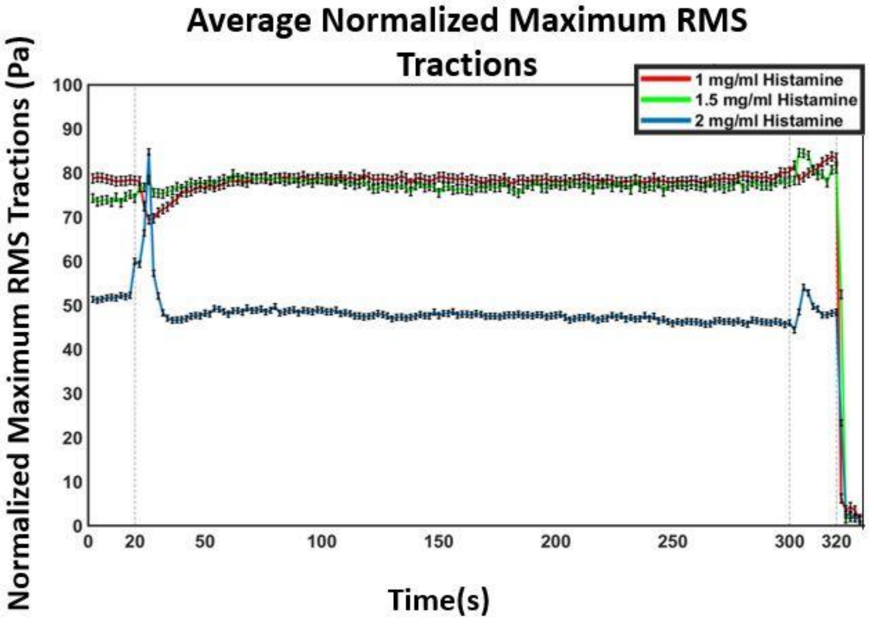

Figure 34: Overall average maximum RMS traction response (normalized) for different histamine concentration: 1mg/ml (red line 63 ROIs), 1.5mg/ml (green line 24 ROIs), and 2mg/ml (blue line 43 ROIs)

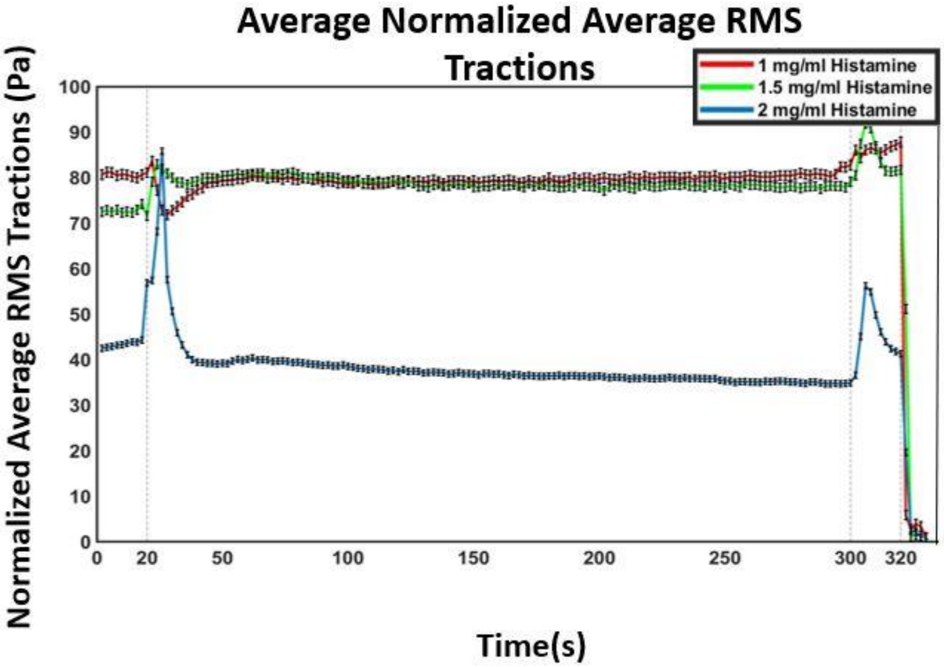

Figure 35: Overall mean average RMS traction response (normalized) for different histamine concentration: 1mg/ml (red line 63 ROIs), 1.5mg/ml (green line 24 ROIs), and 2mg/ml (blue line 43 ROIs)

Figures 34 and 35 represent the maximum and average RMS tractions (normalized from 0-100) based on averages from all the ROIs for different histamine concentrations as shown. It can be seen that both the maximum and average RMS tractions were almost similar. However, only maximum tractions were considered for further analysis to be consistent with the previous reports as mentioned earlier[32]. The average RMS traction response plots were also shown in the supplementary.

For the final analysis, only data from 40-160 seconds were considered with data measured at the 40th second as the baseline. The slight change in tractions was only observed during this period after which the tractions stabilized as shown in figure 34 and figure 35.

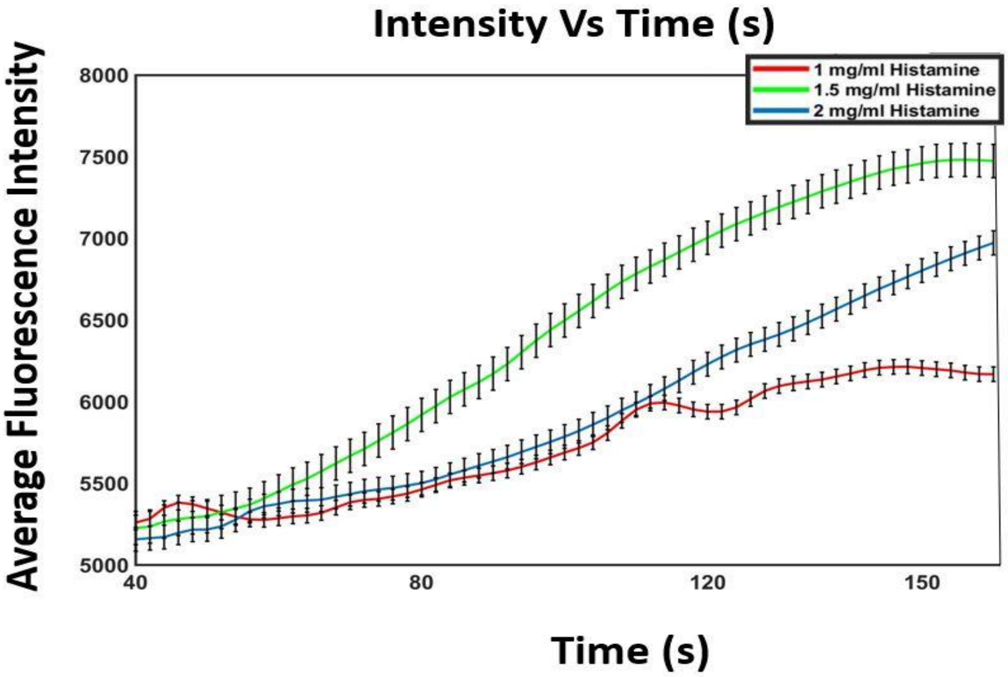

Figure 36: Average fluorescence intensity (Y- axis) response from 40th second to 160th second (20-140 seconds after histamine addition) for different histamine concentrations with error bars

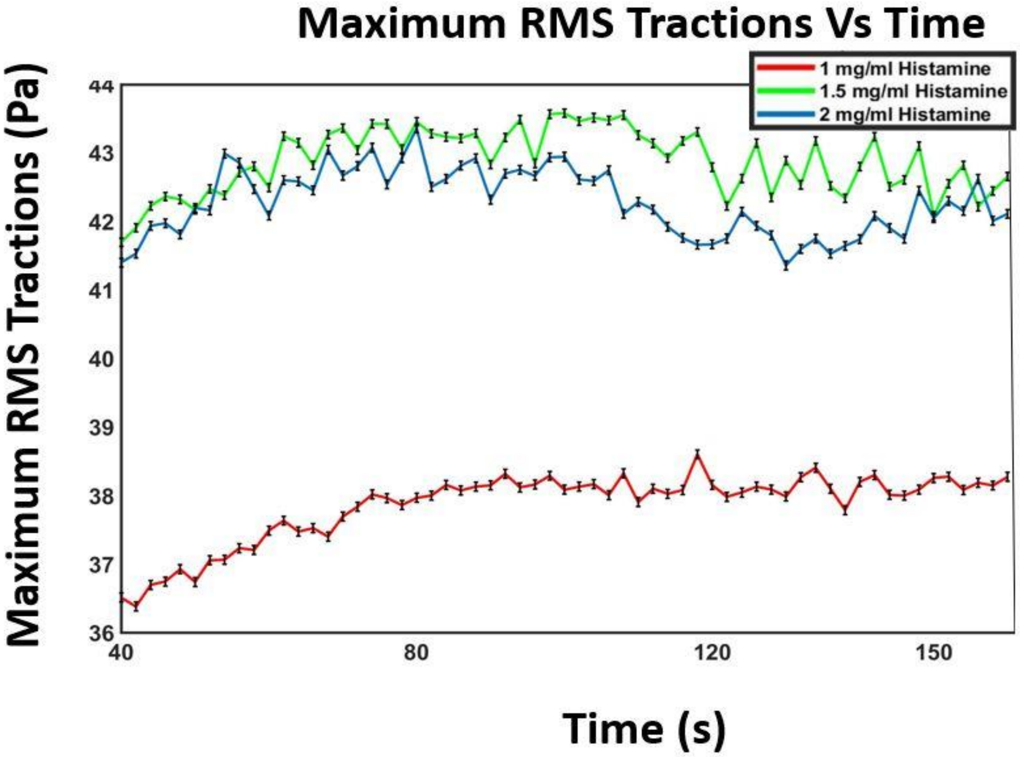

Figure 37: Maximum RMS Tractions (Y- axis, Pa) response from 40th second to 160th second (20-140 seconds after histamine addition) for different histamine concentrations with error bars and time (X-axis, s)

Figure 36 and figure 37 represent the overall fluorescence (calcium levels) and maximum RMS tractions for three different histamine concentrations for the select period of time (40-160 seconds). Figures 38-40 represent both the average maximum RMS tractions (Pa) and fluorescence intensity (inverse relation to calcium levels) responses from 40-160 seconds.

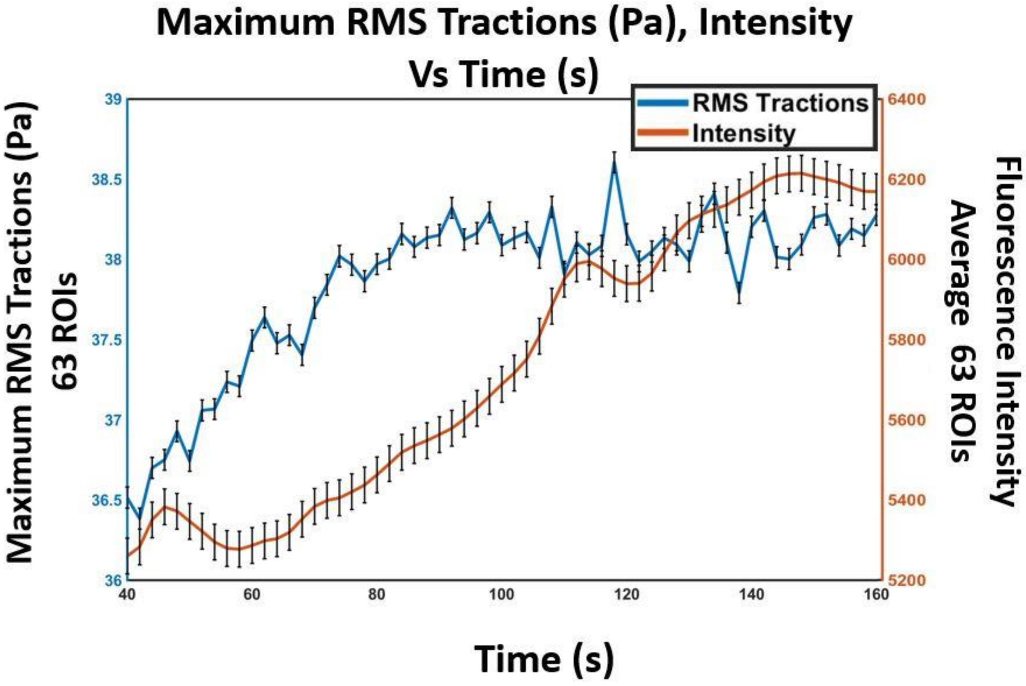

Figure 38: Maximum RMS Traction (Pa) and fluorescence intensity response from 40th second to 160th second for 1mg/ml (histamine added at the end of the 20th second)

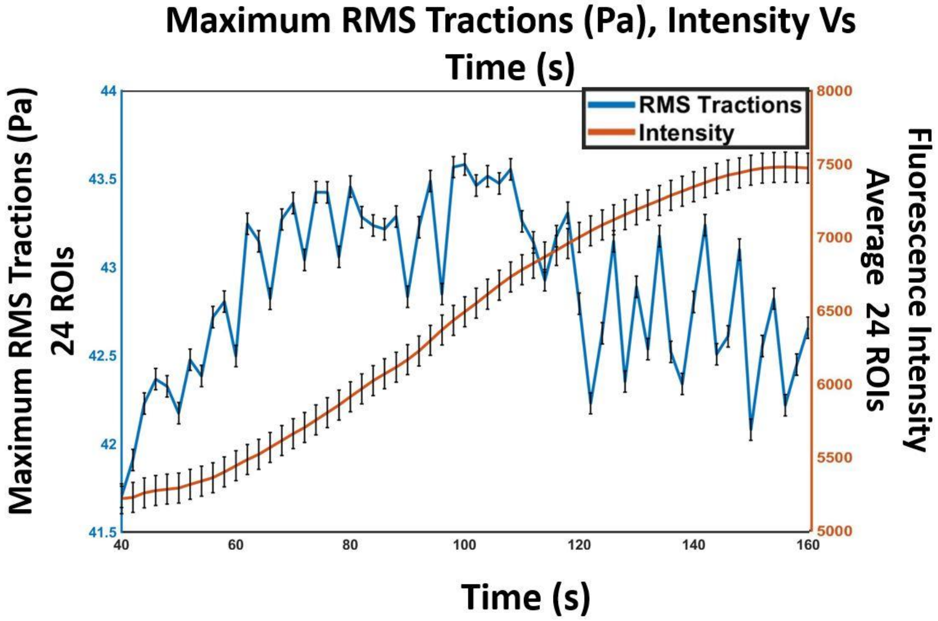

Figure 39: Maximum RMS Traction (Pa) and fluorescence intensity response from 40th second to 160th second for 1.5mg/ml (histamine added at the end of the 20th second)

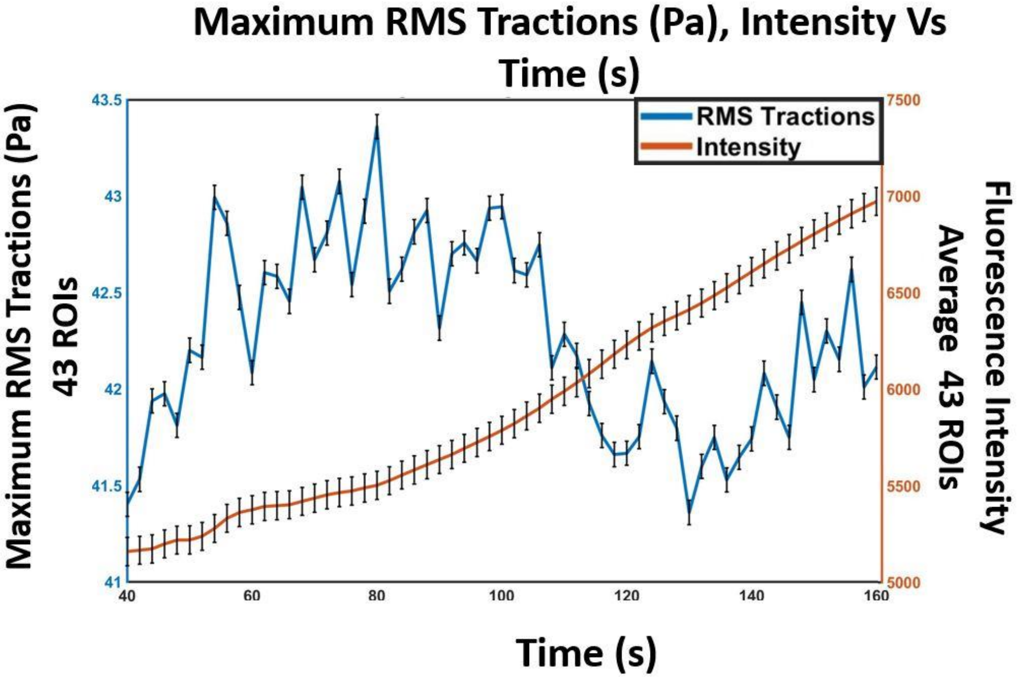

Figure 40: Maximum RMS Traction (Pa) and fluorescence intensity response from 40th second to 160th second for 2mg/ml (histamine added at the end of the 20th second)

Figures 38-40, represent the average maximum RMS tractions and corresponding fluorescence intensity from 63 ROIs (1mg/ml), 24 ROIs (1.5mg/ml), and 43 ROIs (2mg/ml) for the select time (cycles 20-80 or time 40-160 seconds or time 20-140 seconds after histamine addition).

The results show a slight increase in RMS tractions but not drastically high which is consistent with the theory described in [74]. From the results, it can be alluded that histamine doesn't alter the cell-ECM mechanics as much as cell-cell junctions as reported in the journals [73-75]. Therefore, it is the mechanics of cell-cell junctions that dominate (reduce) the traction behavior rather than vice versa due to histamine action.

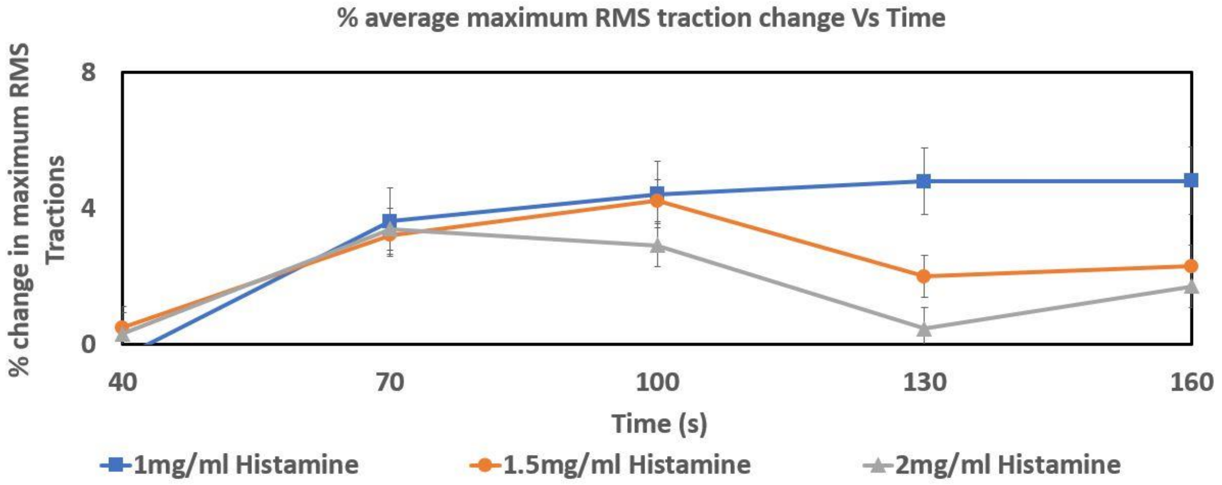

Figure 41: Average % change in maximum RMS tractions Vs Time(s)

Figure 41 above shows that there is a slight increase in tractions for the select period (40-160 seconds) based on averages from 63, 24, and 43 ROIs for 1 mg/ml, 1.5mg/ml, and 2mg/ml histamine addition respectively. The maximum RMS traction value at the 40th second (20 seconds after histamine addition or 20th cycle since imaging) was used as the baseline for calculating the % change. The formula used for calculating the % change is given below

% maximum traction change = [(Baseline – Average maximum RMS traction)/Baseline] × 100

where,

Baseline = Average maximum RMS traction at 40th second since imaging for each histamine concentration

Average maximum RMS traction = Average maximum RMS traction from (42-160 seconds for each histamine concentration

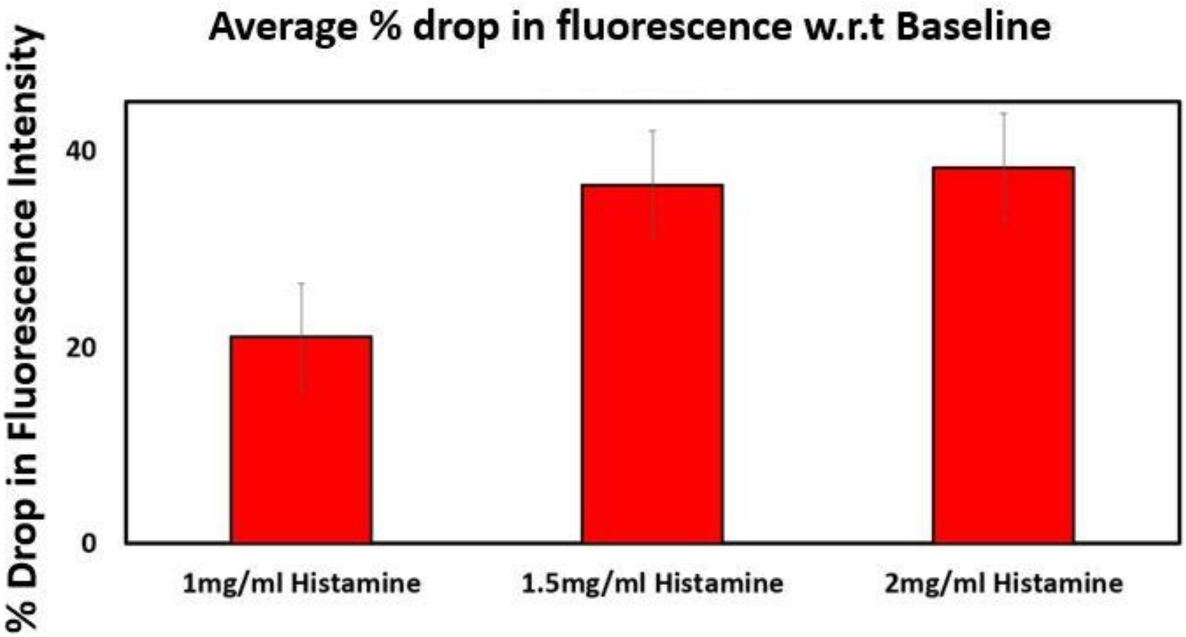

Figure 42:Overall average % drop in fluorescence intensity for different histamine concentrations based on averages from 9 cycles before and 9 cycles immediately after histamine addition

The intensity drop after histamine addition happens within seconds the histamine was added (see figures 30 and 33). The overall % drop in fluorescence due to histamine (shown in figure 33) was calculated using the below formula.

%Drop = [(Baseline – Average Intensity Drop)/Baseline] × 100

where,

Baseline = Average from 9 cycles before histamine addition (Cycles 2-10; 4-20 seconds data)

Average Intensity Drop: Average of 9 cycles (16-24) after histamine addition (32-48 seconds data)

The fluorescence intensity due to 385nm excitation channel starts to return close to the baseline from 50-150 seconds (figures 30 and 33).

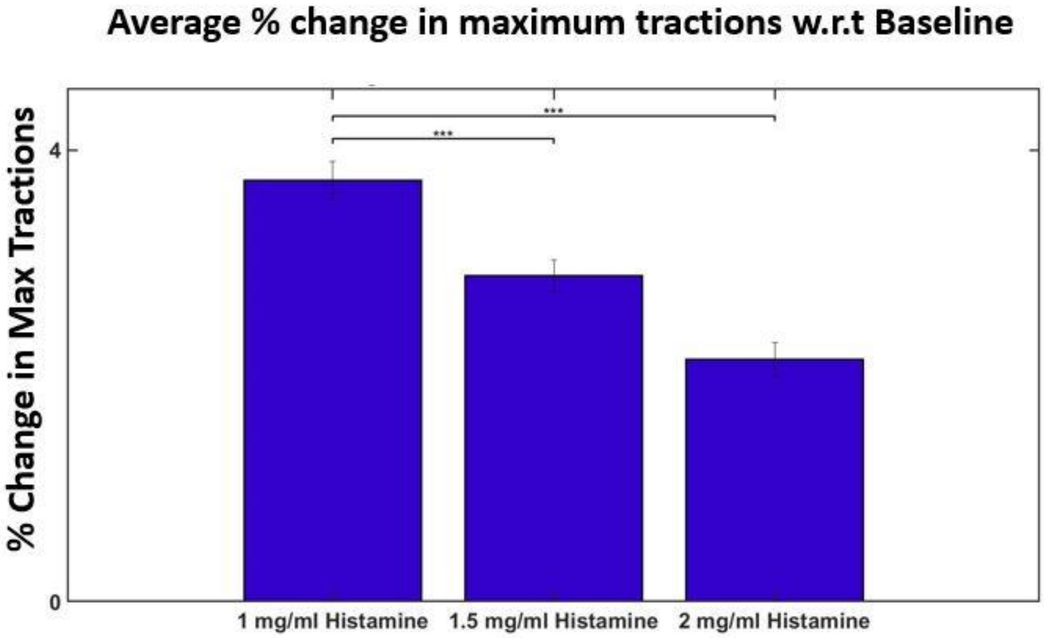

Figure 43: Overall average % change in maximum RMS tractions for different histamine concentrations

Figure 43 shows that there was a very slight increase in tractions compared to the baseline maximum RMS traction at 40th second (20 seconds after histamine addition). The formula to calculate the % change in maximum tractions is given below:

Formula = [(Baseline –Max Traction)/Baseline] × 100

where,

Baseline = Maximum RMS traction at 40th second

Max Traction = Average maximum RMS traction from time 42-160 seconds (21-80 cycles)

% Change: Based on averages from cycles 21-80 (60 data points); 2min data since 20 sec after histamine addition)

For all the analysis the average values from 63 ROIs for 1mg/ml, 24 ROIs for 1.5mg/ml, and 43 ROIs for 2mg/ml respectively.

Machine Learning Classification Analysis

Machine Learning (ML) models capable of classifying agonist (histamine) concentration using calcium level (% drop in fluorescence), average percent maximum tractions change, and cell area as the predictors were built, and their accuracies were tested against unseen observations. The % drop in fluorescence for each ROI was calculated as mentioned in Figure 33 (histamine added after 10th cycle) where the baseline is average from 9 cycles before histamine addition (cycles 2-10) and the peak average intensity drop was calculated from 9 cycles after the histamine addition (cycles 16-24). Similarly, the average percentage change in maximum tractions was calculated based on average from 16 cycles (cycle 35-50 or 70-100 seconds) where the peak changes in the tractions were observed (refer to figures 34 and 35).

The classification analysis was done for two doses of histamine: high (2mg/ml) and low (1mg/ml). In total there were 106 observations (43 for 2mg/ml and 63 for 1mg/ml as mentioned in the previous sections). The data from these 106 observations were randomly shuffled and the first 76 observations were used for training the ML models while 30 observations were held for testing the accuracies of the models.

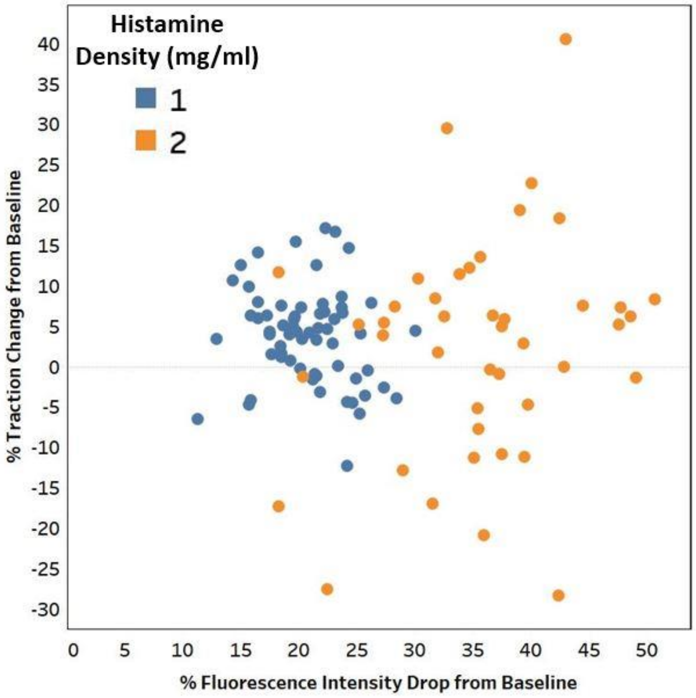

Figure 44: % Average Percent Maximum Traction Change Vs % Fluorescence Intensity Drop

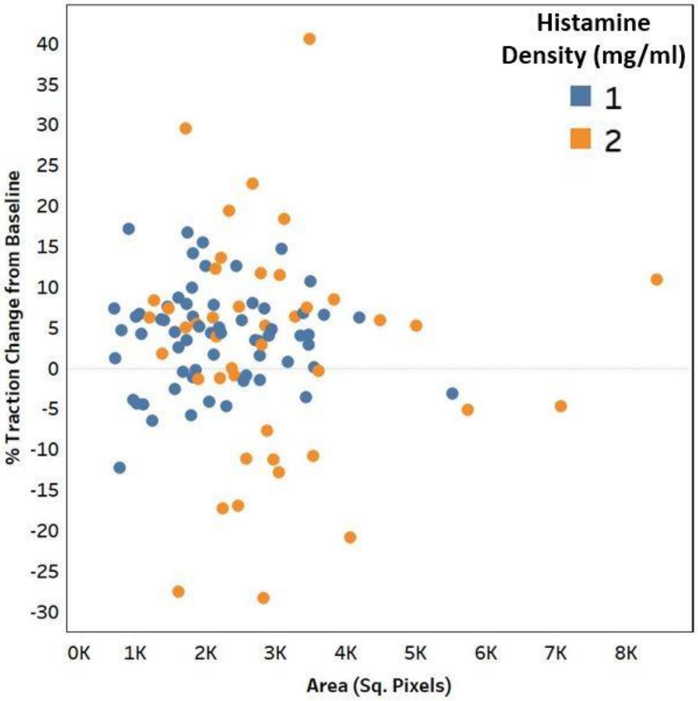

Figure 45: Average Percent Maximum Traction Change Vs Area (Sq. Pixels)

The 76 observations forming the training table were used to train the ML models available in the MATLAB 2019a Classification Learner application with 5-fold cross-validation. The best four validation accuracies were observed for the Kernel Naïve Bayes (KNB), K- Nearest Neighbor (KNN), Quadratic Support Vector Machine (QSVM), and Logistic Regression (LR) models. The above models were picked based on the validation accuracy after training the models.

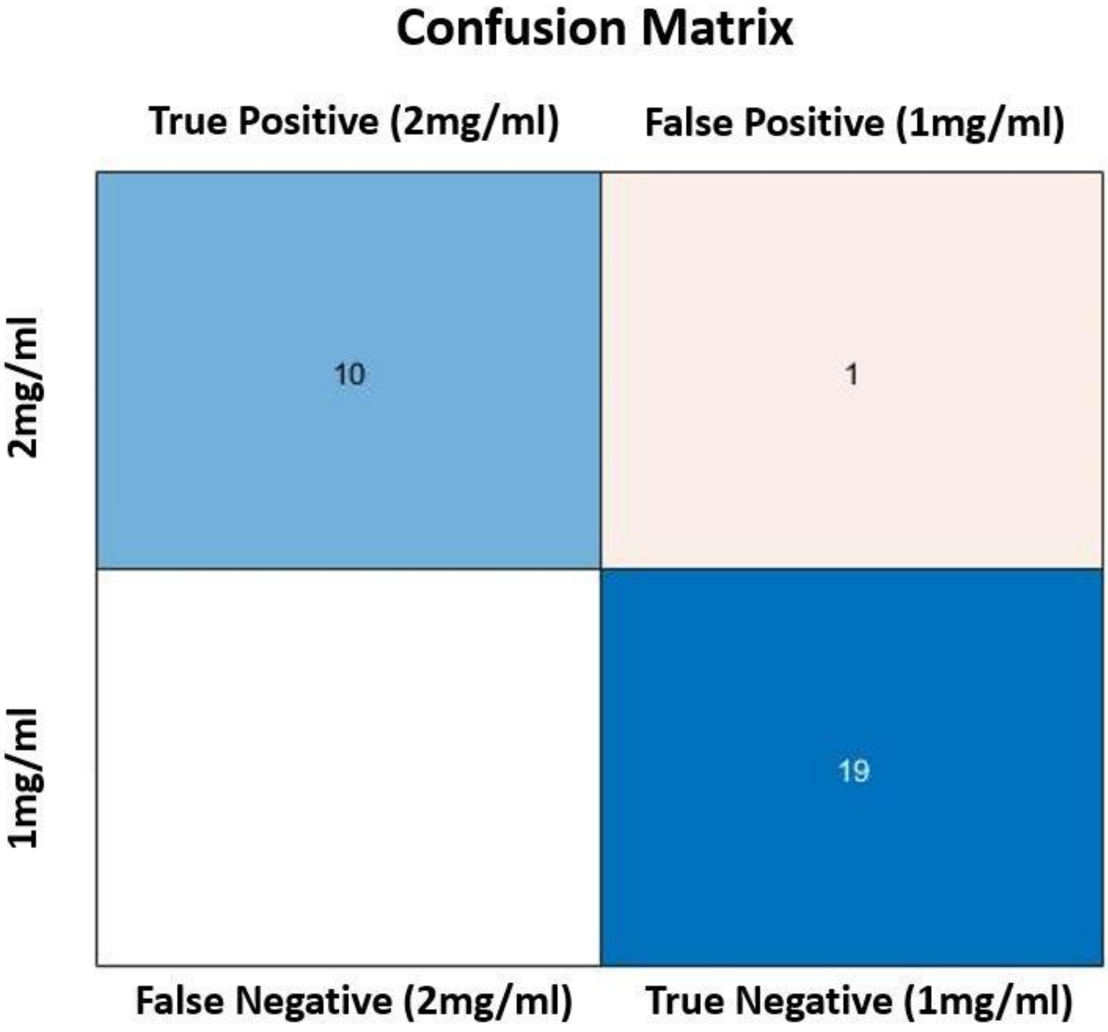

Figure 46: Classification Predictions for high (Positive) and low (Negative) histamine doses using Kernel Naive Bayes (KNB) Predictions (correct predictions in light/dark blue; incorrect predictions in light peach)

An example confusion matrix for KNB classifier predictions on 30 unseen observations was shown above. The model successfully classified all of the low (1mg/ml or negative) histamine data and wrongly classified 1 observation that was actually high (2mg/ml or positive) as low (1mg/ml or negative). The above predictions were made after saving the model to the MATLAB workspace and using the predict function to make the classifications for the 30 observations that the model didn't see. The same procedure was done for training, importing, and making predictions using other models. Accuracy was calculated by finding the ratio of the number of correct classifications to the total number of observations (96.67% for KNB from the confusion matrix). Area Under Receiver Operating Characteristics (AUROC) is another metric used to assess the performance the classification models.

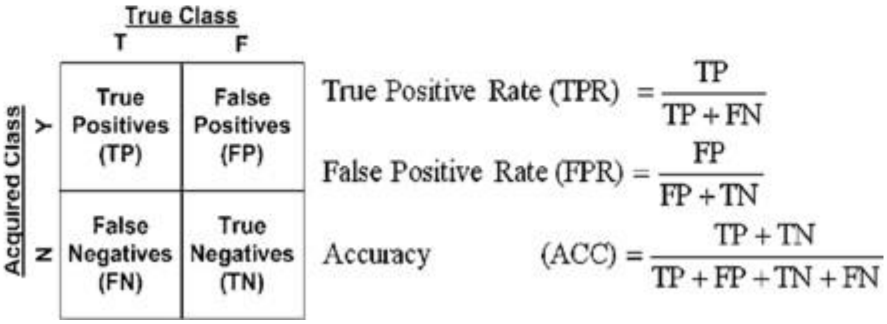

Acquired Class	True Class T	True Class F
Y	True Positives (TP)	False Positives (FP)
N	False Negatives (FN)	True Negatives (TN)

$$\text{True Positive Rate (TPR)} = \frac{TP}{TP + FN}$$

$$\text{False Positive Rate (FPR)} = \frac{FP}{FP + TN}$$

$$\text{Accuracy (ACC)} = \frac{TP + TN}{TP + FP + TN + FN}$$

Figure 47: AUROC Calculation using True Positive and False Positive Rates

AUROC is the area under the curve for true and false positive rate plots. The formula in figure 47 gives this AUROC accuracy.

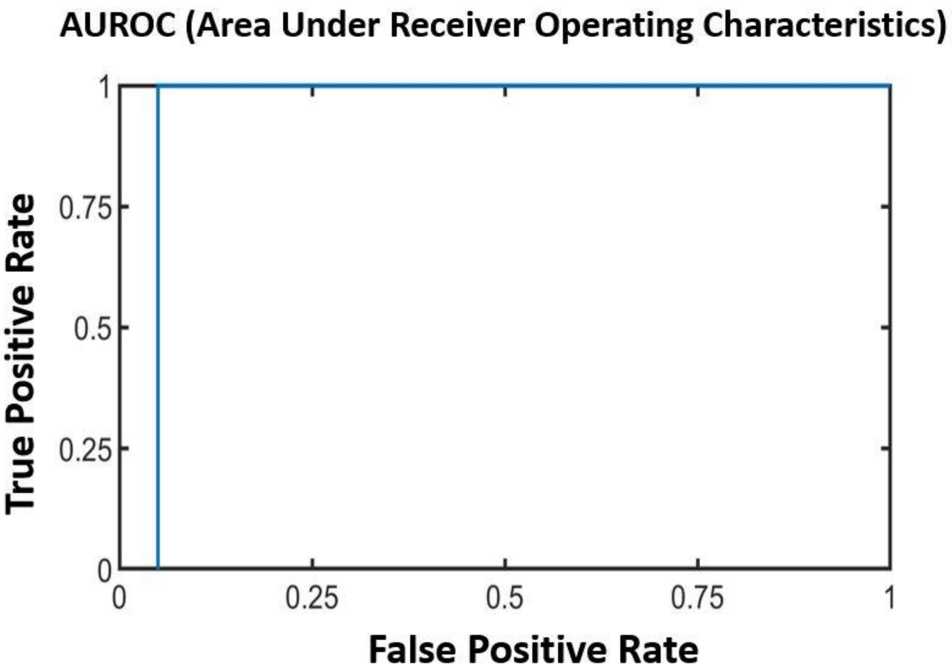

Figure 48: AUROC for KNB classification predictions for the test data (30 unseen observations)

The highest accuracy (100%) was observed for QSVM model which was able to classify all the unseen 30 observations correctly. The list of accuracies from the selected ML models is shown below.

Table 1: Classification Prediction Accuracies of the ML Models for the Test Data (30 unseen observations)

Models	**Accuracy (%)**	**AUC (%)**
Kernel Naive Bayes (KNB)	96.67	95
K- Nearest Neighbor (KNN)	96.67	97.37
Quadratic Support Vector Machine (QSVM)	100	100
Logistic Regression (LR)	90	92.11

Machine learning (ML) regression models were also developed which predicted average maximum tractions utilizing % drop in fluorescence, histamine concentration, and the cell ROI as the predictors (shown in the supplementary) demonstrating the scope for ML models for predicting biochemical doses or cell mechanics.

Conclusion

% Drop in fluorescence was proportional to histamine concentrations: 1 mg/ml (21.03%), 1.5mgml (36.53%), and 2mg/ml (38.35%) but no correlation was observed between the calcium levels (histamine concentrations) and the corresponding change in maximum tractions. Only a very slight increase but an inverse relationship was observed for the average maximum RMS traction increase (during 42-160 seconds) for different histamine concentrations: 1 mg/ml (3.73%), 1.5mgml (2.88%), and 2mg/ml (2.15%) respectively (averages from 42-158 seconds) after which the tractions stabilized. Histamine-induced calcium increase via low-density current (T type) channels didn't produce any significant changes in the tractions although greater % changes were seen for higher doses of histamine suggesting they regulate the mechanics mostly via cell-cell junctions. However, accuracy as highest as 100% for unseen 30 observations (high (2mg/ml) and low (1mg/ml) histamine data) using quadratic support vector machine (QSVM) for classifying histamine concentrations based on fluorescence intensity, area of ROI, and average % traction change. ML regression models for predicting maximum tractions based on histamine-induced calcium levels had only a moderate correlation suggesting that they could be a better predictor of intercellular stresses than tractions (shown in the supplementary section).

Supplementary

The calcium response for different cell ROIs along with a blank ROI (control) was shown.

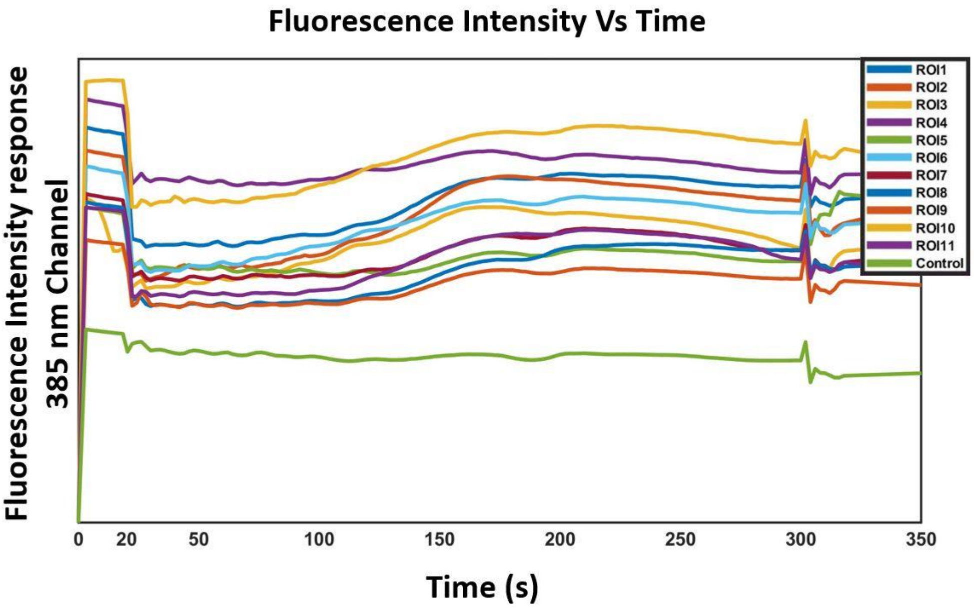

Figure 49: Mean fluorescence intensity measured every 2 seconds for 12 ROIs including the fluorescence of background ROI (bottom green line) after 2mg/ml histamine addition at the end of the 20th second

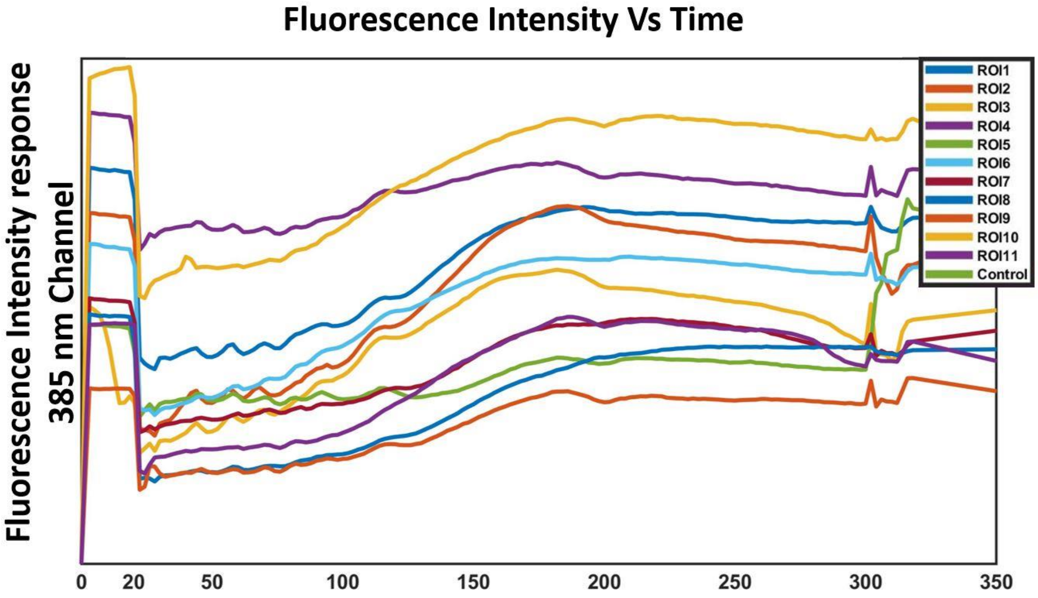

Figure 50: Mean fluorescence intensity time response for 11 ROIs with background fluorescence subtracted (2mg/ml histamine added at the end of the 20th second)

The average RMS tractions and maximum RMS tractions were similar as shown in the results section of this chapter (figures 34 and 35). The average tractions and maximum RMS tractions were similar for the select time (40-160 seconds) as shown in the figures below.

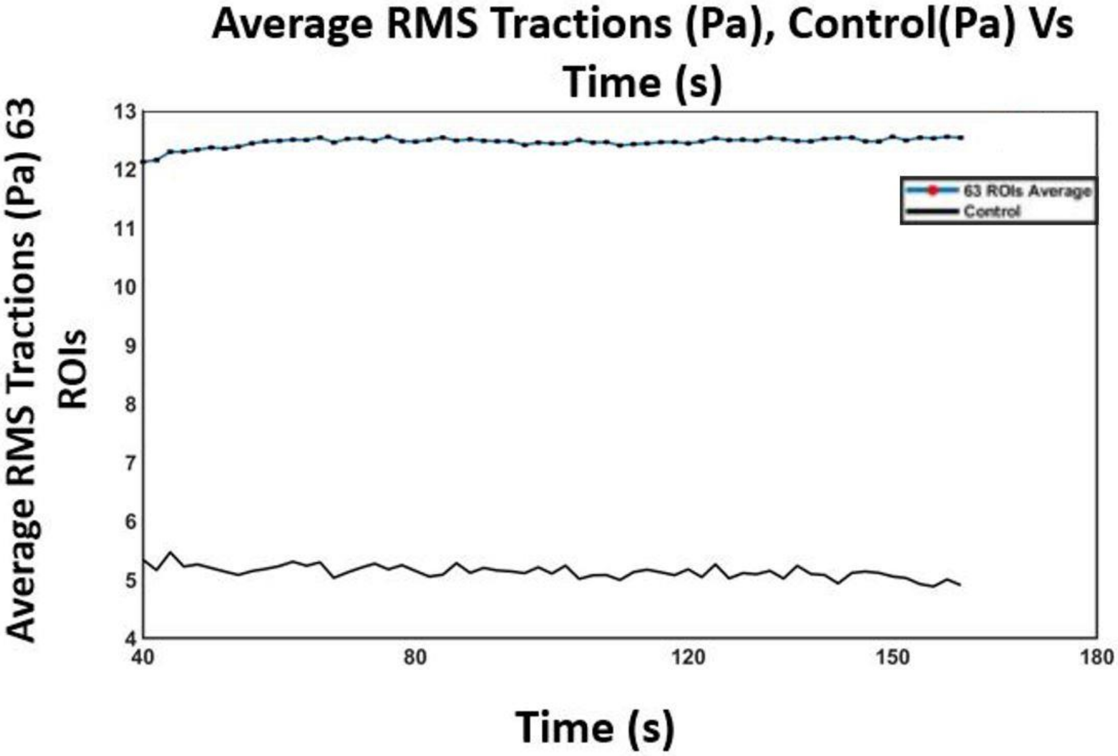

Figure 51:Mean of average RMS tractions for 63 ROIs and control (ROI with no cells) for the select time (40-160 seconds) after 1mg/ml histamine addition

The above figure shows the average RMS tractions mean from 63 ROIs and the corresponding control (no cells) 20 seconds (10 cycles) after 1mg/ml histamine addition. Similarly, the average maximum RMS for 63 ROIs with the corresponding control was shown in figure 52. The response was similar except for the magnitudes. Hence, for the final analysis, only the average maximum RMS tractions were used to compare the dose-dependent response to different calcium levels.

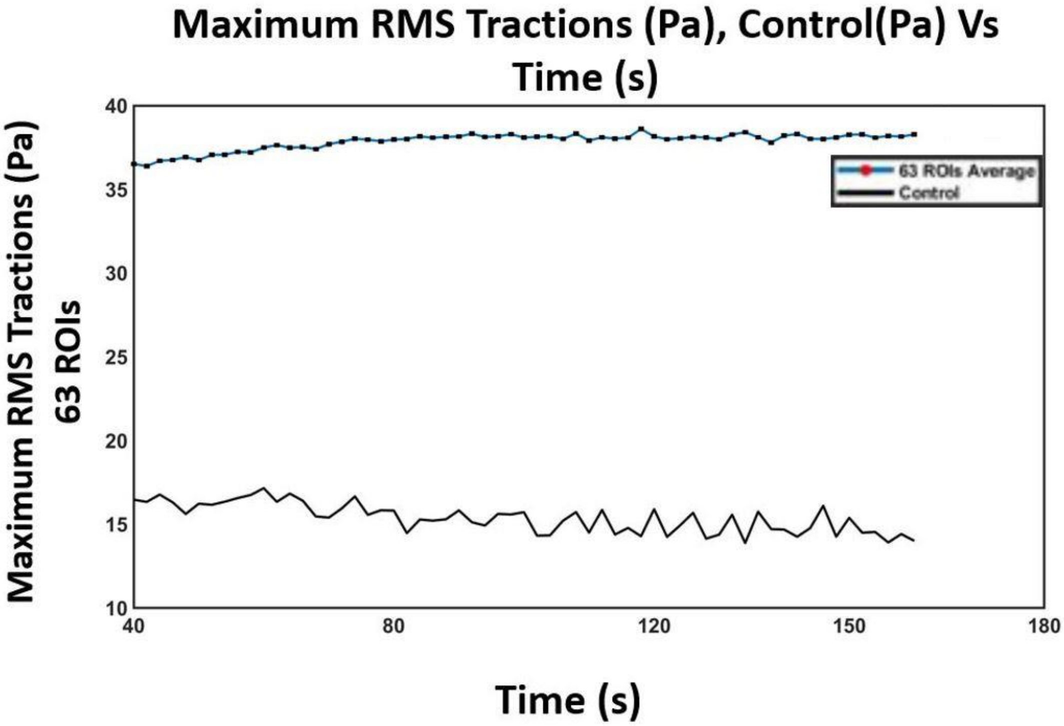

Figure 52: Mean of maximum RMS tractions for 63 ROIs and control (ROI with no cells) for the select time (40-160 seconds) after 1mg/ml histamine addition

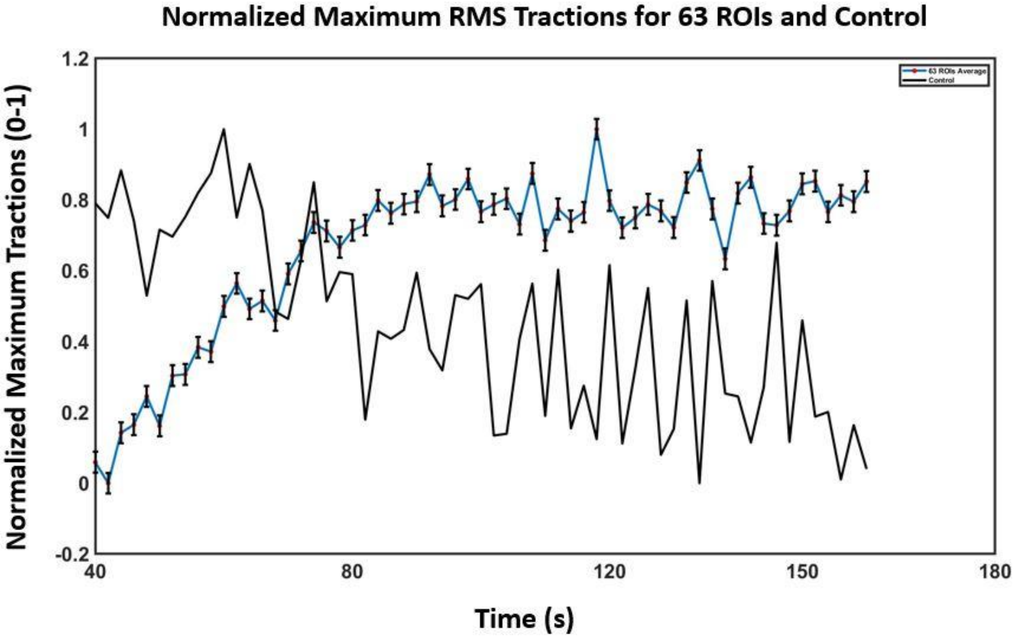

Figure 53: Normalized mean maximum RMS tractions for 63 ROIs and control (ROI with no cells) for the select time (40-160 seconds) after 1mg/ml histamine addition

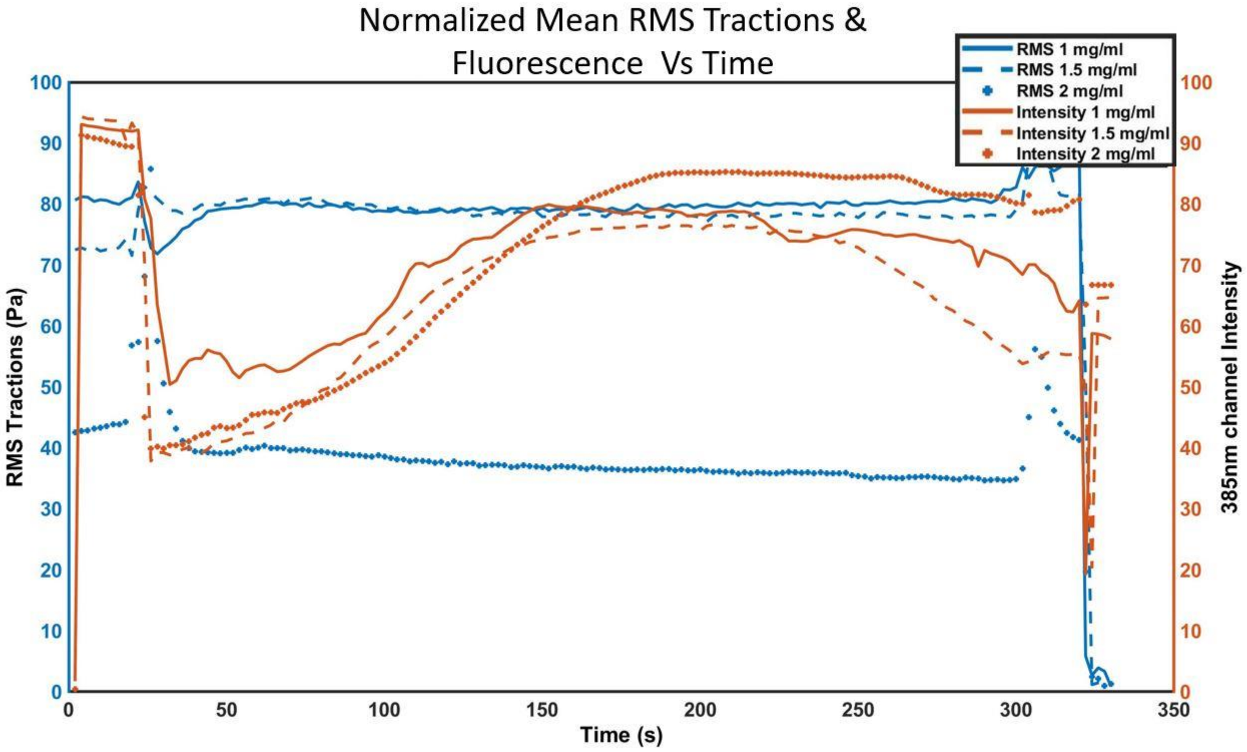

Figure 54: Overall average tractions (blue) and fluorescence intensity (orange) response for different histamine concentrations

The classification of high and low histamine concentrations utilizing average fluorescence drop (calcium level increase), cell area, and average percent of maximum traction change from 70-100 seconds (35-50 cycles when peak tractions were observed) as the predictors have been demonstrated in the machine learning classification analysis section of this chapter. The 106 observations from high and low (2 mg/ml and 1mg/ml) were shuffled and the first 76 observations were used as training sets and 30 observations were held to test the accuracies of the classifier models.

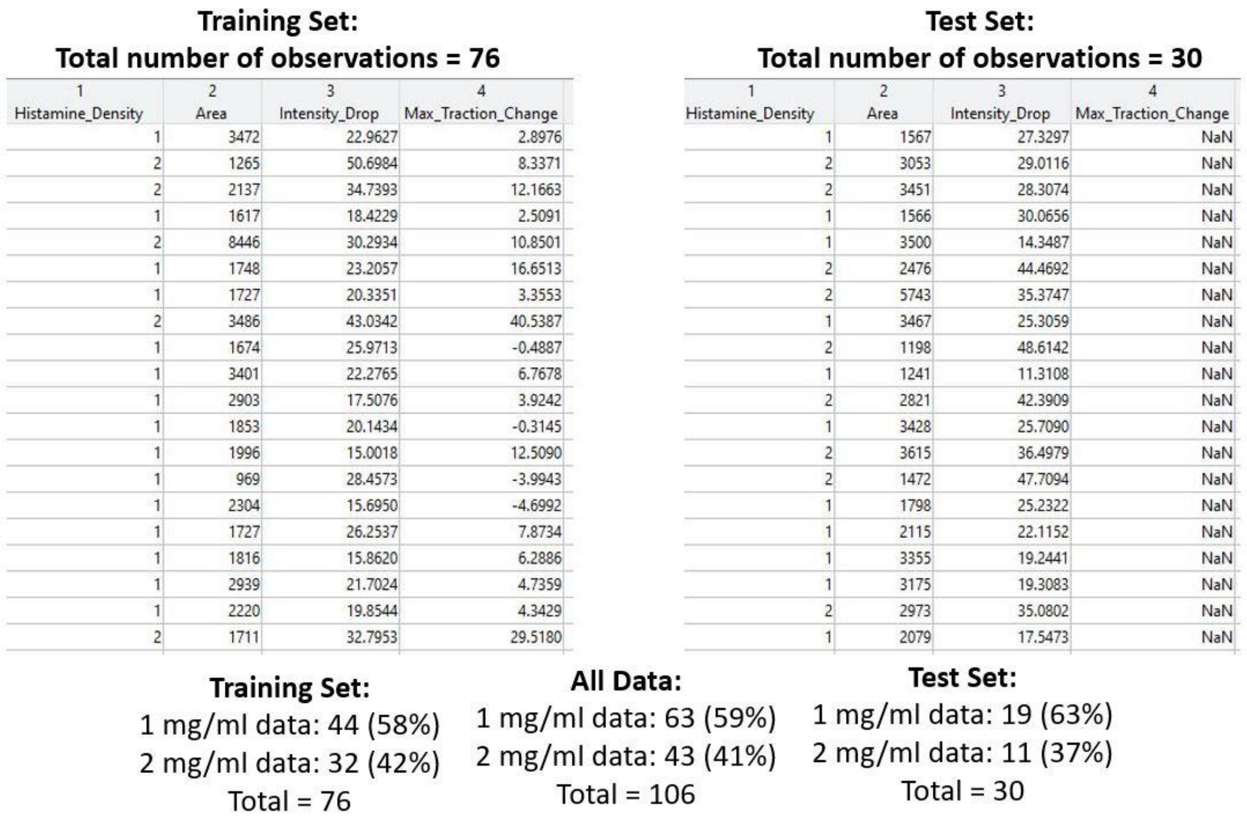

Training Set:
Total number of observations = 76

1 Histamine_Density	2 Area	3 Intensity_Drop	4 Max_Traction_Change
1	3472	22.9627	2.8976
2	1265	50.6984	8.3371
2	2137	34.7393	12.1663
1	1617	18.4229	2.5091
2	8446	30.2934	10.8501
1	1748	23.2057	16.6513
1	1727	20.3351	3.3553
2	3486	43.0342	40.5387
1	1674	25.9713	-0.4887
1	3401	22.2765	6.7678
1	2903	17.5076	3.9242
1	1853	20.1434	-0.3145
1	1996	15.0018	12.5090
1	969	28.4573	-3.9943
1	2304	15.6950	-4.6992
1	1727	26.2537	7.8734
1	1816	15.8620	6.2886
1	2939	21.7024	4.7359
1	2220	19.8544	4.3429
2	1711	32.7953	29.5180

Test Set:
Total number of observations = 30

1 Histamine_Density	2 Area	3 Intensity_Drop	4 Max_Traction_Change
1	1567	27.3297	NaN
2	3053	29.0116	NaN
2	3451	28.3074	NaN
1	1566	30.0656	NaN
1	3500	14.3487	NaN
2	2476	44.4692	NaN
2	5743	35.3747	NaN
1	3467	25.3059	NaN
2	1198	48.6142	NaN
1	1241	11.3108	NaN
2	2821	42.3909	NaN
1	3428	25.7090	NaN
2	3615	36.4979	NaN
2	1472	47.7094	NaN
1	1798	25.2322	NaN
1	2115	22.1152	NaN
1	3355	19.2441	NaN
1	3175	19.3083	NaN
2	2973	35.0802	NaN
1	2079	17.5473	NaN

Training Set:
1 mg/ml data: 44 (58%)
2 mg/ml data: 32 (42%)
Total = 76

All Data:
1 mg/ml data: 63 (59%)
2 mg/ml data: 43 (41%)
Total = 106

Test Set:
1 mg/ml data: 19 (63%)
2 mg/ml data: 11 (37%)
Total = 30

Figure 55: Training and test sets built for classification learners with the data split-ups

An example accuracy and AUROC accuracy metric were shown for Kernel Naive Bayes (KNB) in the machine learning classification analysis section of this chapter. The validation accuracy (accuracy based on training sets) for the same KNB models was shown in the following figures as an example.

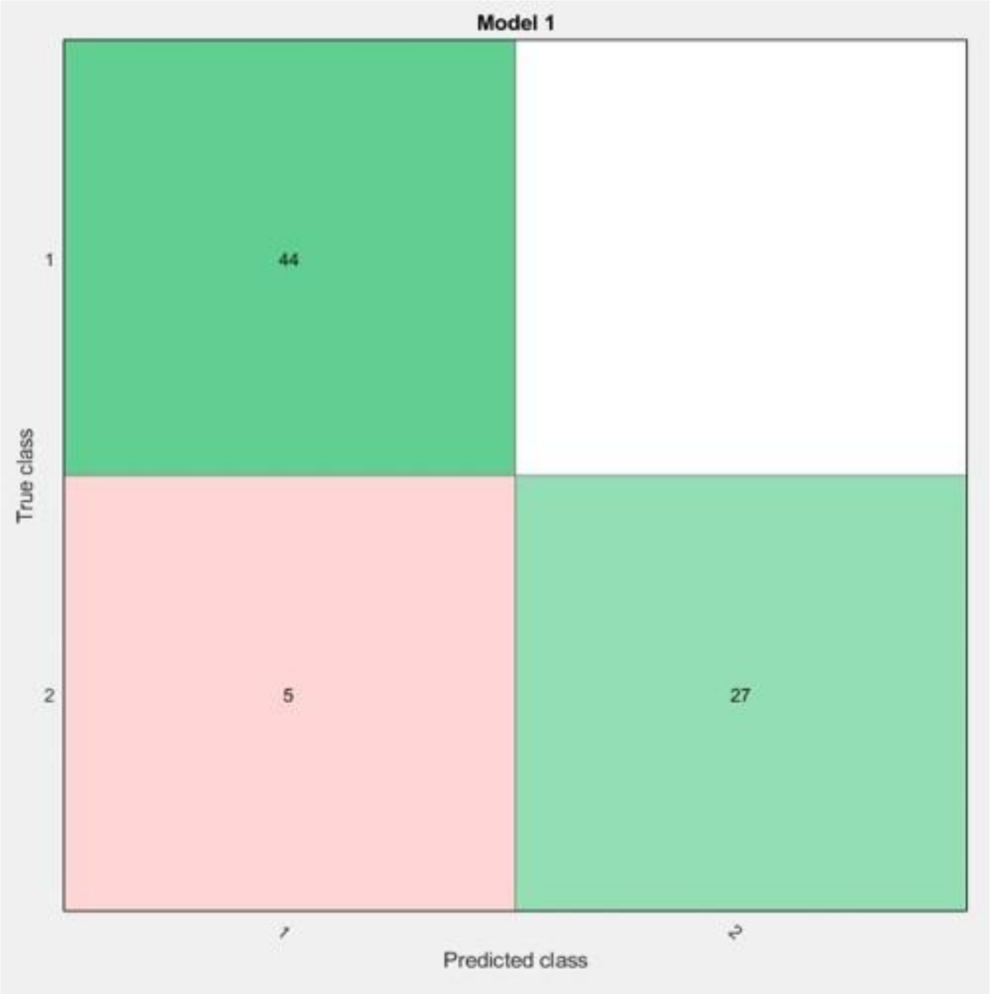

Figure 56: Confusion matrix for the data in training sets (1mg/ml and 2mg/ml histamine data) after training using KNB classification learner

In the above confusion matrix, 1mg/ml is the positive class and 2mg/ml is the negative class (classes flipped in test accuracy).

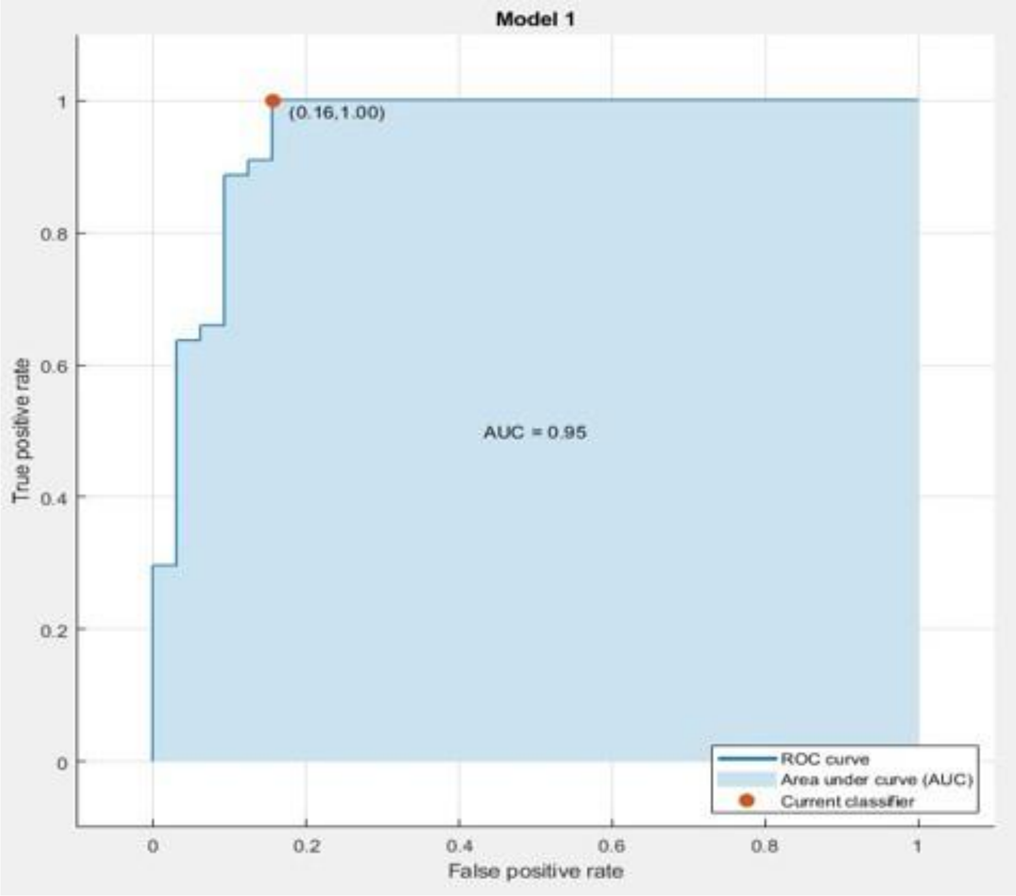

Figure 57: AUROC of KNB model for the high-low histamine training set

Figures 56 and 57 represent the confusion matrix and AUROC curve and accuracy for the training sets after training with the KNB model. This validation accuracy is different from the test accuracy shown in the classification analysis section of this chapter. The validation accuracy is based on the training sets (data divided into ‘k’ groups and k-1 groups were selected in a cycle for training the models and the average of these k-1 accuracies measured against the kth group (holdout set) is called the validation accuracy).

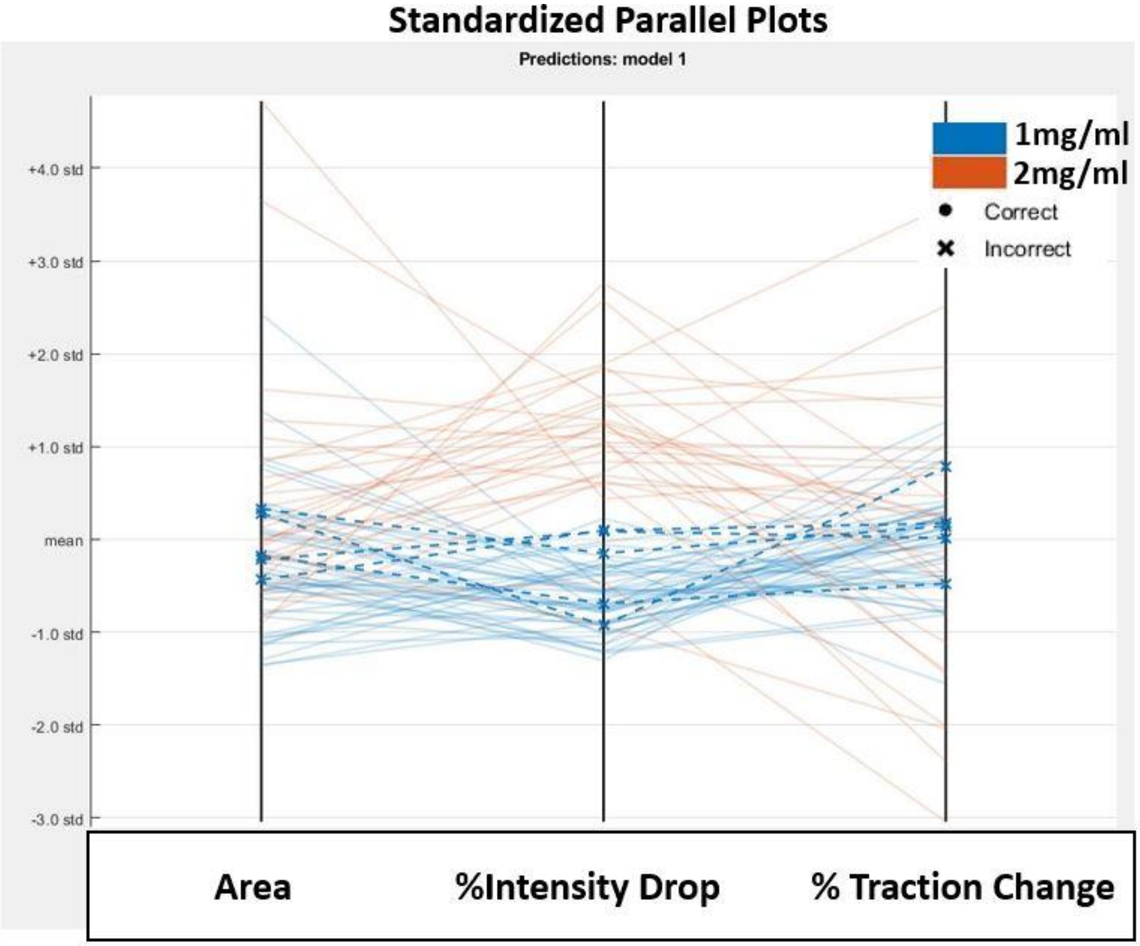

Figure 58: Standardized parallel plot of different predictors with mean as zero n set to zero and the corresponding standard deviations

The above parallel plot is just used to visualize all the predictors standardized on the same scale with the mean set to zero as the center and the variations in respective predictor groups in terms of their standard deviation. The plot is used to select the features which can be a good predictor for the response variable (histamine concentration).

Similarly, Machine Learning (ML) regression learners were also built to predict the average maximum tractions as a function of calcium increase (% fluorescence drop), histamine concentration (mg/ml), and cell area.

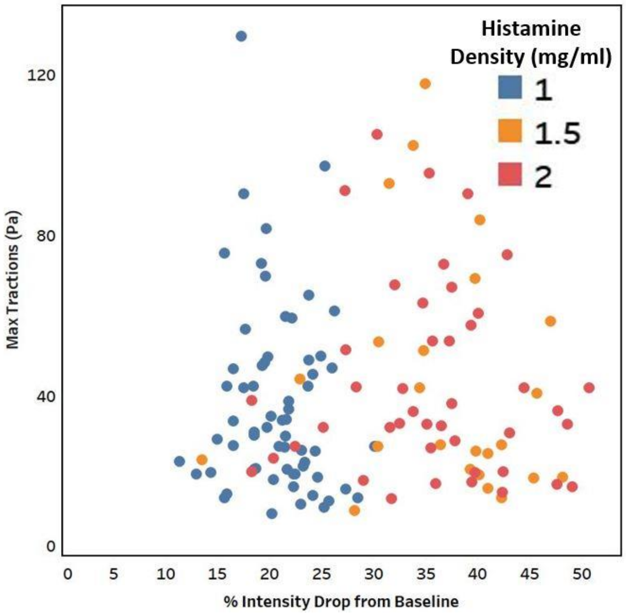

Figure 59: Average Maximum Tractions (Pa, 70-100 seconds) Vs % Fluorescence Intensity Drop for different histamine concentrations

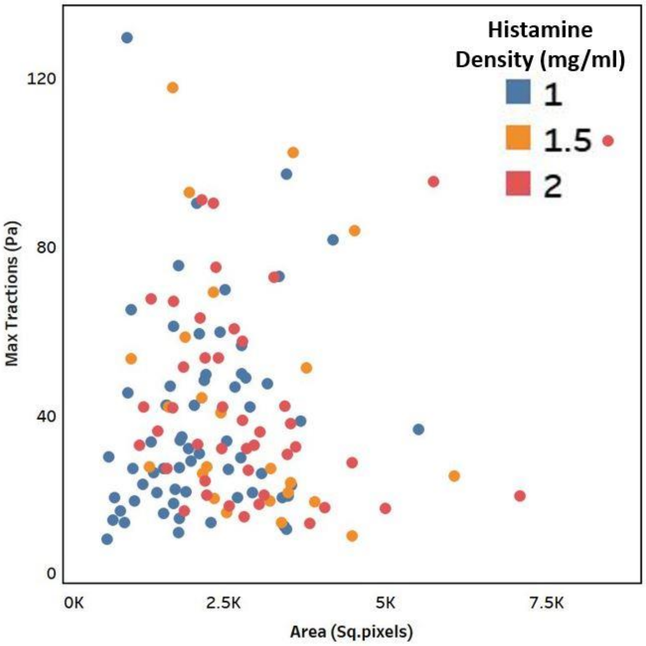

Figure 60: Average Maximum Tractions (Pa, 70-100 seconds) Vs Cell area (Sq. Pixels) for different histamine concentrations

Similar to the classification analysis, average maximum RMS tractions from 70-100 seconds (35-50 cycles when peak tractions were observed) were predicted using regression learners with cell area, histamine concentration (mg/ml), and % fluorescence drop (calcium increase) as the predictors.

For the regression analysis, 97 observations out of 130 (63 (1mg/ml), 43(2mg/ml),24(mg/ml)) observations were used to build the training sets after shuffling all the data in MATLAB. The last 30 observations were used as a holdout for testing the accuracies of the ML models. The building and training of the ML models were similar to what was described in the classification analysis. The top 4 highest observations were observed for Cubic Support Vector Machine (CSVM), Quadratic Support Vector Machine (QSVM), Linear Regression (LR), and Neural Network (NN) learners.

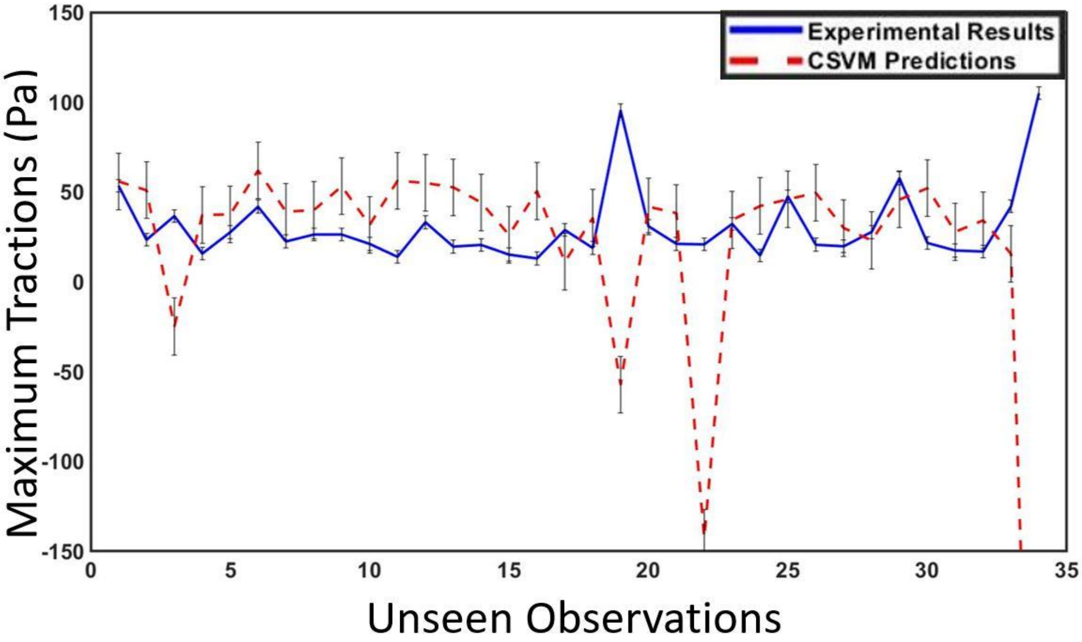

Figure 61:Experimental maximum tractions (Pa, solid blue line) Vs CSVM predictions (dotted red line) for 30 unseen observations

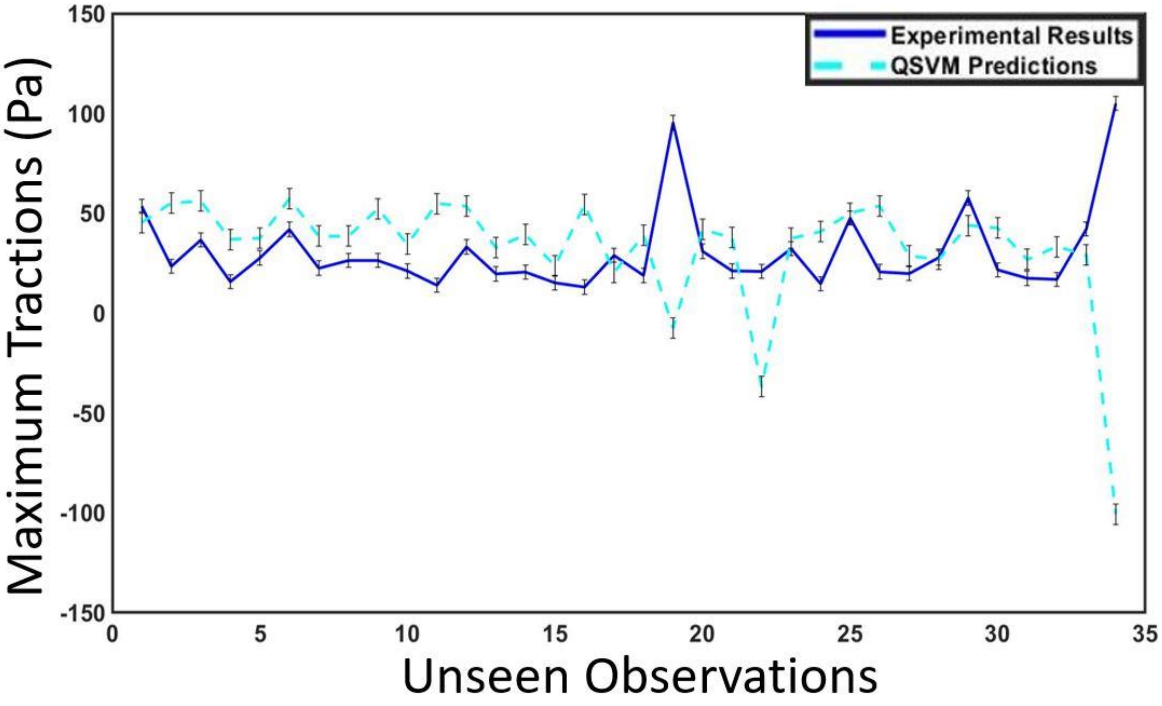

Figure 62: Experimental maximum tractions (Pa, solid blue line) Vs QSVM predictions (dotted cyan line) for 30 unseen observations

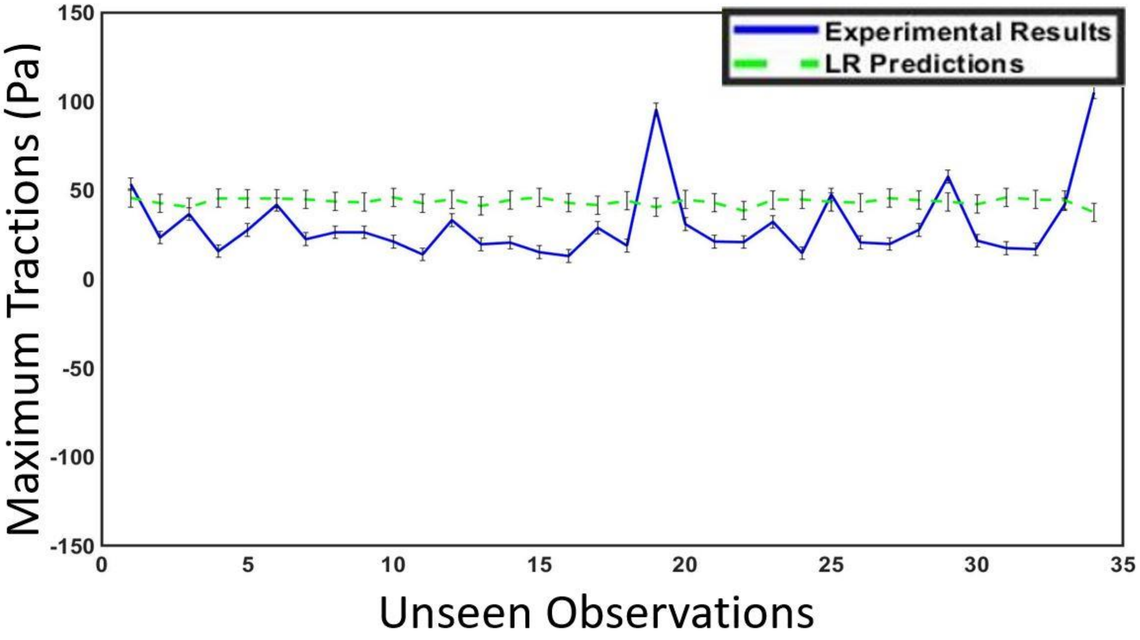

Figure 63: Experimental maximum tractions (Pa, solid blue line) Vs LR predictions (dotted green line) for 30 unseen observations

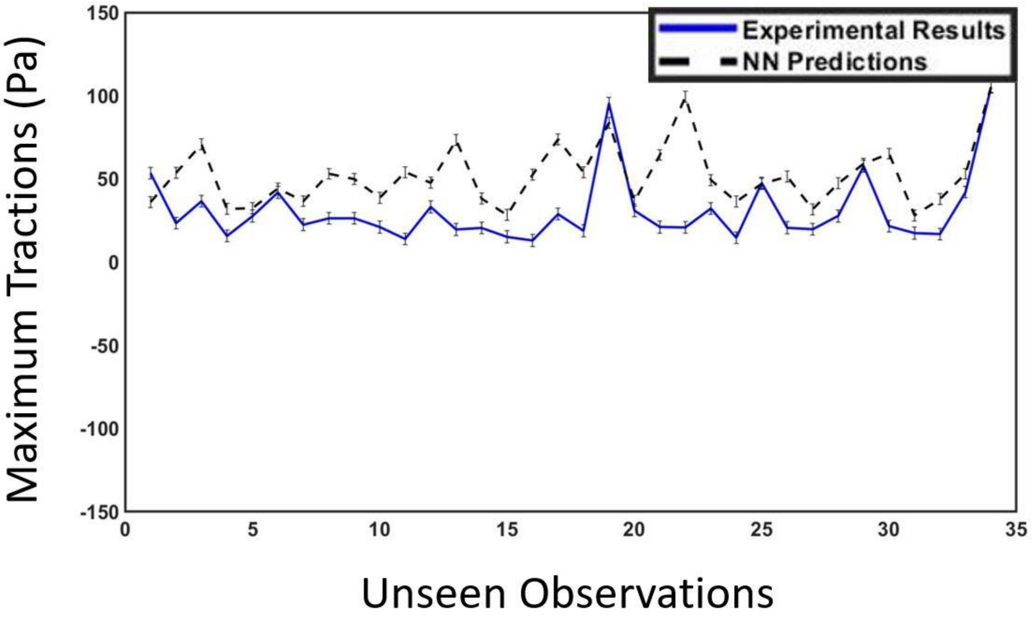

Figure 64: Experimental maximum tractions (Pa, solid blue line) Vs NN predictions (dotted black line) for 30 unseen observations

Table 2: Accuracy of regression learners for maximum traction predictions with p-value

Regression Models	Pearson R	R-Squared	P-value
CSVM	-0.651	0.424	2.9825e-05
QSVM	-0.583	0.34	0.00029318
LR	-0.458	0.21	0.0064649
NN	0.527	0.278	0.0017339

Figures 61-64 show the ML predictions of regression learners for 30 unseen observations (test data). Accuracy (R^2, coefficient of determination) was the highest for the CSVM model followed by QSVM and NN. The only positive correlation was observed for the NN predictions.

CHAPTER SIX: MACHINE LEARNING PREDICTION OF CELLULAR MECHANICAL STRESSES

Abstract

Mechanical stresses at the cell-cell level (intercellular stresses) and cell-substrate level (tractions) have been suggested to be important in a host of physiological and pathological processes such as cell migration, proliferation, wound healing, angiogenesis, and morphogenesis, for example. However, the influence various pharmacological compounds have on the processes and biomechanical stresses mentioned above is poorly understood as the cost and time required to run experiments have hindered the discovery of novel therapeutics, representing a barrier in the field. To overcome this barrier, we implemented Machine Learning (ML) to predict the dose-dependent response endothelial tractions and intercellular stresses had to 2,5-dihydroxychalcone (chalcone), a drug shown by us previously to influence endothelial biomechanics. Our machine learning modeling framework consisted of Stepwise Linear Regression (SLR) and Quadratic Support Vector Machine (QSVM) regression learners. We used the ML models along with morphological and pharmacological predictors to predict how tractions and intercellular stresses changed as a function of chalcone concentration. We utilized SLR and QSVM regression learners to predict both tractions and intercellular stresses by training our models only using data with 0.2 µg/ml & 2 µg/ml chalcone concentrations. To demonstrate the predictive capability and sensitivity of our ML models to drug concentration and morphological predictors we predict tractions and intercellular stresses in response to 0 µg/ml & 1 µg/ml chalcone (concentrations not used in training data sets) and compared our model's results to corresponding experimental results. Predictions were made using SVM and SLR models with two

different training data sets: 1) Monolayer area, monolayer perimeter, and chalcone concentration across all time and samples per datapoint (single area training set) 2) Window area, window perimeter, and chalcone concentration across all time and samples per datapoint (multiple area training set). QSVM model produced the highest R^2 of 0.81 for average normal stress predictions and 0.93 for maximum shear stress predictions utilizing multiple area training data, while the SLR model recorded the highest R^2 of 0.85 for RMS traction predictions with multiple area training data based on averages across the entire grid points and time series from 3 samples for each condition. The ML framework we present here can be used to predict the biomechanical response of any anchorage-dependent cell type to any pharmacological intervention. Therefore, we believe these results will be useful to the fields of regenerative medicine and targeted therapy using investigational drugs for cardiovascular and neurological diseases such as coronary artery disease and Parkinson’s disease.

Introduction

Cell mechanics is important in understanding biological and pathophysiological processes such as homeostasis, tissue repair, morphogenesis, angiogenesis, cancer progression, and atherosclerosis [7, 15]. Most of the cells require contractile forces to constantly probe their microenvironment composed of Extracellular Matrix (ECM). This feedback through mechanosensing can influence the mechanical properties of the cell, which is critical for cell migration, growth, differentiation, etc. [17]. The traction stresses measured on the substrate is directly correlated to the contractile forces exerted from inside of the cell [17]. The living cells also use mechanical forces to communicate with neighboring cells leading to collective pack-like behavior which is currently being investigated [18]. The junctions between cells in a monolayer enable fast, long-distance communication through intercellular stresses [18]. A series of cells in a locality could be driven by the movement of leader cells or cells close to the leader cells [22]. The traction stresses exerted by cells on the substrate can be measured using one of the most common techniques known as Traction Force Microscopy (TFM). The cell-cell normal and shear stresses recovered through Monolayer Stress Microscopy (MSM) with the help of TFM provide a visual intercellular stress map of the monolayer under study. The tractions exerted by the cells on the ECM coated substrate are communicated across the monolayer through cell-cell junctions [41]. Cell-cell and cell-ECM stresses engage in a tug of war which should balance each other according to Newton’s third law. MSM approximates the monolayer to a thin elastic plate and the intercellular stresses are solved using a chosen elastic modulus and Poisson’s ratio for the monolayer, which mimics the biological conditions and the tractions from TFM [41]. The influence of various factors such as stiffness, local tractions, monolayer geometry, local stress orientations, etc. on the collective cell mechanics was widely studied. The complex interplay among tractions, intercellular stresses, and other microenvironmental & biochemical factors is not clearly understood.

Cell-populated collagen gel was one of the first methods that measure the traction forces by estimating the change in diameter of the gel disk and traction forces were also quantified based on wrinkles exerted by the cells on the thin silicone membrane. These methods, however, suffered because of variability, lack of accuracy, and the complexity involved [36]. Micropost force sensor arrays are also being used to measure tractions of individual cells or monolayers based on deflections from the microposts [36]. A novel Förster resonance energy transfer (FRET) sensor-based approach has also been employed to measure tractions by estimating the change in excitation energy of the fluorescent protein markers that are sensitive to external forces [37]. However, FRET sensors were not able to differentiate forces in the pN range, and force contributions from other unmarked proteins could not be quantified [37]. TFM quantifies traction stresses exerted by a single or sheet of cells on a substrate that is coated with an ECM. The method computes the tractions based on the displacement field of fluorescent microbeads localized on the top surface of the substrate. A window based cross-correlation method was used to calculate the bead displacements based on comparison with a stress-free image of the bead configuration [38]. The challenges in TFM include variability in experimental data, noise in displacement data requiring low pass filters, and error due to boundary effects in a constrained TFM [17, 38]. In the MSM method, cell-cell intercellular stresses were recovered from TFM tractions by assuming a monolayer sheet of cells as elastic thin plates and imposing Newton's force balance and strain compatibility equations. The effect of boundary, external noise, out-of-plane tractions & stresses, Poisson’s ratio and elastic modulus on MSM was discussed in [41].

There are several external factors notably substrate stiffness, cell spread area, local cell curvature, and external forces that affect the cell mechanics including traction and intercellular stresses [42, 43]. [20, 42, 44, 45] investigated the interplay between cell shape, cell area, substrate stiffness, and traction forces. Research has also shown that traction force is also modulated by distance from the center of the cell to its perimeter and local cell curvature [42, 46]. [44] predicted traction stresses by using substrate stiffness (E) and cell area (A) as the predictors for a single endothelial cell (EC) and an EC pair. A positive correlation was observed for both stiffness and area with respect to the tractions. Contrastingly, [20] reported that a larger cell spread area lowered average traction forces in human pulmonary artery ECs. In addition, [42] showed that cell spread area and local curvature are better predictors of strain energy compared to the number of focal adhesions and substrate stiffness. [47] predicted traction force maps of single EC, fibroblast, and keratocyte with the first moment of area model (FMA) utilizing cell shape as the predictor. Other contour mathematical models notably the simple tension model, anisotropic tension model, tension-elasticity model, and cellular potts model provide a theoretical framework for traction forces by utilizing cell geometry [48].

More recently, Bayesian Inversion Stress Microscopy (BISM) and Kalman Inversion Stress Microscopy (KISM) were presented as predictive models for internal stress fields based on corresponding traction force data. BISM and KISM use experimental traction force data as likelihood function to make predictions using Bayesian statistics (Bayes' theorem). BISM can infer internal stress fields only from a single traction field image but a dimensionless regularization parameter must be calculated from the experimental data to make predictions. KISM however, is capable of estimating internal stress fields from a time-lapse of traction data (movie) with its accuracy depending on-time resolution of the traction data [49, 50].

The development of regenerative medicine and investigational drugs have been heavily researched to treat neurological disorders and cardiovascular diseases such as Parkinson's disease, Alzheimer's disease, hypertension, atherosclerosis, Coronary Artery Disease (CAD), etc. [9, 81, 82]. Exploring cell mechanics combined with the biochemistry of cells under the influence of the experimental drugs could shed more insights on the biomechanical and chemical signaling involved during disease propagation or cell repair. Studying the mechanism by which these experimental drugs repair or regenerate the affected tissue or cells could be helpful for improving and developing more efficient targeted drugs. Dysfunctionality in the endothelium of the vasculature due to inflammation or immunological response, for example, can cause CAD. Drugs such as Zedoarondiol and Astragaloside were developed as a potential treatment for CAD, which works by reducing inflammation on the endothelium by effectively inhibiting Reactive Oxygen Species (ROS) with enhanced antioxidant properties, are currently being investigated [10].

[35] demonstrated static endothelial monolayer response upon connexin 43 disruption in vitro, using high and low doses of 2,5-dihydroxychalcone (chalcone) drug. It has been observed that higher doses of chalcone significantly decreased Human Umbilical Vein Endothelial Cell (HUVEC) monolayer’s intercellular stresses, substrate traction stresses, cell velocities, and strain energies highlighting the contribution of Cx43 in EC mechanics. Results from [35] showed that the chalcone drug significantly impacts endothelial biomechanics. Measuring cell mechanics for different drug dosages can be challenging owing to cost and time constraints. A machine learning framework capable of predicting cell mechanics as a function of drug concentration using morphological predictors could help accelerate research and enhance our current understanding of cell biomechanics in drug therapy.

We propose a novel machine learning model to predict both tractions and intercellular stresses using pharmacological and morphological predictors. Predictive models were created using Stepwise Linear Regression (SLR) and Quadratic Support Vector Machine (QSVM) regression learners. The SLR and QSVM models were trained using two different training sets: 1) Single Area Training (SAT) set utilizing monolayer area, monolayer perimeter, and chalcone concentration as predictors 2) Multiple Area Training (MAT) set utilizing overlapping window area, window perimeter, and chalcone concentration as predictors. The predictive capability of the model is demonstrated by comparing the experimental results for different chalcone dosages to the corresponding tractions and intercellular stresses predicted by the SLR and QSVM models trained using the SAT and MAT datasets.

Materials and Methods

Substrate Displacement Computation

The 2-D displacement of fluorescent beads on the top surface of the gel was computed using a window-based Particle Image Velocimetry (PIV) routine. The entire image was divided into a set number of overlapping windows depending on the crop size of the image used for the PIV analysis. Cross-correlation between each window in the reference image was computed against a window occupying the same coordinates in the fluorescent image (with cells attached) sequentially, across all the window blocks. The displacements were calculated in the x and y coordinate system in pixels using an iterative cross-correlation function. The displacement calculated from the peak cross-correlation function between each reference-fluorescence window pair was assigned to the center coordinates of those windows [36].

Traction Force Microscopy (TFM) & Monolayer Stress Microscopy (MSM)

Traction force Microscopy and monolayer stress microscopy as previously described in [22, 38, 56, 57] was used to calculate the traction maps on the PA gel substrate and intercellular stresses respectively. Briefly, the deformations on the top surface of the gel were calculated by running a window-based Particle Image Velocimetry (PIV) routine that computes the pixel shift in fluorescent images of the gel (cells attached) with respect to the stress-free reference image (fluorescent image taken after trypsinization). Intercellular stresses were calculated as previously described in [56, 57]. The intercellular stresses were recovered from traction force maps on the substrate by using straightforward force balance equations imposed by Newton's law. The computed local two-dimensional stress tensor within the monolayer was converted into maximum principal stress (σ_{max}) and minimum principal stress (σ_{min}) along the principal plane by rotating the local coordinate system along with the principal orientation. The average normal stress $(\sigma_{max} + \sigma_{min})/2$ and maximum shear stress $(\sigma_{max} - \sigma_{min})/2$ were calculated at each point in the elements within the monolayer as discretized by the Finite Element (FEM) code.

Predictions using Machine Learning (ML) Models

The tractions on the substrate and intercellular stresses calculated from TFM and MSM respectively can be used as the response or dependent variables for building the ML Models. Briefly, a set of predictors (independent) were identified that can be linked to the dependent variables. A training table was generated associating the predictors to the outputs that were to be predicted. The generated training table was fed into the ML regression learner which trains the data establishing relationships between the input (predictors) and output (response) features. Type of ML regression model and the algorithm it uses, values set for the tuning parameters, amount of data in the training table, and type of predictors used can greatly influence the relationships correlated between the input and output variables which in turn affects the prediction accuracy and Root Mean Square Error (RMSE). After training the different ML models based on data in the training table, predictions were made for new test data held within the training tables using 5-fold cross-validation. Based on the value of R^2 (capability of ML model to explain the variability in data) and RMSE for the test data, the ML models were chosen. ML models with high R^2 and low RMSE values were preferred for making predictions with the new data. The ML models can be trained by feeding the training table into the 'Regression Learner' application in MATLAB 2019a. The trained model can be stored as a '. mat' structure variable for each chosen ML model. Later, for a new phase image for which the predictions are to be made, the predictors (input features) were extracted for those images grouped together as a table in the same format as that of the training table. Now, from this new prediction table (containing only the predictors from the new phase image) and the trained ML model (stored as a structure variable containing relationships between predictors and response variable computed from training data), a fit of response variables like RMS tractions or maximum/minimum intercellular stresses can be computed.

Selection of Predictors and Response Variables

Predictors selected for building the ML model can dictate the robustness and accuracy of the model. RMS Traction, Maximum Principal Stress, and Minimum Principal Stress were the three response variables chosen for constructing the training table. These three response variables were the results gathered from TFM and MSM respectively. The selection of predictors was done prudently involving only those factors that were known to affect the response variables. A list of predictors that were considered includes monolayer area, monolayer perimeter, monolayer density, cell shape, cell curvature, substrate stiffness, substrate porosity, cell velocity, substrate traction, shear flow rate, and concentration of drug [27]. However, for the sake of simplicity and to demonstrate the predictive capability of ML models mainly as a function of drug dosage only monolayer area & perimeter, window area & perimeter, and drug concentration were chosen as the predictors. Also, the chosen predictors must be dynamic otherwise the ML predictions will be insensitive to any changes in the predictors for the new data (phase image).

Data Selection

The data for building the training tables were obtained from [35]. The results computed from four HUVEC monolayer data were used to build the ML models. Each chosen monolayer sample had a sequence of 73 images taken 5 min apart since the start of the experiment (about 6 hours). All the images in the selected monolayers had the same crop size (2000×2000 pixels), window size (32 pixels), and overlap (0.75) (for displacement calculation using PIV routine), and hence the size of traction/intercellular stress data was also same for all the images from the four monolayer samples. The results gathered from MSM were in the form of a square matrix with displacement and corresponding traction data at the center of each overlapping grid on the image. The size of traction data (spatial resolution) depends on the overlap, crop size, and window size used in the PIV routine. The intercellular stresses were also a square matrix computed from tractions using a FEM code that solves for the boundary conditions applied along the contour of the monolayer (free edge) where the stresses are zero: $\sigma_{ij}n_j = 0$ and n_j is the unit normal vector to the monolayer boundary. The square matrices of traction and intercellular stress data were converted and stored as their respective column matrices. For the crop size, window size, and overlap used in the analysis there exists 246×246 traction/intercellular data which is equivalent to 60516 data points (after conversion into a column matrix). Out of the four chosen monolayer samples, two of the samples were subjected to 0.2 µg/ml chalcone treatment and the two other samples were subjected to 2 µg/ml of chalcone.

Building Training Tables from TFM & MSM Data

The three response variables chosen for the training data were RMS traction, Maximum principal stress, and Minimum principal stress respectively. Training tables were created separately for each of these response variables with the help of predictors before training them with ML models. The predictors chosen for building the training tables were monolayer area & perimeter, window area & perimeter, and chalcone concentration. The type of predictors and the combinations of predictors chosen can affect the ML model's accuracy, robustness, sensitivity, and prediction (computational) time. The predictors computed from the phase images will be linked to these response variables. Two different training sets were used depending on the combination of predictors used for training the ML models.

Single Area Training Set

This training set, as the name suggests uses monolayer area & perimeter and chalcone concentration as the predictors to link the response variables for the training data. The monolayer contour of each of the four samples was traced after converting the images into binary. The monolayer area & perimeter were then calculated using the 'regionprops' command in MATLAB. The monolayer area & perimeter remain the same for all the images in a monolayer sample (constrained monolayer) but differ among other monolayer samples. The predictors were calculated for each image separately with the size 1×60516, the same as that of the response variables (tractions/intercellular stresses). For the monolayer area & perimeter, the same value was copied to all the images in a monolayer sample matching the size of the response variables (column vector with 60516 data points with the same area/perimeter values for each image in the monolayer of interest). Similarly, the same chalcone concentration was copied to all the images depending on the monolayer concerned. However, grouping the data across all the four different monolayer samples will result in four different monolayer area/perimeter (different for each monolayer but same values for all the images pertaining to that monolayer sample with size same as response variable) values and two different chalcone concentrations (0.2 & 2 μg/ml). Training tables were created by grouping predictor and response variable data from all the images (292 images in total; 73 images per monolayer sample) for each corresponding overlapping window separately. Hence, 60516 training tables were generated in total for each response variable (RMS Traction, Maximum and Minimum Principal Stresses) forming the single area training set. Since the same monolayer area/perimeter values were used for all the images in a monolayer sample, this training set can only train ML models to predict the average values of RMS Traction, Maximum and Minimum Principal Stress based on 6-hour phase image data from 4 monolayer samples. The single area method can't capture HUVEC's movement within the monolayer and can only make average predictions for a given input image based on the monolayer contour or drug concentration. A time series for new images can't be generated using the single area training set if the monolayer was constrained. However, a time series can be generated for an expanding monolayer.

Multiple Area Training Set

Multiple area training is like a single area method but here instead of computing area & perimeter for the entire monolayer, area/perimeter was calculated for each overlapping window block that collectively makes up the entire field of view of the phase image. The individual HUVECs in the monolayer can be traced and their area/perimeter can be computed as well but the number of HUVECs will be different for different images and the size of the cell area and perimeter data will also vary depending on the confluency of the monolayer. Hence, it will be difficult to use an individual cell's area, perimeter, or any other cell feature as a predictor because of a mismatch between the size of the response variables and cell area/perimeter. To tackle this issue, instead of calculating the area of cells individually, the phase image was divided into the same number of overlapping windows used in the displacement/traction calculation. The area & perimeter values were calculated for each of these windows which were then stored as a column matrix for each image in the monolayer samples. In the case of the window method, calculated area & perimeter match the size of response variables because of the use of overlapping windows/blocks that have the same size and overlap settings used for displacement/traction calculations. Training tables were created with the calculated window area & perimeter values and linked with one of the response variables. The predictors and response variables stored separately were gathered along with the chalcone concentration using MATLAB codes as described in the previous section. Although the same number of phase images and training tables were used to create the ML models, this method can generate time series of cell mechanics of interest (RMS Traction/intercellular stresses). This is possible because, unlike the monolayer area which remains constant for all the images in time series (constrained monolayer experiments), the window area changes as the cell moves within the monolayer. The change in area/perimeter in each box will result in a different output prediction based on the data that was used to train the ML model.

Selection of ML Models

The generated training tables were fed into the ML models available in MATLAB 2019 Regression Learner App. Each training table, in the case of single and multiple area methods, has 292 data points (number of data in each predictor or response variable). Since the data was relatively small, it was trained with all the available ML models. Each model after training returns the Root Mean Square Error (RMSE) and coefficient of determination (R_2) of its predictions. Five-fold cross-validation (usually 5 or 10 is recommended but 5 was chosen because of relatively small table size 292×4 for each training table) was used to validate the models where the inputted training table was randomly divided into five groups and one group was held as the test data on which the model makes prediction after training the data from the remaining four sets. The models with high R^2 and low RMSE values were usually chosen to make predictions for all the new data. In our case, not all ML models were sensitive to the changes in predictor values extracted from a new phase image while making predictions. In all the previous methods, chalcone concentration was used as one of the predictors. A chalcone concentration value of 0.2µg/ml was used for 146 images representative of two monolayer samples and a concentration of 2µg/ml was used for the remaining 146 images from the other two monolayer samples as per the MSM experimental data and results. Since all the images have one of the two concentration values most of the ML models weren't sensitive to changes in the drug concentration that was inputted into the model when making predictions for the new data. Although robustness in an ML model is desired ideally, in our case, we would want the model to be sensitive to the changes in drug concentration without drastically overfitting the predicted results. Also, since other predictors like monolayer area/perimeter and window area/perimeter were used along with the drug concentrations, only the ML models which were sensitive to changes in all the predictors were chosen. After training the models on several of the training tables or sample data sets, test predictions were made for new data with different predictors. Support Vector Machine (SVM), and Stepwise Linear Regression (SLR) based models emerged as frontrunners for our MSM data. Trained models based on SVM and SLR were sensitive to new data with less overfit and high R^2 values compared to the other models. These models once trained were stored as a '. mat' structure variable which can be later called to make the predictions for the new phase image. A trained model database was created by writing a MATLAB function which inputs the training tables sequentially in a for loop, trains the tables for a chosen ML model, and stores the trained ML model in a folder which can be called later to make predictions for the new data (phase image). ML model database was created separately for each chosen ML model, response variable, and data training method. Each database contains a trained ML model variable for all the 60,516 response variable data. The number of response variable data depends on the crop size, overlap, and window size chosen in the PIV routine to get the displacement data based on which traction and intercellular stresses were calculated from TFM and MSM respectively. The training time for single and multiple area methods was around 5 hours for 292 images. For the average table method, the training time was 10-20 minutes for the SLR model and ~ 8 hours for SVM models.

Support Vector Machine

Support Vector Machine (SVM) is widely used in classification and regression analysis. SVM utilizes the kernelization technique to effectively find the hyperplane that separates the support vectors by transforming the data in higher dimensions in classification problems. In regression, the hyperplane is the best fit line or curve that effectively fits most of the points or support vectors. SVM can use different kernels like linear, quadratic, or gaussian to compute the transformation in higher dimensions at a reduced computational cost, where it is easier to find the hyperplane that is closer to most of the data points. SVM optimizes the hyperplane so that the distance from each support vector is minimized within the chosen decision boundary. The decision boundary encompasses the data that are closer to the hyperplane. A margin of tolerance (ε) can be inputted by the user to increase the tolerance level from the decision boundary. SVM can easily tackle complex, non-linear data, robust to outliers and has better prediction accuracy compared to linear regression models. However, SVM is susceptible to noise and not preferred for very large or very small data sets [83].

Stepwise Linear Regression

Stepwise Linear Regression (SLR) evaluates the independent or exploratory variables one by one through a forward selection rule (variables added at each step), backward-elimination rule (all variables included), or a bi-directional rule (combination of both forward selection and backward elimination) by computing the t statistics for the coefficients of the selected variable at each step. The SLR regression model helps choose the best independent variables efficiently based on statistical significance. Although very effective in minimizing the number of predictors, the SLR model is prone to choosing wrong variables if there is a large number of predictors and a small amount of data [84].

Making Predictions from Trained Models

To make predictions for a new phase image, only the predictors used in the training sets on which the ML model was trained were extracted. The extracted predictors were grouped together in a table (prediction table) like tables in the training set, but the last column representative of a response variable should be left empty. Now, the prediction table was inputted to the trained ML model in MATLAB 2019a using the command:

```
R = TM.predictFcn(T)
```

where ‘R’ is a column vector with a fit of the predicted response variable

‘TM’ is a ‘. mat’ variable of the trained ML model and ‘T’ is the prediction table.

Predictions were made from each trained model variable in the database for the given prediction table. These results were coupled together to get the overall predictions for the new phase image in the case of single and multiple area training sets. The prediction table was a single row of data with monolayer area, perimeter, drug concentration, and an empty response variable. In the case of multiple area training sets, prediction tables were generated for each image because of changing window area as HUVECs move with time which makes time-series predictions possible. Prediction time for a single new phase image was around 20 minutes and 5 minutes for single area training, multiple area training respectively.

Validation of Predicted Results Against MSM

Predictions made for each response variable were computed for a new image with different monolayer areas and drug concentrations. The models were built on data from 4 monolayer samples with just two chalcone concentrations (0.2 & 2µg/ml). Predictions were made for new phase images with chalcone concentrations set to 0 & 1µg/ml respectively. Master average of the predicted results (RMS Traction, Average Normal Stress, Maximum Shear Stress) was compared with the actual master average of the results computed from TFM & MSM. Master average of the results is the average of the response variable in all the overlapping blocks that make up the image and the average is taken across the entire image time series that follows in the MSM experiment. Predictions were made for 3 monolayer samples for each of the four chalcone concentrations, using the proposed ML models based on two different training sets and compared against the actual experimental result averages from 3 samples for each chalcone concentration obtained from MSM. Pearson coefficient (R) was used as the metric to validate how close the predicted average results match with the actual MSM trend. Predictions were also made for all the four chalcone concentrations and the averages of the predicted results were compared to MSM results pertaining to that chalcone concentration and R values were calculated. Correlation was calculated in Excel 2016, using the formula: Correlation = Covariance (A, B) / (Std. Dev A * Std. Dev. B). If the trend between MSM and predicted results were close, then we get high R values and vice versa. R^2 (coefficient of determination) is a much-preferred metric in statistics that represents the % of the variability in data that can be explained by the ML model. Root Mean Square Error (RMSE) was also computed for the predicted averages of the response variable against the experimental MSM data based on averages from 3 samples, across 60,516 grid points in each of the 292 images in the time series for each chalcone concentration.

Results

Single Area Training Set

The ML models were trained using data from 4 samples with 2 different chalcone concentrations (0.2 & 2 µg/ml). The cellular stress predictions were made using SLR and QSVM models for three new unseen samples for each of the four chalcone concentrations: 0 µg/ml, 0.2 µg/ml, 1 µg/ml, and 2 µg/ml and compared against the experimental averages of three samples for each chalcone concentration (see figures 65-70, tables 3-5). The overall coefficient of determination (R^2) for the average normal stress predicted by SLR and QSVM models for different chalcone concentrations were 0.74 & 0.7 respectively. R^2 for maximum shear stress predicted by SLR and QSVM were 0.88 & 0.84 respectively. Relatively lower R^2 of 0.51 & 0.54 were seen for RMS tractions predicted by SLR and QSVM models for different chalcone concentrations. RMSE for the predictions from SLR and QSVM models was 24.18Pa and 27.5Pa respectively for average normal stress, 47.26Pa and

53.57Pa respectively for maximum shear stress, and 6.5Pa and 5Pa respectively for RMS traction predictions. Overall, the prediction accuracy was the highest utilizing the SLR model, for average normal and maximum shear intercellular stresses (R^2 of 0.74 and 0.88). The prediction accuracy of RMS tractions was the highest for the QSVM model with R^2 of 0.54 (from table 3, single area training column). The predicted intercellular stress distributions for different chalcone concentrations were shown in figures 66 and 67. RMS traction distributions in figures 69 and 70.

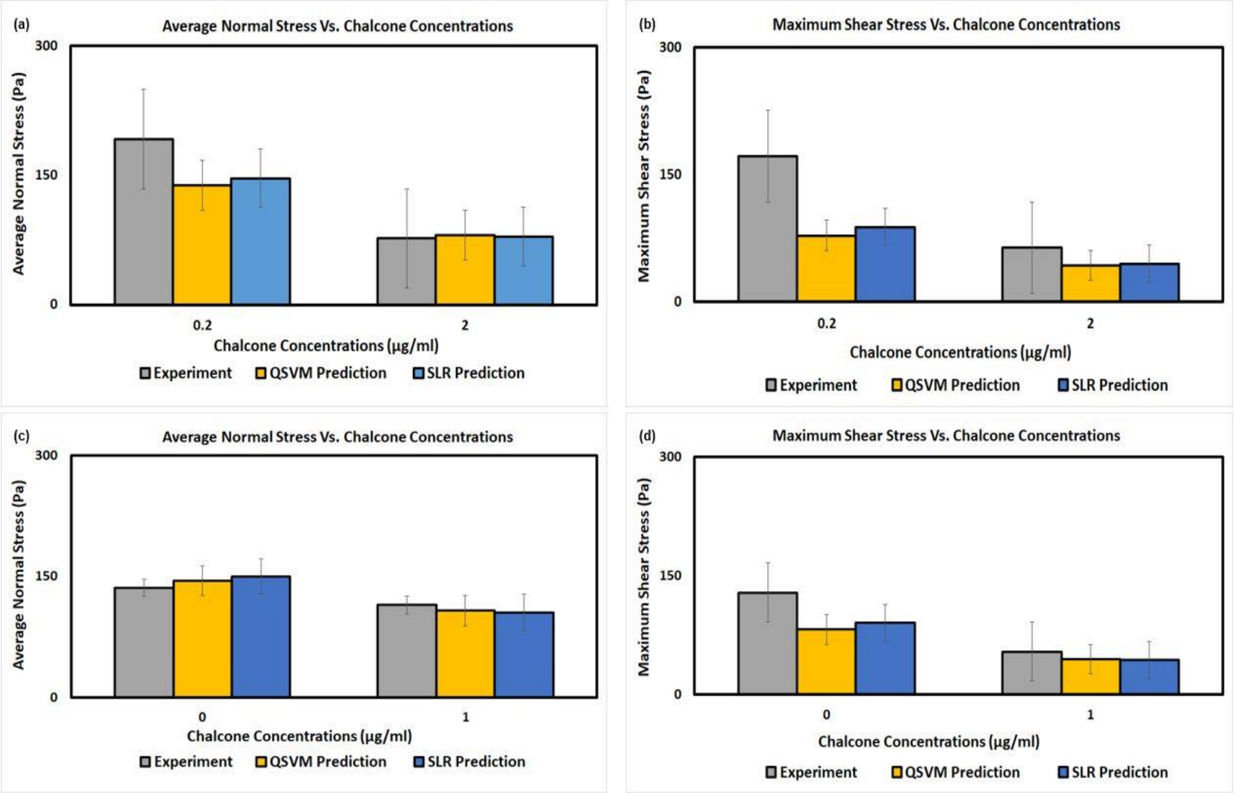

Figure 65: Average normal stress and maximum shear stress experimental results, QSVM, and SLR predictions utilizing single area training set for 0.2 µg/ml and 2 µg/ml (a and b) and 0 µg/ml and 1 µg/ml (c and d) chalcone concentrations

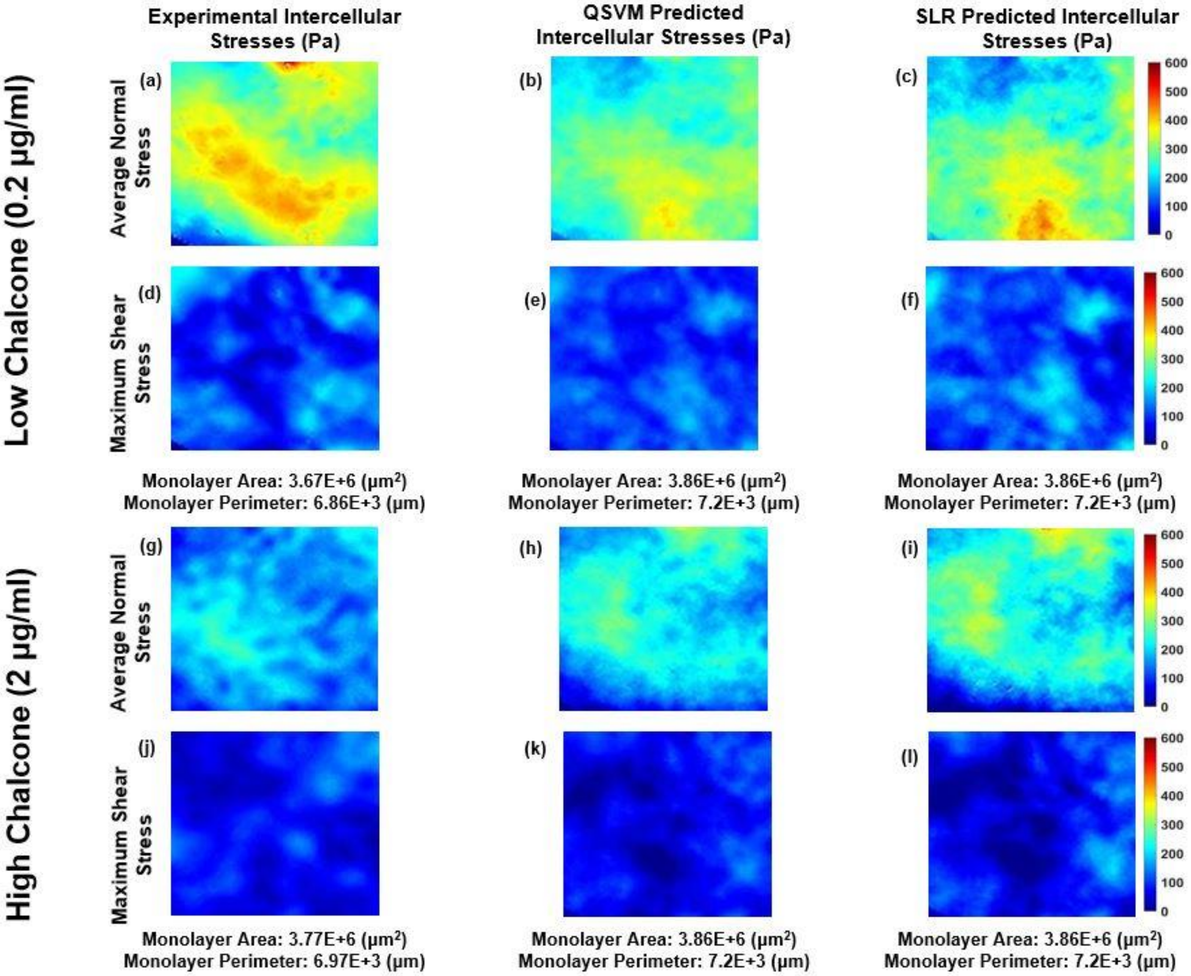

Figure 66: Experimental average normal stress, QSVM, and SLR predicted average normal stress distributions for 0.2 µg/ml chalcone concentration (a-c). Experimental maximum shear stress, QSVM, and SLR predicted maximum shear stress distributions for 0.2 µg/ml chalcone concentration (d-f). Experimental average normal stress, QSVM, and SLR predicted average normal stress distributions for 2 µg/ml chalcone concentration (g-i). Experimental maximum shear stress, QSVM, and SLR predicted maximum shear stress distributions for 2 µg/ml chalcone concentration (j-l). All QSVM and SLR predictions made using single area training sets

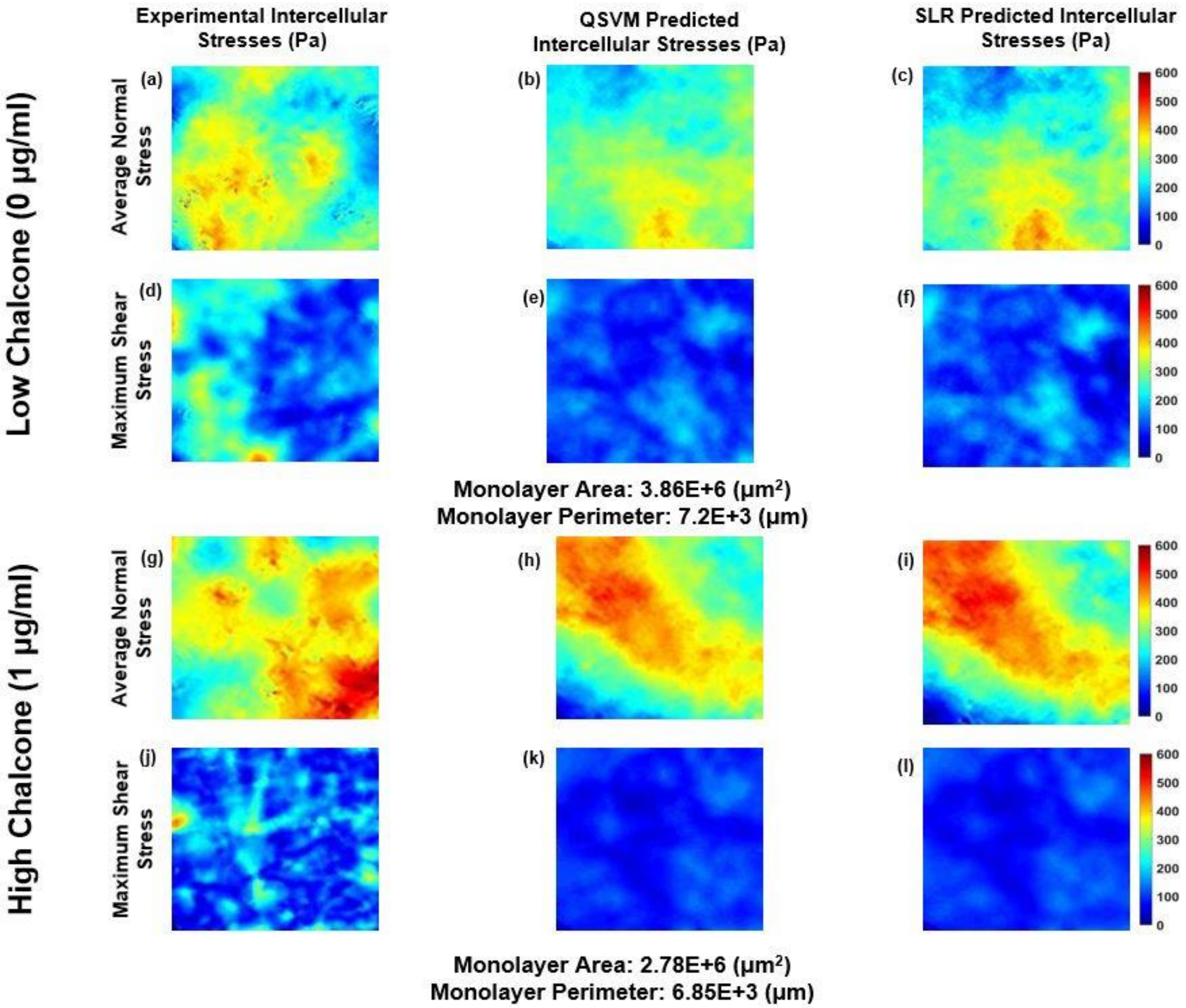

Figure 67: Experimental average normal stress, QSVM, and SLR predicted average normal stress distributions for 0 µg/ml chalcone concentration (a-c). Experimental maximum shear stress, QSVM, and SLR predicted maximum shear stress distributions for 0 µg/ml chalcone concentration (d-f). Experimental average normal stress, QSVM, and SLR predicted average normal stress distributions for 1 µg/ml chalcone concentration (g-i). Experimental maximum shear stress, QSVM, and SLR predicted maximum shear stress distributions for 1 µg/ml chalcone concentration (j-l). All QSVM and SLR predictions made using single area training sets

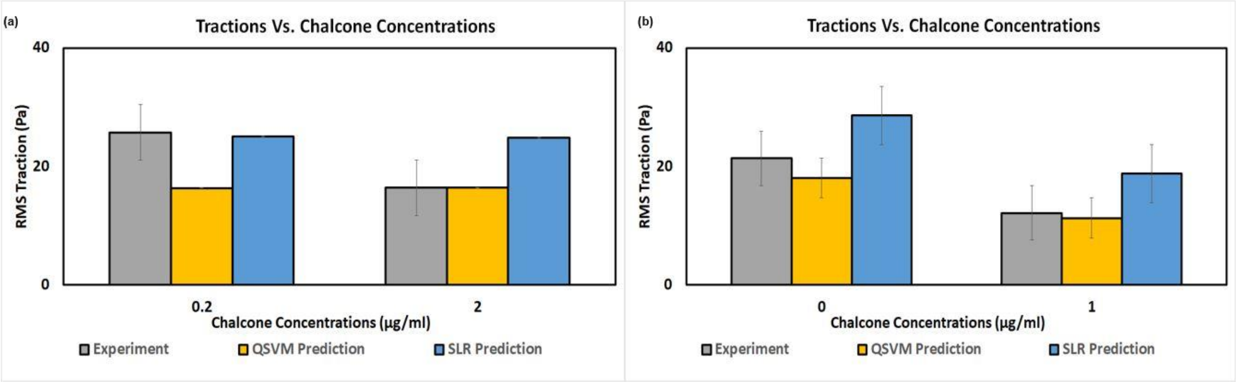

Figure 68: RMS traction experimental results, QSVM, and SLR predictions utilizing single area training set for 0.2 µg/ml and 2 µg/ml (a) and 0 µg/ml and 1 µg/ml (b) chalcone concentrations

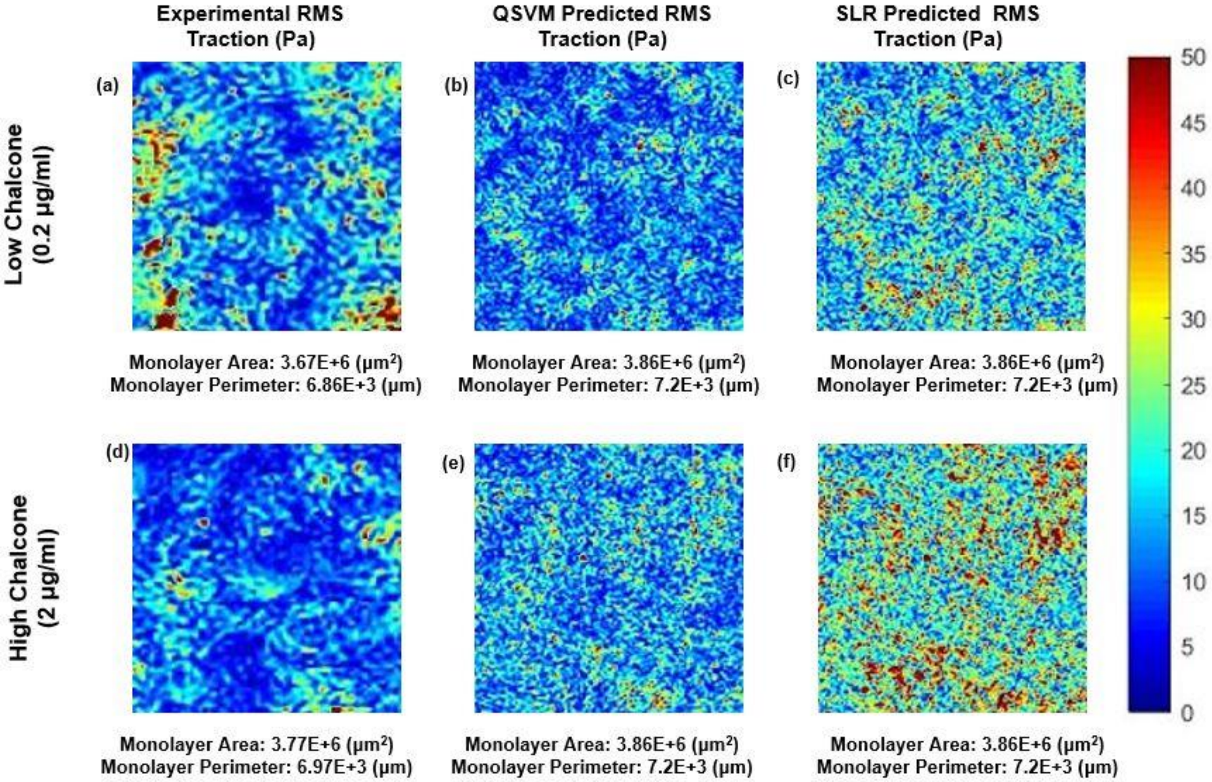

Figure 69: Experimental RMS traction, QSVM, and SLR predicted RMS traction distributions for 0.2 µg/ml chalcone concentration (a-c) and 2 µg/ml chalcone concentration (d-f) utilizing single area training set

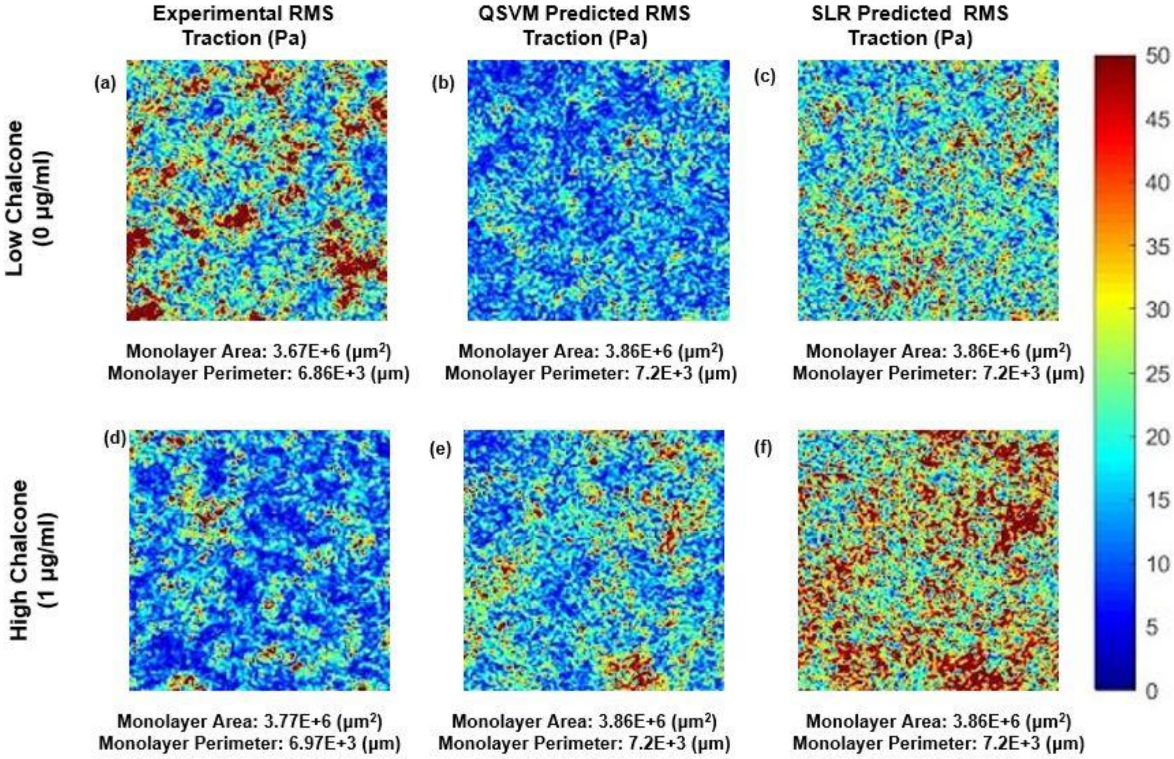

Figure 70: Experimental RMS traction, QSVM, and SLR predicted RMS traction distributions for 0 µg/ml chalcone concentration (a-c) and 1 µg/ml chalcone concentration (d-f) utilizing single area training set

Multiple Area Training Set

Similar to results from the previous section, predictions were made using SLR and QSVM models for three new samples for each of the four chalcone concentrations using multiple area training sets and compared against the corresponding experimental results (see figures 71-76, tables 3-5). The R^2 values for average normal stress predicted by SLR and QSVM were 0.67 and 0.81 respectively with RMSE of 24.49 Pa and 22.20Pa respectively. Higher R^2 values of 0.87 and 0.93 were seen for maximum shear stress predicted by SLR and QSVM models with RMSE of 49.06Pa and 52.67Pa. For RMS tractions, the R^2 values were 0.85 and 0.008 for SLR and QSVM models with RMSE of 4.56Pa and 7.37Pa respectively. Overall, the prediction accuracy was the highest utilizing the QSVM model, for average normal and maximum shear intercellular stresses (R^2 of 0.81 and 0.93). The prediction accuracy of RMS tractions was the highest for the SLR model with R^2 of 0.85 (from table 1, multiple area training column). The predicted intercellular stress distributions for different chalcone concentrations were shown in figures 72 and 73 and RMS traction distributions in figures 75 and 76.

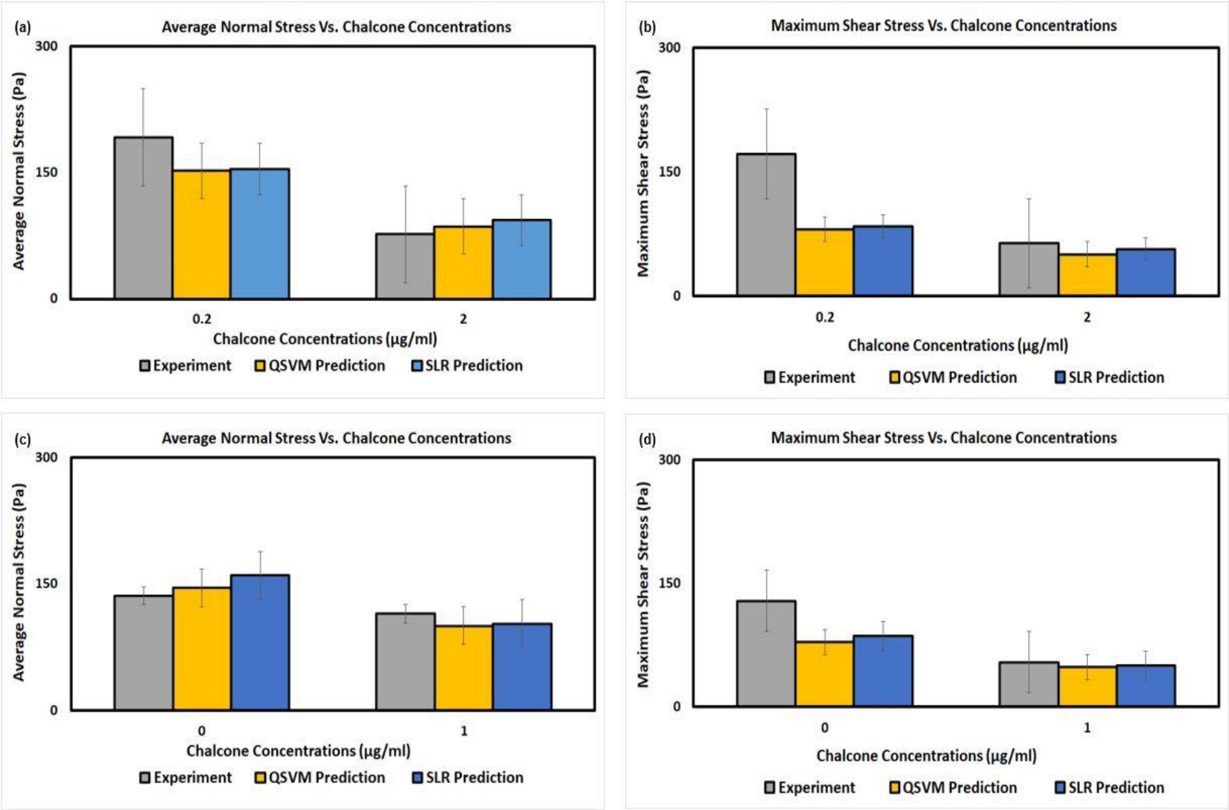

Figure 71: Average normal stress and maximum shear stress experimental results, QSVM, and SLR predictions utilizing multiple area training set for 0.2 µg/ml and 2 µg/ml (a and b) and 0 µg/ml and 1 µg/ml (c and d) chalcone concentrations

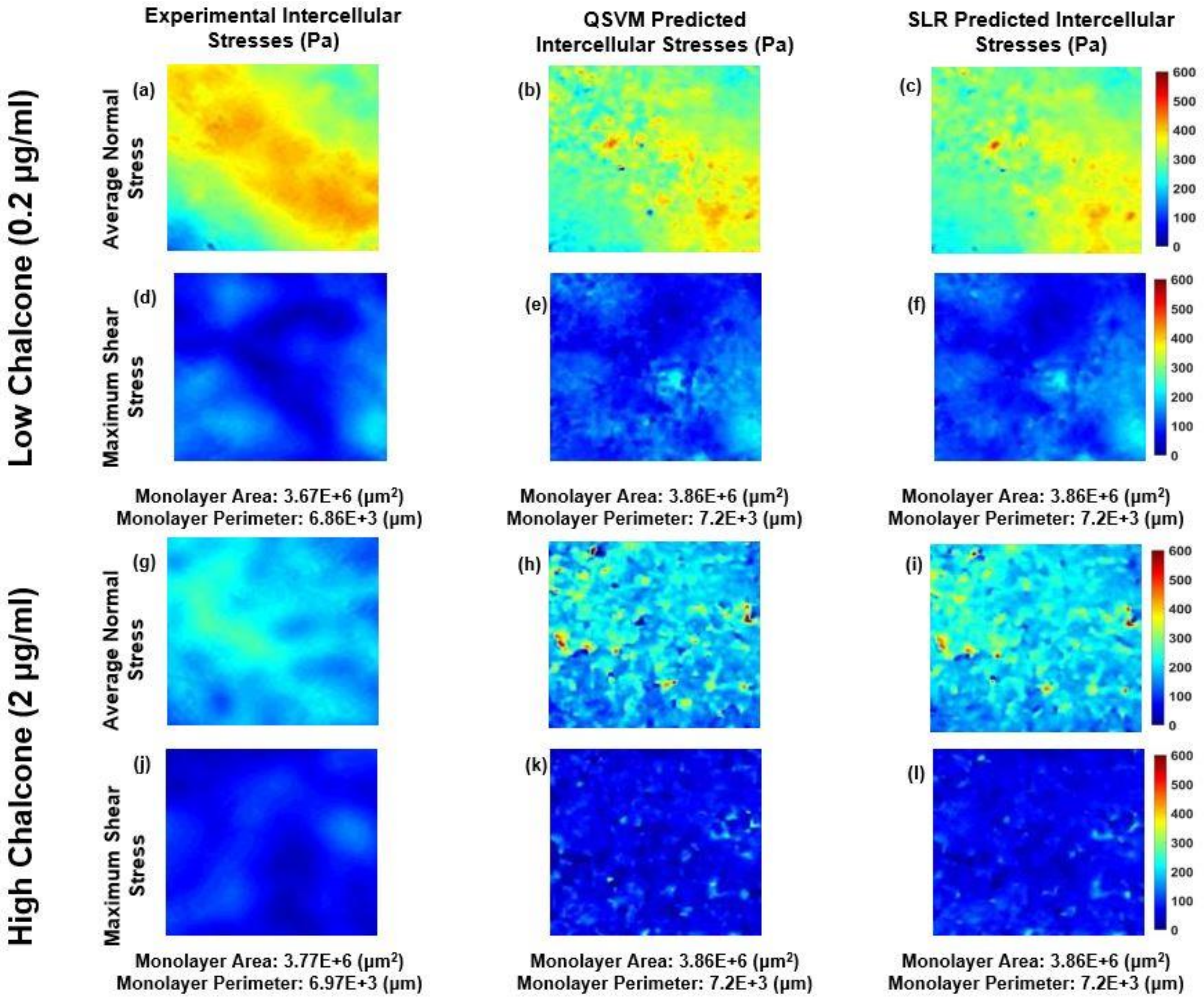

Figure 72: Experimental average normal stress, QSVM, and SLR predicted average normal stress distributions for 0.2 µg/ml chalcone concentration (a-c). Experimental maximum shear stress, QSVM, and SLR predicted maximum shear stress distributions for 0.2 µg/ml chalcone concentration (d-f). Experimental average normal stress, QSVM, and SLR predicted average normal stress distributions for 2 µg/ml chalcone concentration (g-i). Experimental maximum shear stress, QSVM, and SLR predicted maximum shear stress distributions for 2 µg/ml chalcone concentration (j-l). All QSVM and SLR predictions made using multiple area training sets

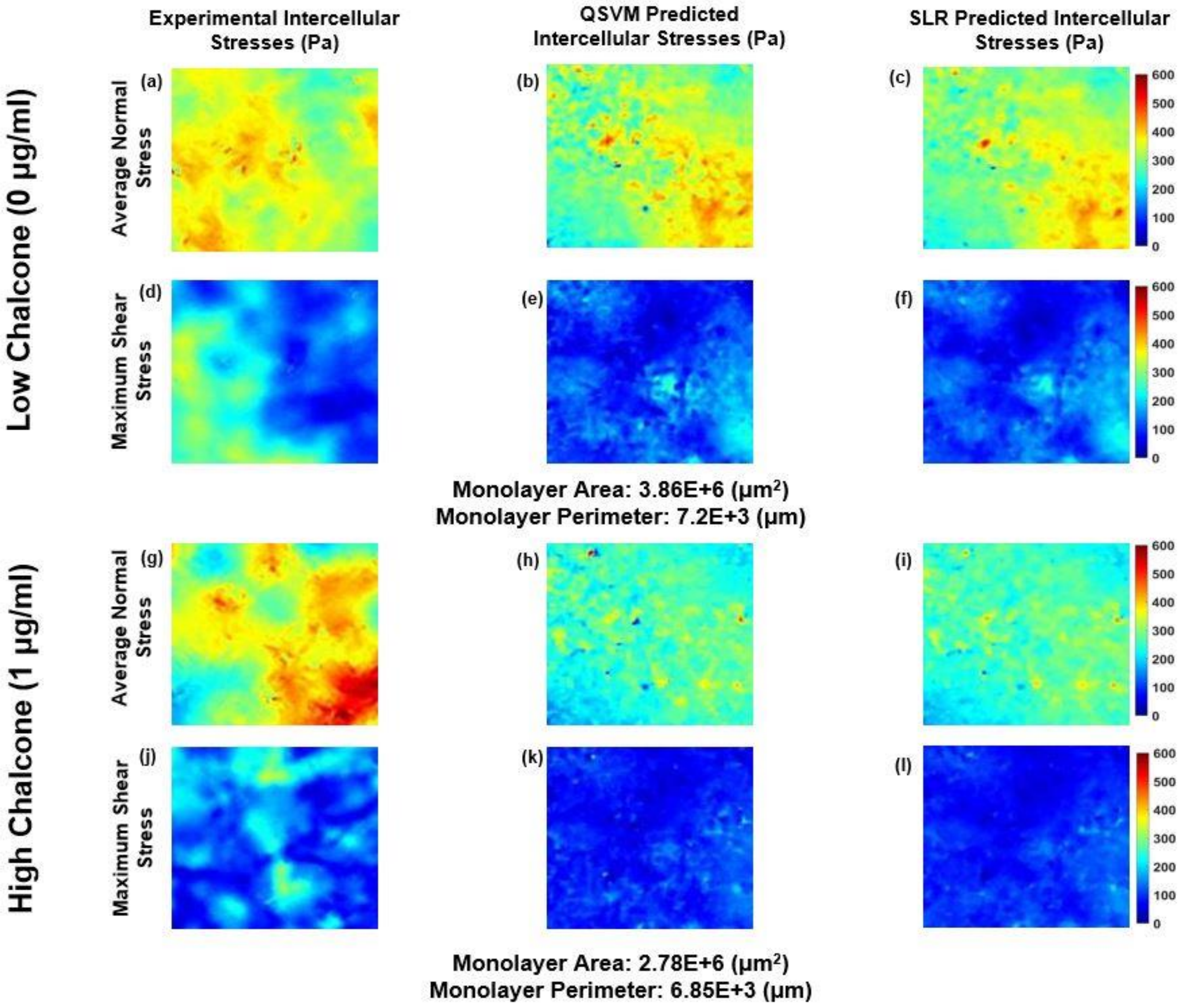

Figure 73: Experimental average normal stress, QSVM, and SLR predicted average normal stress distributions for 0 µg/ml chalcone concentration (a-c). Experimental maximum shear stress, QSVM, and SLR predicted maximum shear stress distributions for 0 µg/ml chalcone concentration (d-f). Experimental average normal stress, QSVM, and SLR predicted average normal stress distributions for 1 µg/ml chalcone concentration (g-i). Experimental maximum shear stress, QSVM, and SLR predicted maximum shear stress distributions for 1 µg/ml chalcone concentration (j-l). All QSVM and SLR predictions made using multiple area training sets

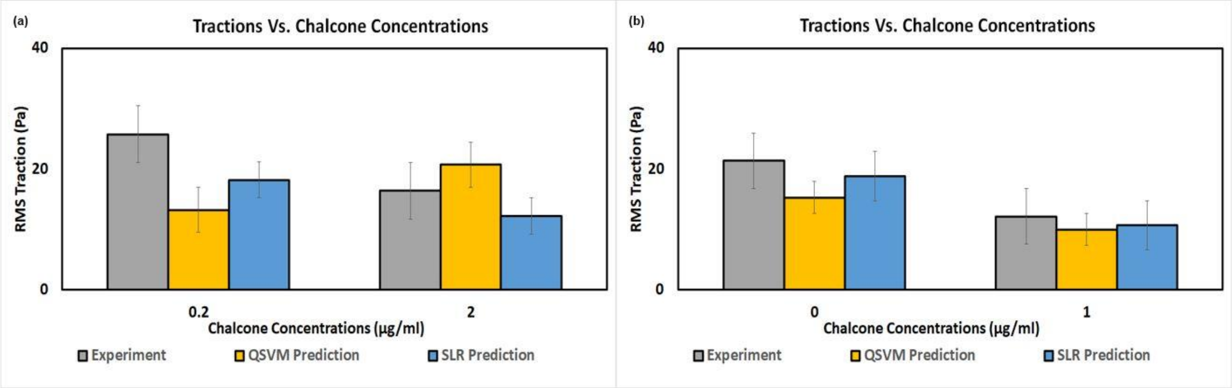

Figure 74: RMS traction experimental results, QSVM, and SLR predictions utilizing multiple area training set for 0.2 µg/ml and 2 µg/ml (a) and 0 µg/ml and 1 µg/ml (b) chalcone concentrations

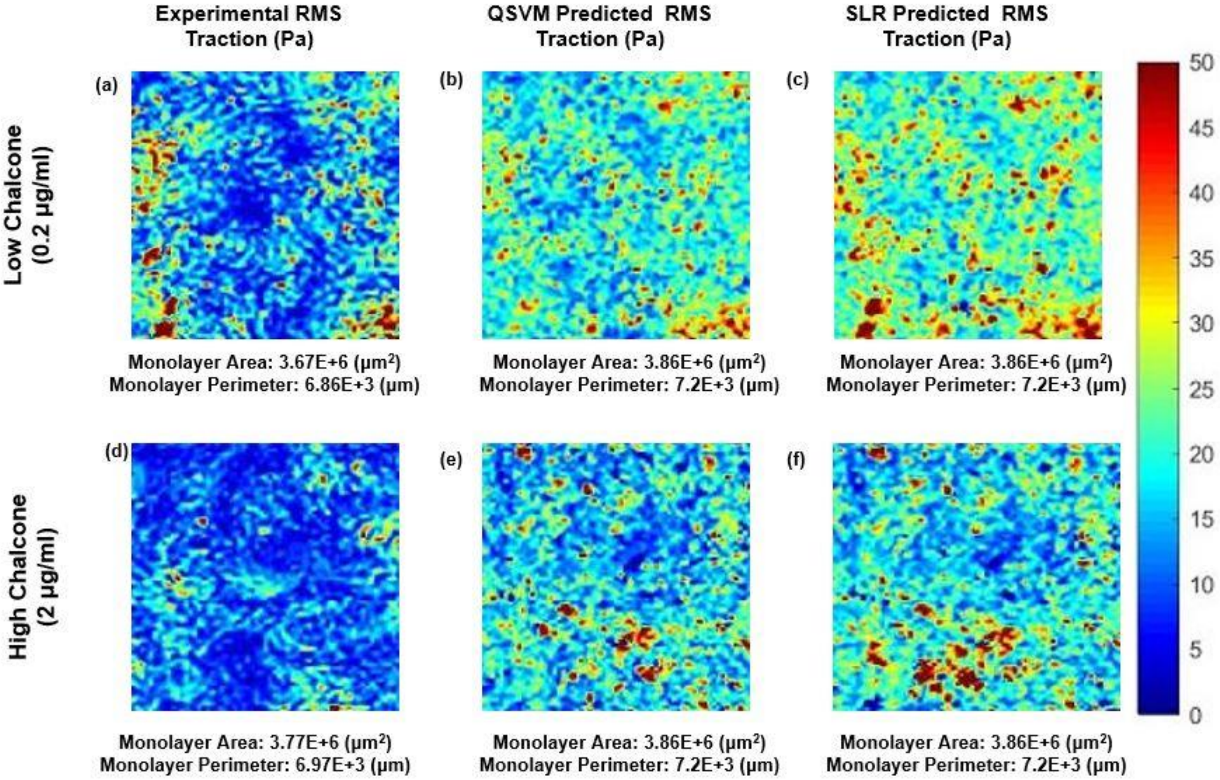

Figure 75: Experimental RMS traction, QSVM, and SLR predicted RMS traction distributions for 0.2 µg/ml chalcone concentration (a-c) and 2 µg/ml chalcone concentration (d-f) utilizing multiple area training set

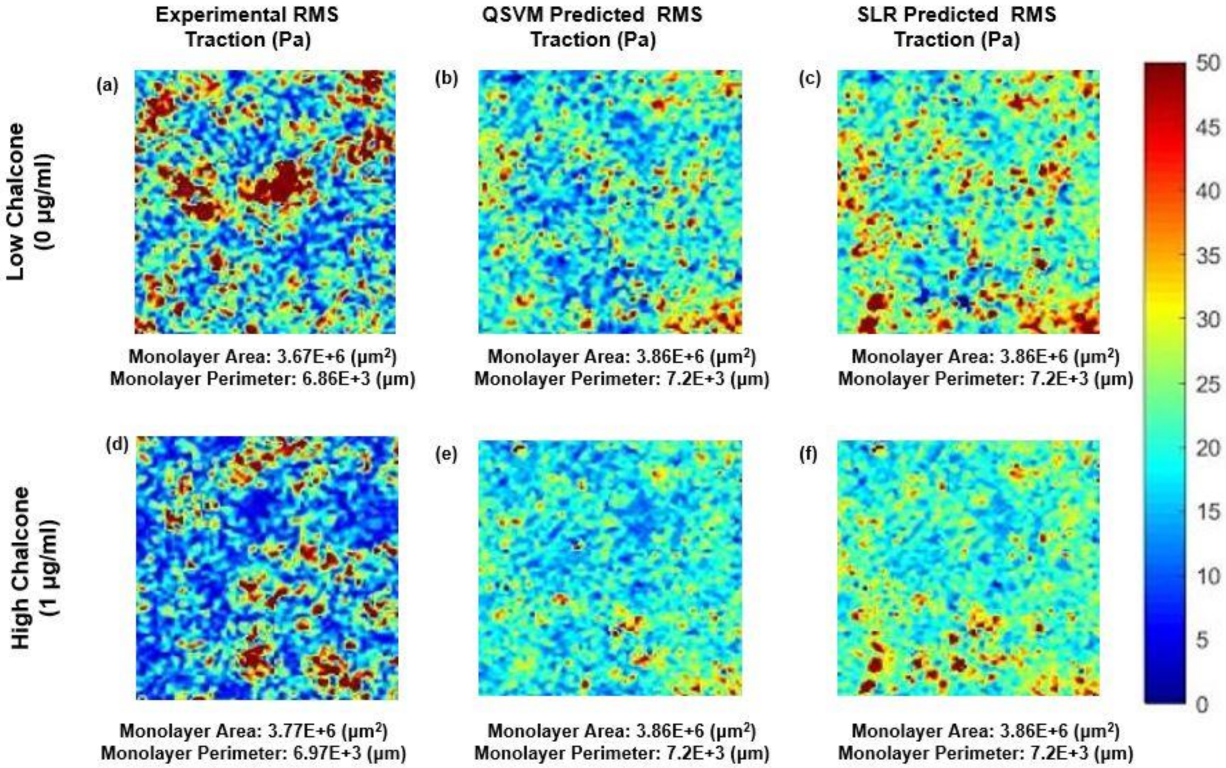

Figure 76: Experimental RMS traction, QSVM, and SLR predicted RMS traction distributions for 0 µg/ml chalcone concentration (a-c) and 1 µg/ml chalcone concentration (d-f) utilizing multiple area training set

Table 3: Overall R^2 of Intercellular stress and RMS Traction predictions using ML models from single area and multiple area training sets for different chalcone treatment concentrations based on average from 3 monolayer samples for each condition

Single Area Training			**Multiple Area Training**	
Avg Normal	**SLR Model**	**QSVM Model**	**SLR Model**	**QSVM Model**
R^2	0.74	0.7	0.67	0.81
RSME (Pa)	24.18	27.5	24.49	22.20
Max Shear	**SLR Model**	**QSVM Model**	**SLR Model**	**QSVM Model**
R^2	0.88	0.84	0.87	0.93
RSME (Pa)	47.26	53.57	49.06	52.67
RMS Traction	**SLR Model**	**QSVM Model**	**SLR Model**	**QSVM Model**
R^2	0.51	0.54	0.85	0.008
RSME (Pa)	6.5	5.0	4.56	7.37

Table 4: Intercellular stress predictions using ML models from single area and multiple area training sets for different chalcone treatment concentrations based on average from 3 monolayer samples for each condition

Experimental Results Average Normal Stress (Pa)		**Single Area Training**		**Multiple Area Training**	
		SLR Model (Pa)	**QSVM Model (Pa)**	**SLR Model (Pa)**	**QSVM Model (Pa)**
0µg/ml	136.19±25	150±13	144.6±9	160±7	145.3±7
1µg/ml	114.71±3	105.5±4	107.6±5	103.2±7	100.4±8
0.2µg/ml	192±32	146.6±8	138.2±8	154.4±7	152±7
2 µg/ml	76.75±14	78.8±5	80.5±2	93.6±1	86.2±0.4
Experimental Results Maximum Shear Stress (Pa)		**Single Area Training Set Predictions**		**Multiple Area Training Set Predictions**	
		SLR Model (Pa)	**QSVM Model (Pa)**	**SLR Model (Pa)**	**QSVM Model (Pa)**
0µg/ml	129±20	90.7±6	82.3±5	85.9±4	78.6±1
1µg/ml	54.3±4	43.6±6	44.8±5	50.8±6	48.3±6
0.2µg/ml	172±73	88.5±6	78.4±4	84.3±4	80.7±4
2 µg/ml	63.8±4	44.6±2	44.6±1	56.6±3	50.6±2

Table 5: RMS Traction predictions using ML models from single area and multiple area training sets for different chalcone treatment concentrations based on average from 3 monolayer samples for each condition

Experimental Results		Single Area Training		Multiple Area Training	
RMS Tractions (Pa)		SLR Model (Pa)	QSVM Model (Pa)	SLR Model (Pa)	QSVM Model (Pa)
0µg/ml	21.4±3	28.6±6	18±2	18.8±1	15.3±1
1µg/ml	12.2±0.4	18.8±2	11.3±1	10.6±1	10±1
0.2µg/ml	25.7±5	25±5	16.3±2	18.2±1	13.2±1
2 µg/ml	16.4±4	24.8±7	16.4±3	12.2±1	20.7±5

Discussion

In this paper, for the very first time, we have predicted both tractions and intercellular stresses mainly as a function of a drug (chalcone) concentration using regression learning models QSVM and SLR with two different training sets, utilizing one of the monolayer area and perimeter or window area and perimeter along with chalcone concentration as the predictors depending on the training method chosen. Overall, SLR models did well with single area training set while the QSVM model did better than SLR for multiple area training set except for traction predictions. The R^2 of intercellular stress predictions was the highest for the QSVM model utilizing a multiple area training set ($R^2 = 0.81$ for average normal stress and $R^2 = 0.93$ for maximum shear stress). SLR model utilizing multiple area training set had the highest R^2 value of 0.85 for traction predictions. A very low R^2 value (0.008) for RMS traction predictions using QSVM with multiple area training sets could be attributed to the unconstrained traction data with potential boundary effects from edges that were used to train the regression models. Training of datasets and predictions were done utilizing MATLAB's parallel computing toolbox with 4 Core Intel i7-7700 CPU (3.60 GHz & 32 GB RAM). Training time was almost the same (5 hrs) for both single and multiple area methods with SLR & SVM-based regression models. The memory requirement to store the trained regression models was very high for both single & multiple area methods (~1-2 GB per model) for 292 images and very low for the average table method (32 MB per model). Also, multiple area training requires preprocessing to extract input variables from the new data (image) for making predictions while the single area method requires very little preprocessing for extracting the independent variables. The prediction time for a new (unseen) image was relatively same across the all the ML models built on the two different training sets (~10-20 min).

Out of the two proposed training sets, ML models built on multiple area training were very much sensitive to the outliers. In the multiple area method, the predictions from all the three regression models (SLR, LSVM, and QSVM) were subject to a filter that excludes the outliers < -1000 Pa & > +1000 Pa (values corresponding to 0.15th, 99.95th percentile) for intercellular stresses and > +600 Pa (values corresponding to the 99.95th percentile) for RMS tractions to filter noise due to overfitting. Also, the most important feature of the multiple area method is the ability to generate time-series predictions of tractions and intercellular stresses based on the changes in area & perimeter observed in each small overlapping grid across the entire field of view. The R^2 especially for tractions can be improved by using more predictors such as substrate stiffness, cell orientation, cell velocity, etc. Also, training the models using a cropped monolayer section inside the circular monolayer samples could reduce the noise due to boundary effects and improve prediction accuracy. Time series prediction is possible with multiple area training but R^2 was too low because of overfitting due to noise for both tractions and intercellular stresses. One of the future works is to reduce the boundary effects of the training sets by using cropped subsets inside the monolayer and employing cell velocity as an independent variable for time-series predictions. However, including cell velocity as a predictor can increase the pre-processing and computation time compared to window-based and monolayer area predictors. Other future works include making time-series predictions for expanding monolayer using single area training sets and explore with more predictors such as cell velocity, cell orientation, curvature, cell area, ECM concentration, and substrate stiffness.

Conclusion

Intercellular stresses and tractions measured from a HUVEC monolayer can depend on a wide variety of factors such as monolayer area, substrate stiffness, cell area, curvature, external forces & biochemical substances, or drugs. Cell tractions have been correlated to factors like substrate stiffness, cell area, local curvature, and cell geometry. Bayesian inversion stress microscopy (BISM) and Kalman inversion stress microscopy (KISM) were recently introduced to predict intercellular stresses from traction force microscopy. However, we believe this is the very first work to predict both tractions and intercellular forces from the independent variables: drug concentration, monolayer area, monolayer perimeter, window area, and window perimeter based on prior knowledge of tractions and intercellular stresses. We predicted both tractions and intercellular stresses using QSVM and SLR regression learners built on two different training sets.

The coefficient of determination (R^2) values were the highest for maximum shear stress compared to average normal stress and RMS tractions which were relatively consistent across different ML models based on averages from 3 samples for each drug concentration. The inclusion of more predictors such as substrate stiffness should increase the prediction accuracy (R^2) of the regression learners. With these promising results, we can incorporate more predictors such as cell velocity, substrate stiffness, ECM concentration, etc., to improve the accuracy of the current models to make more reliable predictions of stress distributions and time-series predictions instead of just the average trend. This work will be helpful for accelerating research in experimental drugs and targeted drug therapy. Proposed ML models could be applicable for testing cell mechanics of any anchorage-dependent cells as a function of pharmacological and other morphological parameters that can influence cell mechanics.

Supplementary

SVM Theory, Advantages, and Disadvantages

SVM uses the kernelization technique to map the data into higher dimensions which makes it easier to establish relationships between the predictors and response variable. The hyperplane in the support vector machine regression learner is the plane that has the greatest number of data points. Epsilon is the width or the acceptable error from the hyperplane. The points closer to the hyperplane are called the support vectors. Depending on the kernel used for transforming the input data into higher dimensions to find the hyperplane that captures the most data points there are different types of SVM like LSVM (Linear), QSVM (Quadratic), Gaussian SVM, etc. ‘w’ is the slope of the linear fit with y-intercept ‘b’. ‘ε’ is the tolerance level of the model and ‘ξ’ is the bias term added to penalize the model from overfitting the data.

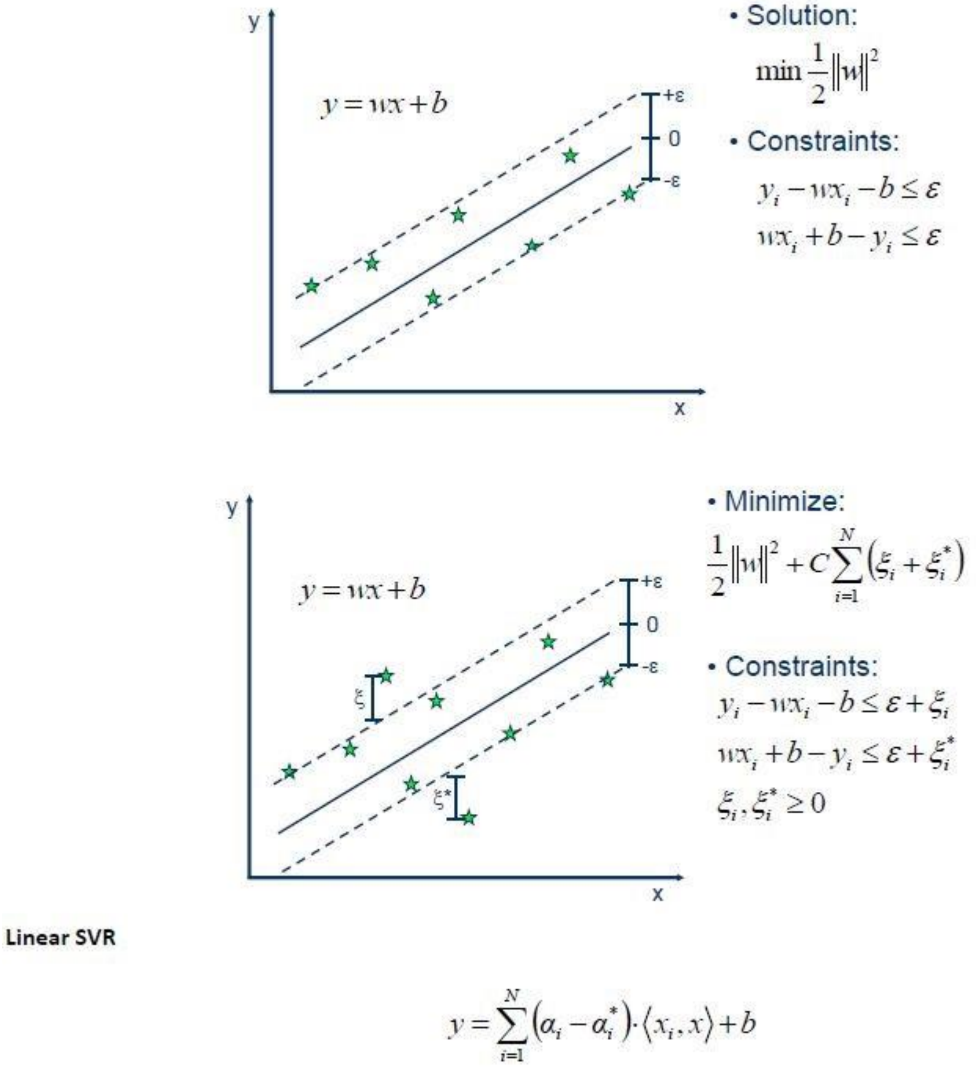

Figure 77: Mathematical description of Support Vector Machines using Linear Kernel with tuneable hyperparameters (ε and ξ) [83, 85]

$$y = \sum_{i=1}^{N} \left(\alpha_i - \alpha_i^*\right) \cdot \langle \varphi(x_i), \varphi(x) \rangle + b$$

$$y = \sum_{i=1}^{N} \left(\alpha_i - \alpha_i^*\right) \cdot K(x_i, x) + b$$

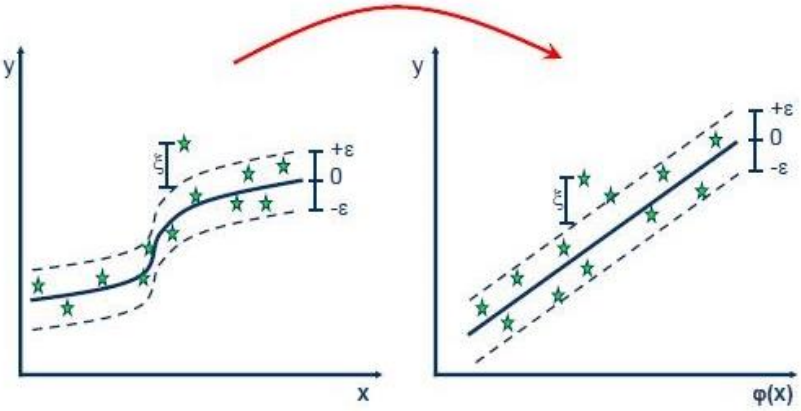

Kernel functions

Polynomial

$$k(\mathrm{x}_i, \mathrm{x}_j) = (\mathrm{x}_i . \mathrm{x}_j)^d$$

Gaussian Radial Basis function

$$k(\mathrm{x}_i, \mathrm{x}_j) = \exp\left(-\frac{\left\|\mathrm{x}_i - \mathrm{x}_j\right\|^2}{2\sigma^2}\right)$$

Figure 78: Mathematical description of Non-linear Support Vector Machines transforming data into higher dimensions for linear fit using Polynomial and Gaussian Kernels [85]

SVM models are used because they don’t overfit, relatively easier to update the models with high generalized prediction accuracy.[83] However, SVM can struggle with large datasets and is also susceptible to noise and cases where the number of features is high [83]. The theory of Stepwise Linear Regression (SLR) and its advantages and disadvantages were discussed in the materials and methods section of this chapter.

Feature Extraction and Building Training Sets

The training sets for the ML models were built similar to what was described in chapter five. The pictorial depiction of the features extracted for the single area and multiple area training sets are described below.

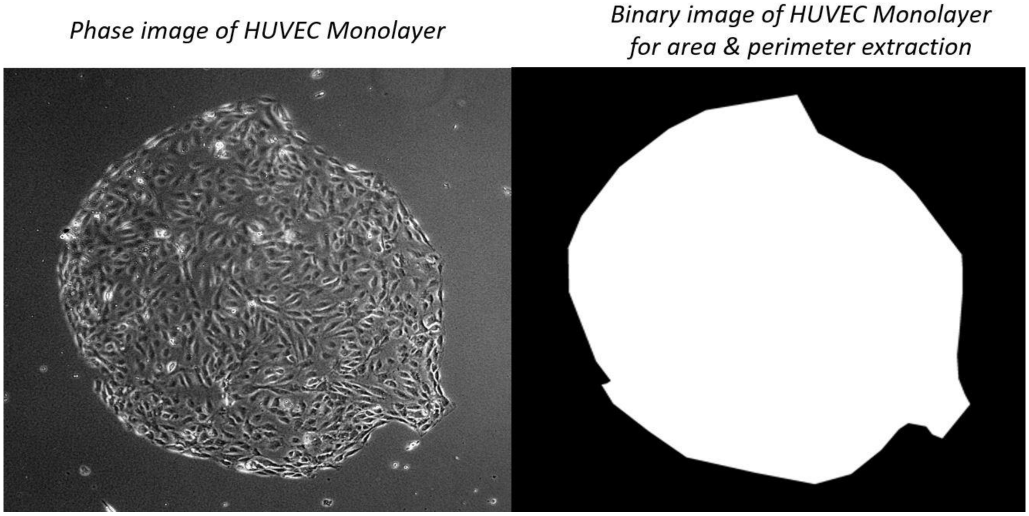

Figure 79: Monolayer area and monolayer perimeter extracted from the phase contrast images for building the single area training sets

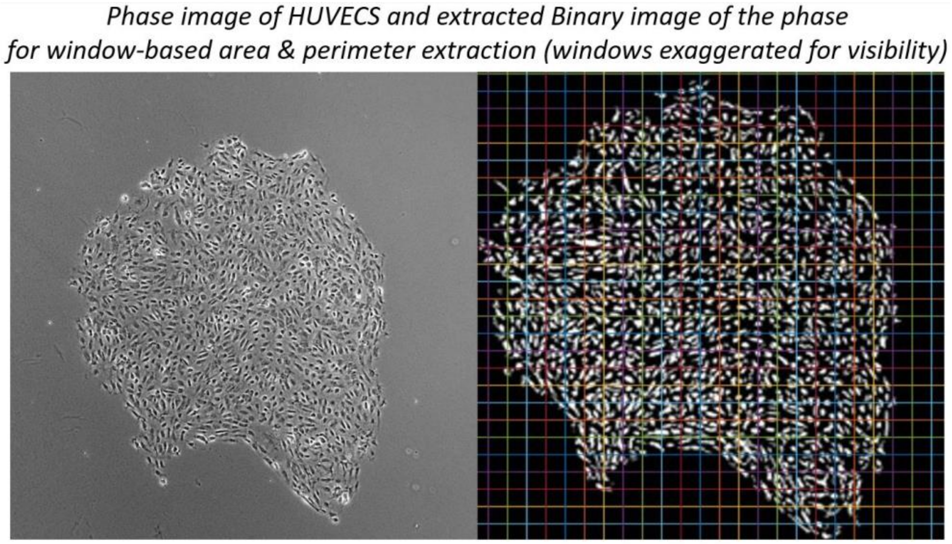

Figure 80: Window area and window perimeter extracted from the binarized phase contrast image for building the multiple area training sets

1 Area	2 Perimeter	3 Chalcone	4 Pmin
3084044	1.0676e+04	2	-160.0167
3084044	1.0676e+04	2	-164.1059
3084044	1.0676e+04	2	-136.0450
3084044	1.0676e+04	2	-158.1152
3084044	1.0676e+04	2	-151.8531
3084044	1.0676e+04	2	-111.4324
3084044	1.0676e+04	2	-120.3128
3190777	9.7484e+03	0.2000	-120.6567
3190777	9.7484e+03	0.2000	-119.2099
3190777	9.7484e+03	0.2000	-98.9334
3190777	9.7484e+03	0.2000	-137.0209
3190777	9.7484e+03	0.2000	-156.5084
3190777	9.7484e+03	0.2000	-182.3077
3190777	9.7484e+03	0.2000	-186.9028
3190777	9.7484e+03	0.2000	-232.8746
3190777	9.7484e+03	0.2000	-233.7437
3190777	9.7484e+03	0.2000	-258.5291
2246702	6.5454e+03	0.2000	-1.1572e+03
2246702	6.5454e+03	0.2000	-1.7347e+03
2246702	6.5454e+03	0.2000	-1.7591e+03
2246702	6.5454e+03	0.2000	-1.8843e+03
2246702	6.5454e+03	0.2000	-1.6589e+03
2246702	6.5454e+03	0.2000	-1.4826e+03
2246702	6.5454e+03	0.2000	-1.4437e+03
2246702	6.5454e+03	0.2000	-1.4754e+03

Figure 81: Building single area training sets for training the ML models

The above figure shows the single area training sets using monolayer area, monolayer perimeter, and chalcone concentration as the predictors and the minimum principal stress (Pmin) as the response or dependent variable. Similarly, single area training sets were built for training maximum principal stress (Pmax). After training the model, the predictions were made for a new phase contrast image after extracting the input features (monolayer area, monolayer perimeter, and chalcone concentration). From the predicted maximum and minimum principal stresses, average normal stress and maximum shear stresses were calculated as mentioned in the research methodology section.

Similarly, training tables were built for multiple area sets by calculating the window area and window perimeter shown in figure 80 along with chalcone concentration as the predictors (independent variables/features). The window size and pixel shift of the overlapping windows were selected based on the settings used in the PIV (Particle Image Velocimetry) routine for calculating the displacement field in TFM. The choice of window size and overlap affects the accuracy and resolution of the predicted distributions as well as the actual experimental results.

Average (Multiple Area) Training Sets

This training set uses the average of response variables and predictors (from multiple area training sets) for all the images in a monolayer sample to build the training table. The average data from four different monolayer samples were coupled together as a single master table which was then trained using regression learner application in MATLAB. This method eliminates the need for a training table for each data point as seen in the previous two training sets (single and multiple area sets). The average master table created from the four samples contained 242,064 data points (60,516 response/predictor data per monolayer). Although the size of the single master training table generated using this method is large compared to each of the 60,516 tables from the single or multiple area methods, it is the least computationally expensive among other proposed training sets. The predictor used in the method can be monolayer area/perimeter, window area/perimeter, or a combination of both along with chalcone concentration (same as the multiple area sets). However, only the average values of window area & perimeter have been used as predictors along with chalcone concentration because of relatively higher spatial resolution of predicted distributions compared to predictions from monolayer area/perimeter.

For the average training sets, only one master trained model variable was created from a single master training table containing the averages of predictors and response variables from four monolayer samples (same as multiple area sets). In this case, a fit of the predicted results was directly obtained by using the ‘predictFcn’ command in MATLAB without making predictions sequentially for each datapoint. Prediction time for a single new phase image was around 20 minutes, 5 minutes, and 5-10 minutes for single area, multiple area, and average table methods respectively.

Average Training Set ML Predictions

The predictions were also made using SLR and QSVM models for three new samples for each of the four chalcone concentrations using the average table training set and compared against the corresponding experimental results. Overall R^2 for average normal stress predictions for different chalcone concentrations were 0.57 and 0.58 for SLR and QSVM models with RMSE of 30.66Pa and 29.83Pa respectively. For maximum shear stresses, the R^2 values were 0.85 and 0.85 for SLR and QSVM models with RMSE of 47.77Pa and 55.75Pa. The overall R^2 of RMS tractions for SLR and QSVM models were 0.87 and 0.78 with RMSE of 7.36Pa and 10.41Pa respectively.

The training time for the average tables method was very low for the SLR model (10-15 min) but very high for SVM models (~8 hrs). The average table method was the least sensitive to noise but more prone to underestimation of intercellular stresses and tractions compared to the other two methods.

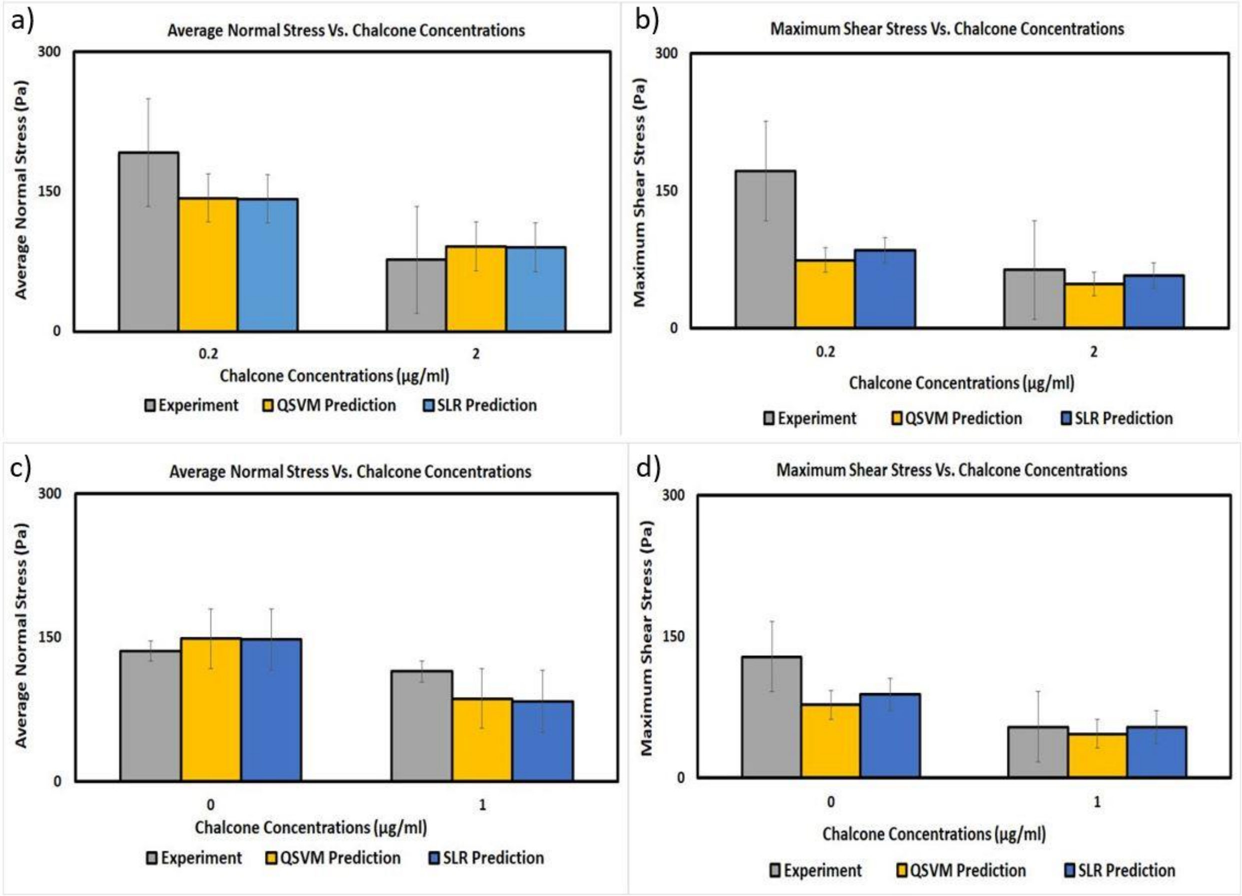

Figure 82: Average normal stress and maximum shear stress experimental results, QSVM, and SLR predictions utilizing average training set for 0.2 µg/ml and 2 µg/ml (a and b) and 0 µg/ml and 1 µg/ml (c and d) chalcone concentrations

The predictions were also made using Linear Support Vector Machine (LSVM) which didn't produce better accuracy for single and multiple area training sets. The stress distributions predicted by different models utilizing average training sets are shown in the following figures.

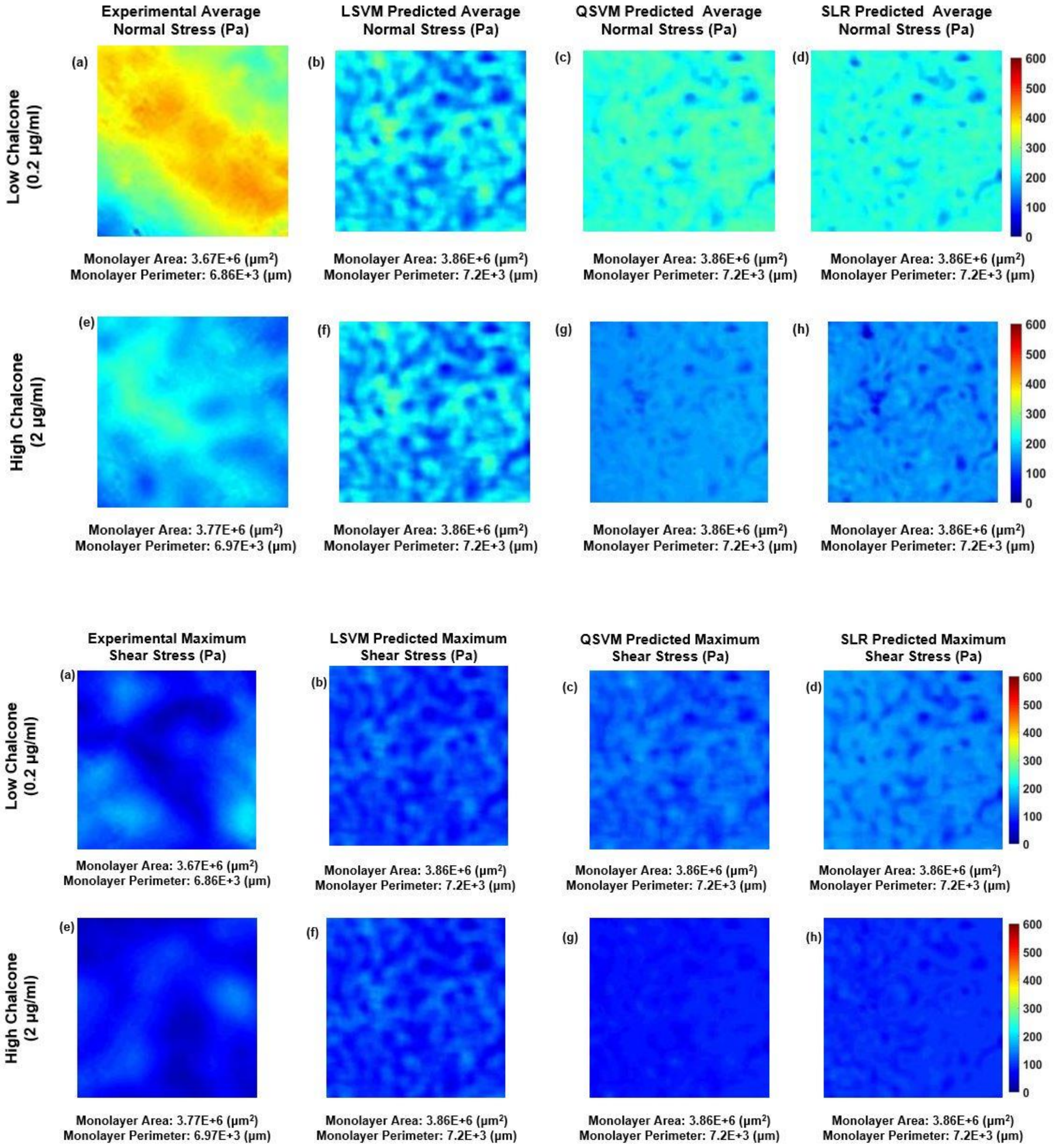

Figure 83: Experimental average normal stress, LSVM, QSVM, and SLR predicted average normal stress distributions for 0.2µg/ml chalcone concentration (a-d). Experimental maximum shear stress, LSVM, QSVM, and SLR predicted maximum shear stress distributions for 0.2 µg/ml chalcone concentration (a-d). Experimental average normal stress, LSVM, QSVM, and SLR predicted average normal stress distributions for 2 µg/ml chalcone concentration (e-h). Experimental maximum shear stress, LSVM, QSVM, and SLR predicted maximum shear stress distributions for 2 µg/ml chalcone concentration (e-h). All LSVM, QSVM, and SLR predictions made using average training sets

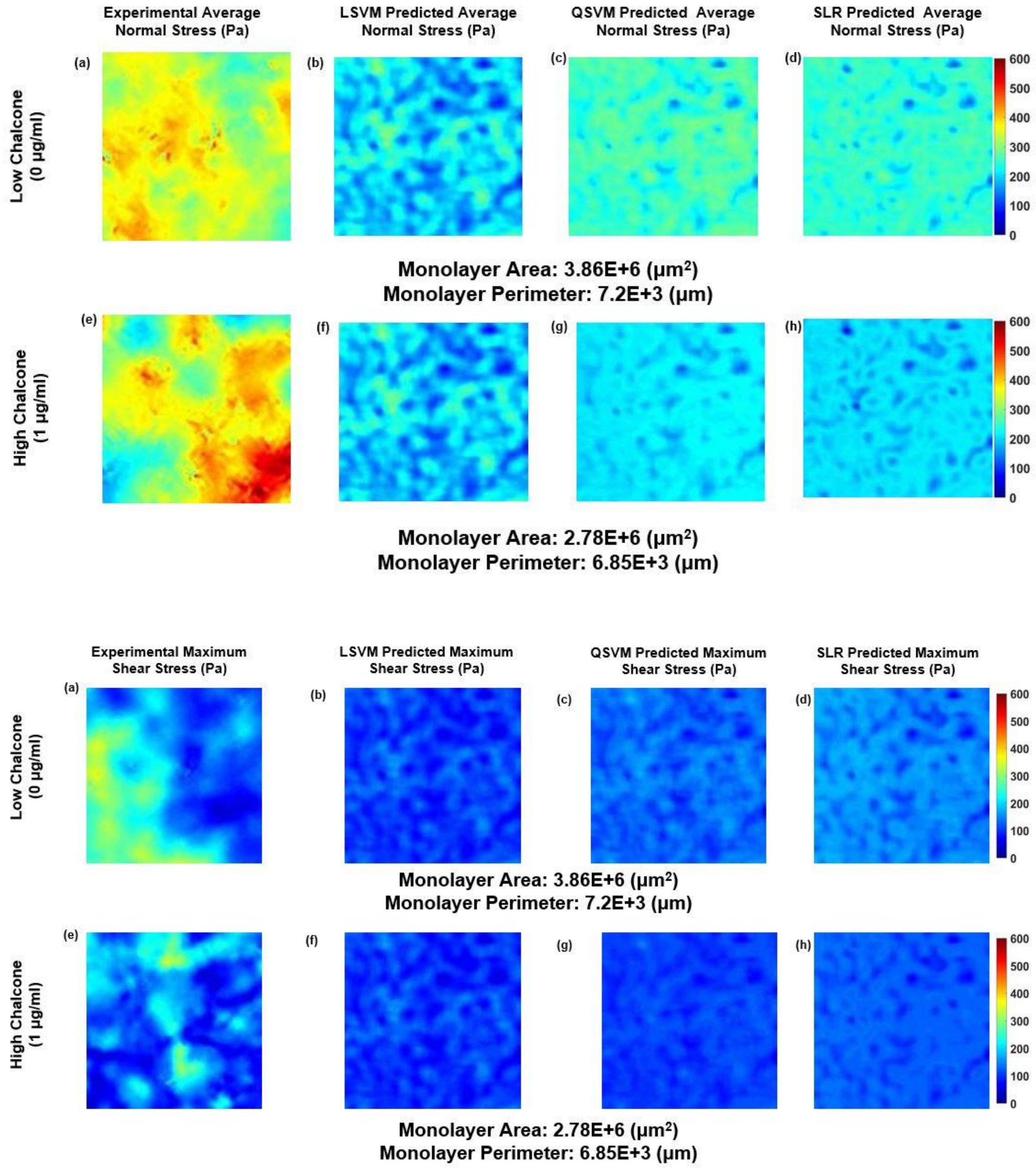

Figure 84: Experimental average normal stress, LSVM, QSVM, and SLR predicted average normal stress distributions for 0µg/ml chalcone concentration (a-d). Experimental maximum shear stress, LSVM, QSVM, and SLR predicted maximum shear stress distributions for 0µg/ml chalcone concentration (a-d). Experimental average normal stress, LSVM, QSVM, and SLR predicted average normal stress distributions for 1 µg/ml chalcone concentration (e-h). Experimental maximum shear stress, LSVM, QSVM, and SLR predicted maximum shear stress distributions for 1 µg/ml chalcone concentration (e-h). All LSVM, QSVM, and SLR predictions made using average training sets

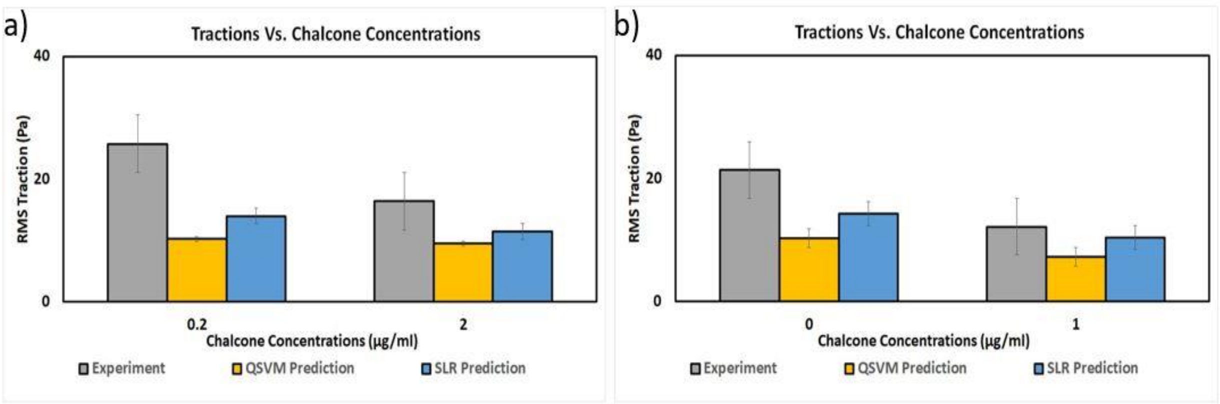

Figure 85: RMS tractions from experimental results, QSVM, and SLR predictions utilizing average training set for 0.2 µg/ml and 2 µg/ml (a) and 0 µg/ml and 1 µg/ml (b) chalcone concentrations

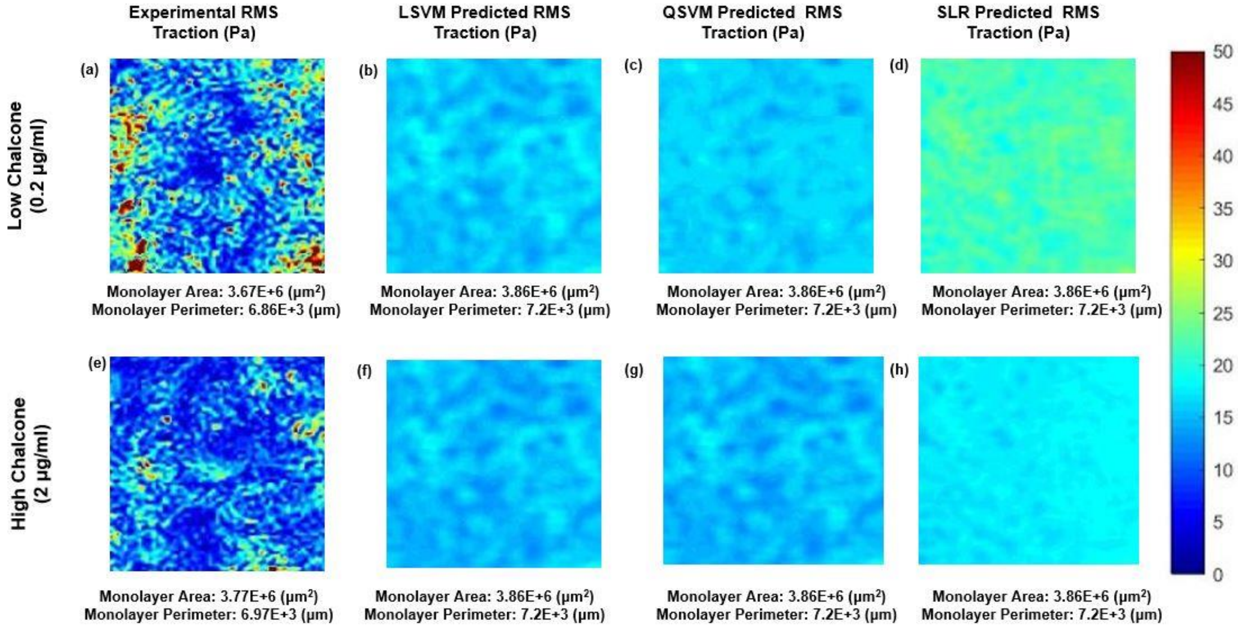

Figure 86: Experimental RMS traction, LSVM, QSVM, and SLR predicted RMS traction distributions for 0.2µg/ml chalcone concentration (a-d) and 2µg/ml chalcone concentration (e-h) utilizing average training set

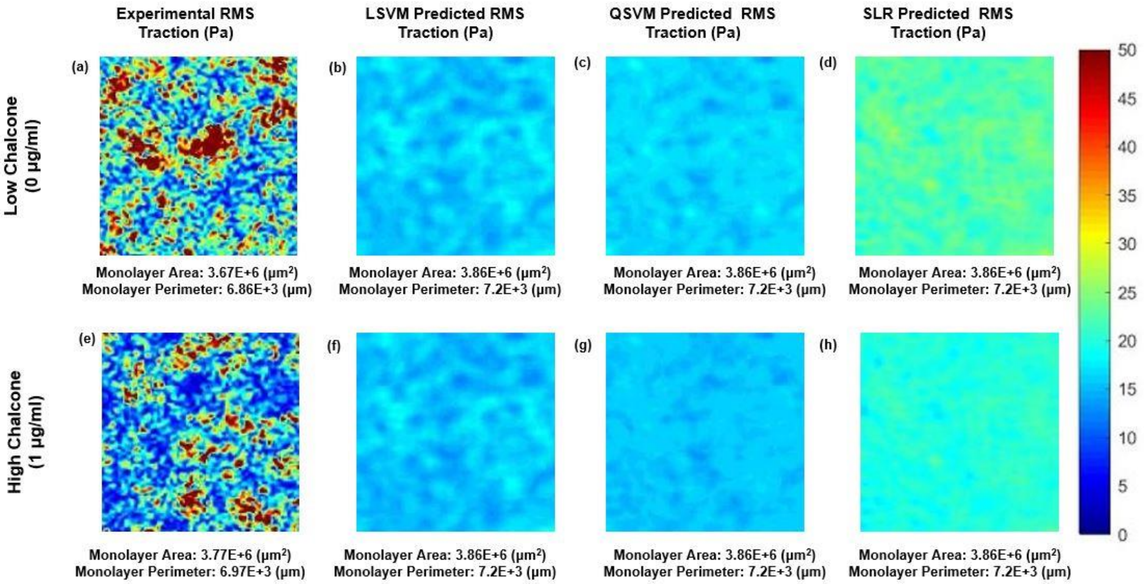

Figure 87: Experimental RMS traction, LSVM, QSVM, and SLR predicted RMS traction distributions for 0µg/ml chalcone concentration (a-d) and 1µg/ml chalcone concentration (e-h) utilizing average training set

Predictions for 1µg/ml

As mentioned from all these three different training sets, predictions were mainly made using QSVM and SLR models. LSVM models were also sensitive to the input features but the accuracy was poor for certain training sets and very similar to QSVM and SLR predictions.

Single Area Training Set Results for 1µg/ml Predictions

LSVM was poor for single area training sets and was relatively better for multiple and average training sets. The ML models were trained from each of these three training sets (based on data from 4 monolayers; 2 samples with 0.2µg/ml and 2 samples with 2µg/ml chalcone treatments) for each response variable (maximum, minimum principal stresses, and tractions). The results for the single area training set, multiple area training set, and average training sets for eight unseen phase images pertaining to 1µg/ml chalcone treatment were shown in the following section.

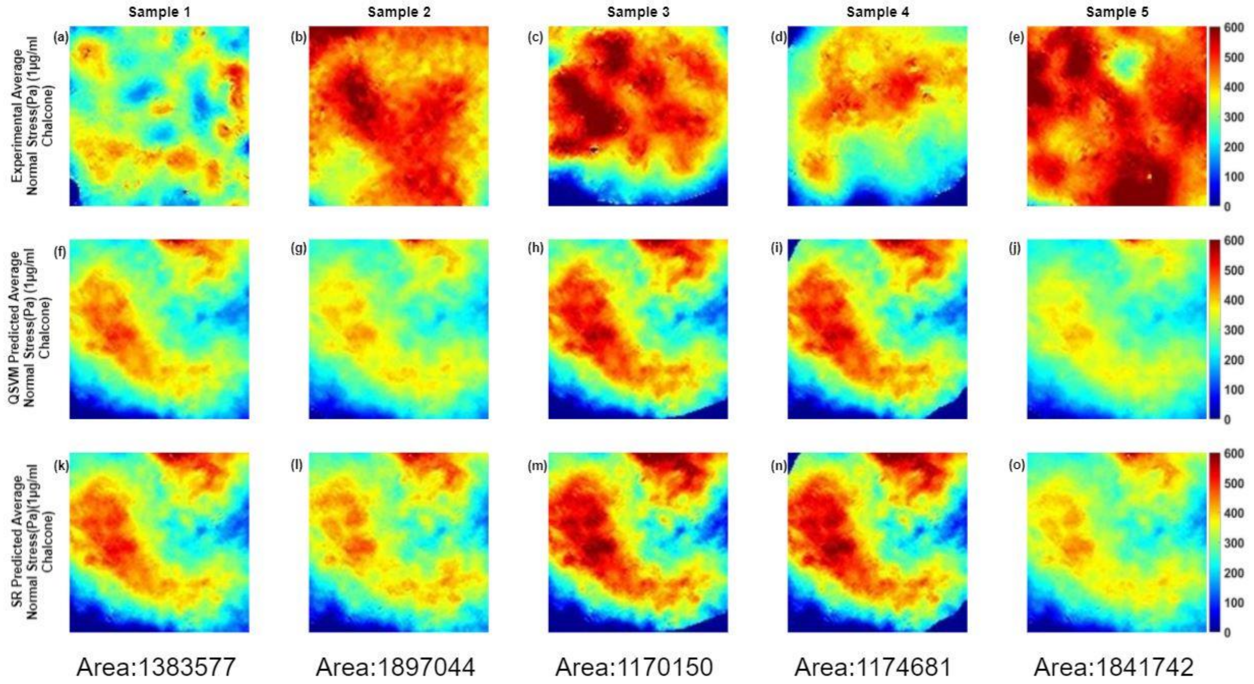

Figure 88: Experimental (a-e) average normal stresses and corresponding QSVM (f-j), and SLR (k-o) predictions utilizing single area training sets with monolayer area (Sq.Pixels)

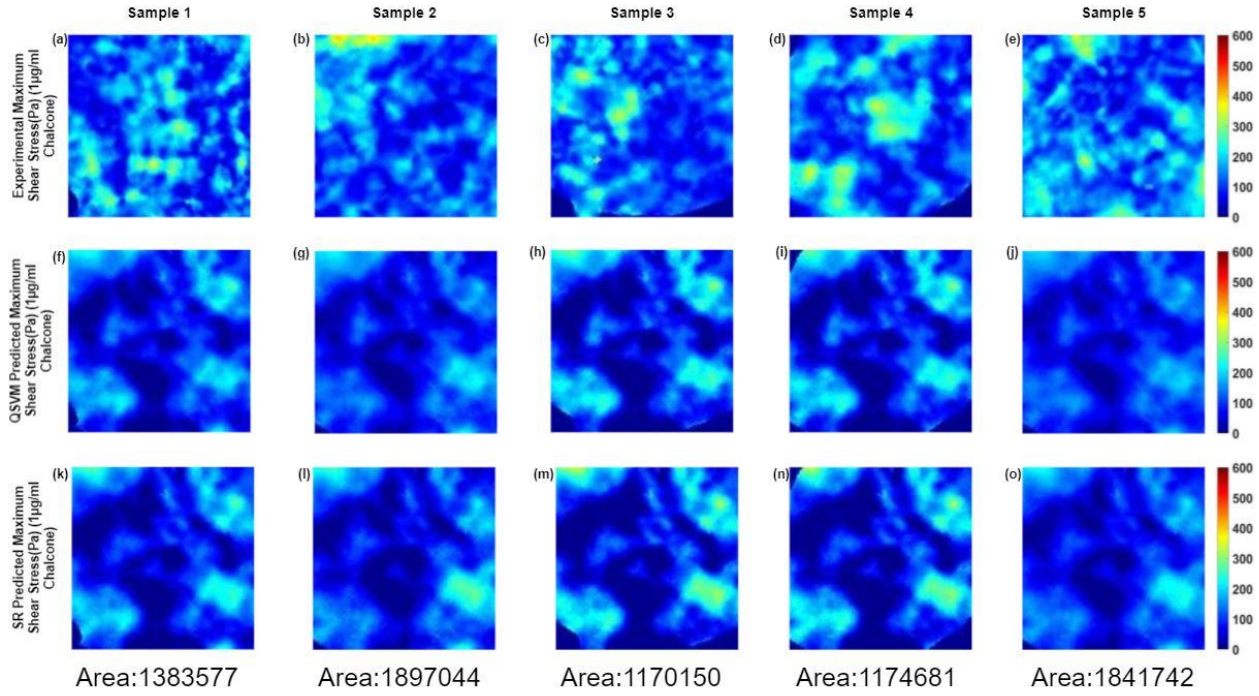

Figure 89: Experimental (a-e) maximum shear stresses and corresponding QSVM (f-j), and SLR (k-o) predictions utilizing single area training sets with monolayer area (Sq.Pixels)

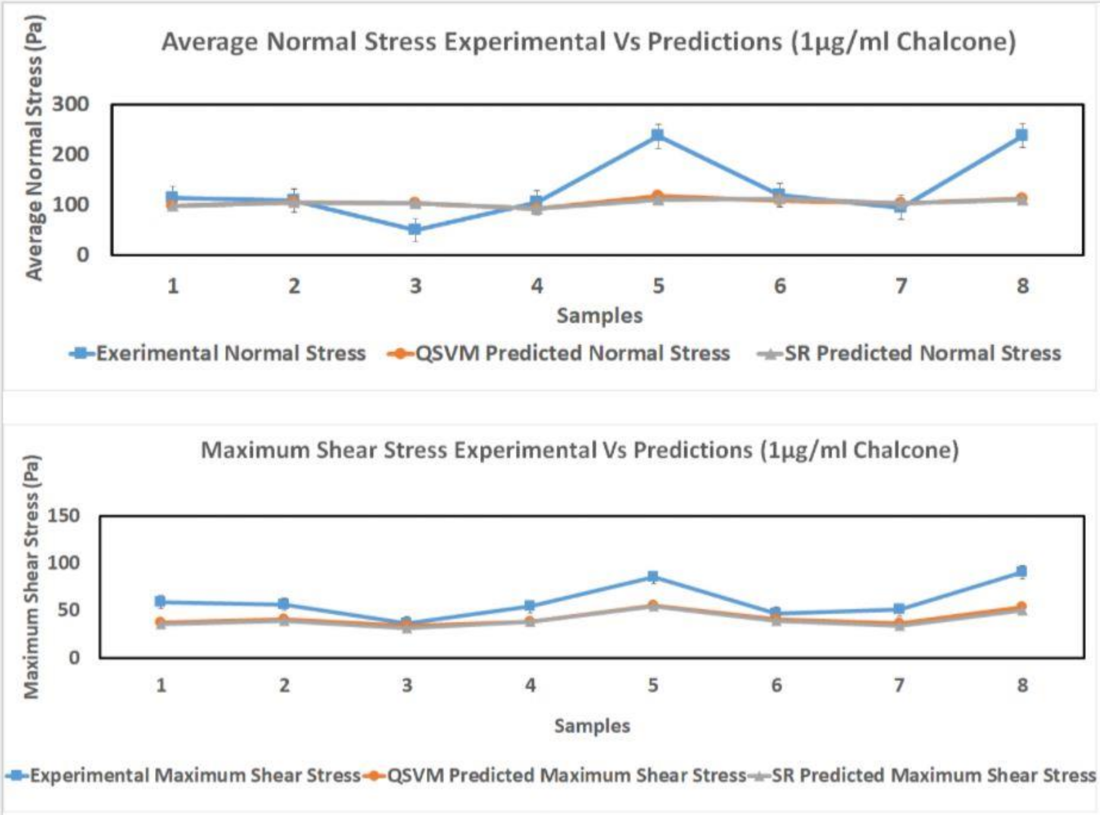

Figure 90: Average experimental results from 8 samples and the corresponding average normal and maximum shear stress predictions using single area training sets

The Pearson (R) correlation and Root Mean Square Error (RMSE) for average normal stress predictions and maximum shear stress predictions based on average from 8 unseen samples based on comparison with test data (actual experimental averages from 8 samples).

The ML models were trained using data from 4 samples with 2 different chalcone concentrations (0.2 & 2 μg/ml). The predictions were made for 8 new samples with 1 μg/ml chalcone concentration using the trained ML models (see in the Supporting Material). The predictions were compared with the experimental results from TFM & MSM. For the single area training set, R^2 values were 0.27 & 0.55 respectively for average normal intercellular stress predictions from SLR and QSVM models. In the case of maximum intercellular shear stress, R^2 values were 0.86 &

0.89 respectively for SLR and QSVM predictions. RMSE of the predictions from the SLR and QSVM models was 66.83Pa and 64.56Pa respectively for average normal stress and 22.47Pa and 20.85 Pa respectively for maximum shear stress. SLR & QSVM RMS traction predictions had poor accuracy (R^2) of 0.014Pa and 0.0005Pa respectively based on predicted averages from the 8 samples with 1 µg/ml chalcone treatment.

Table 6: R and RMSE for QSVM and SLR models utilizing single area training sets for 1ug/ml predictions

Avg Normal	**SLR Model**	**QSVM Model**
R	0.52	0.74
RMSE (Pa)	66.83	0.742
Max Shear	**SLR Model**	**QSVM Model**
R	0.93	0.94
RMSE (Pa)	22.47	20.85
RMS Tractions	**SLR Model**	**QSVM Model**
R	0.12	-0.022
RMSE (Pa)	7.63	1.9

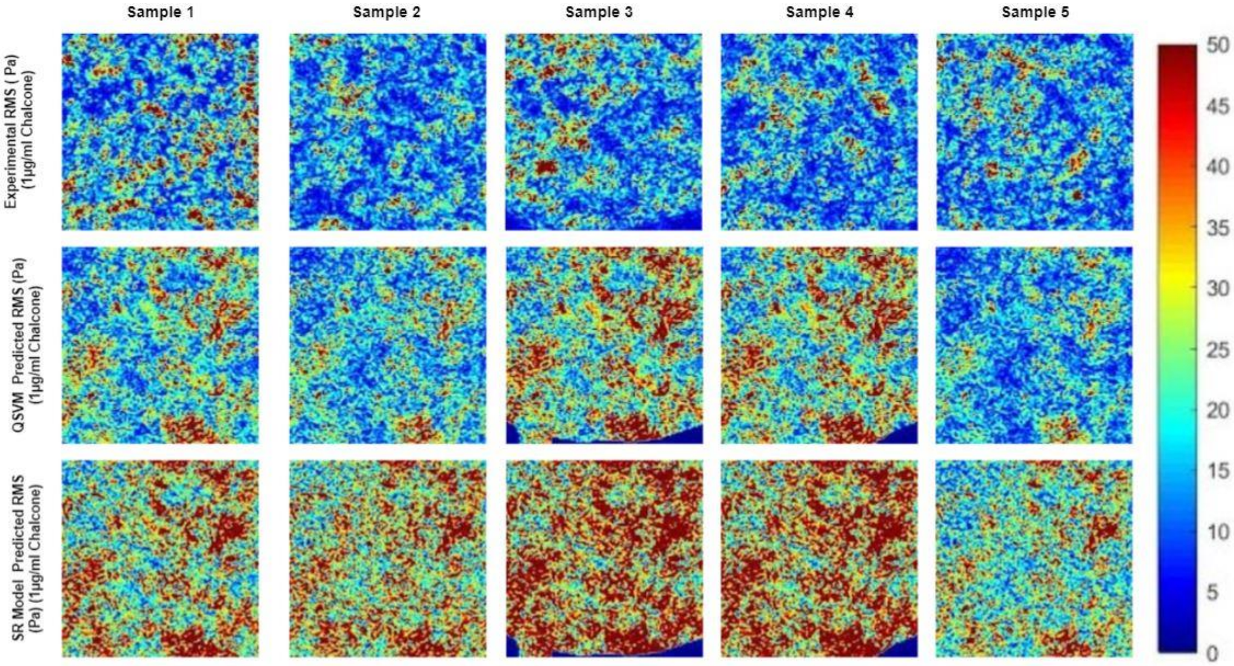

Figure 91: Experimental (a-e) RMS tractions and corresponding LSVM (f-j), and QSVM (k-o), SLR (p-t) predictions utilizing single area training sets with monolayer area (Sq.Pixels)

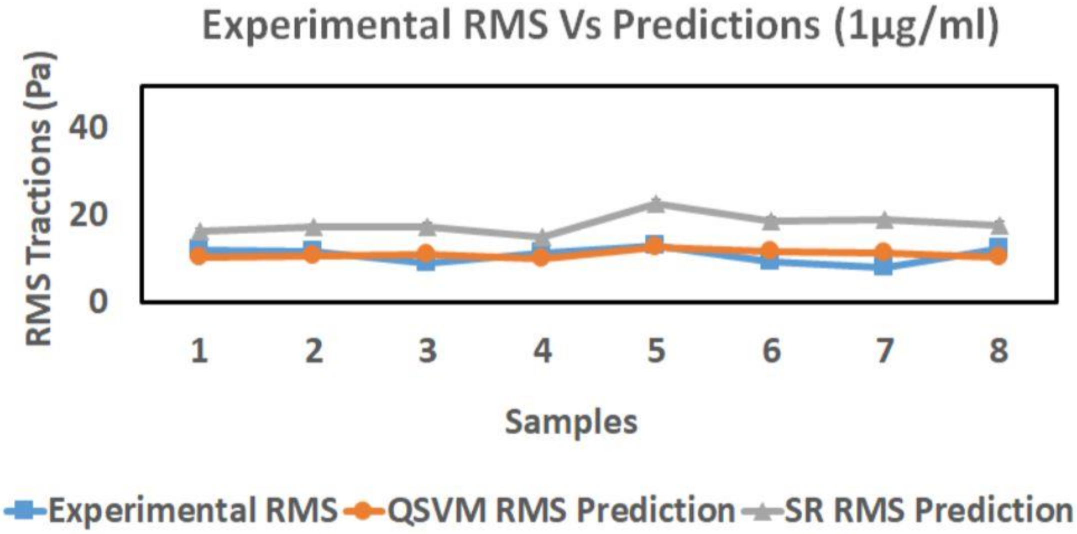

Figure 92: Average experimental results from 8 samples and the corresponding average RMS traction predictions using single area training sets

Multiple Area Training Set Results for 1µg/ml Predictions

Similar to results from previous results, predictions were made for 8 new samples with 1 µg/ml chalcone concentration using SLR and QSVM models with multiple area training sets. R^2 for SLR and QSVM models, for average normal stress predictions, were 0.80 and 0.85 respectively when compared to the actual average MSM experiment results from the same 8 samples. R^2 of SLR and QSVM models for average maximum stress predictions were 0.93 and 0.93 respectively. For RMS traction predictions, R^2 values were 0.58 and 0.62 respectively for SLR and QSVM models. RMSE of the predictions from the SLR and QSVM models was 64.60Pa and 66.03Pa respectively for average normal stress, 17.35Pa and 19.46 respectively for maximum shear stress, and 1.56Pa and 2.23Pa respectively for RMS traction predictions.

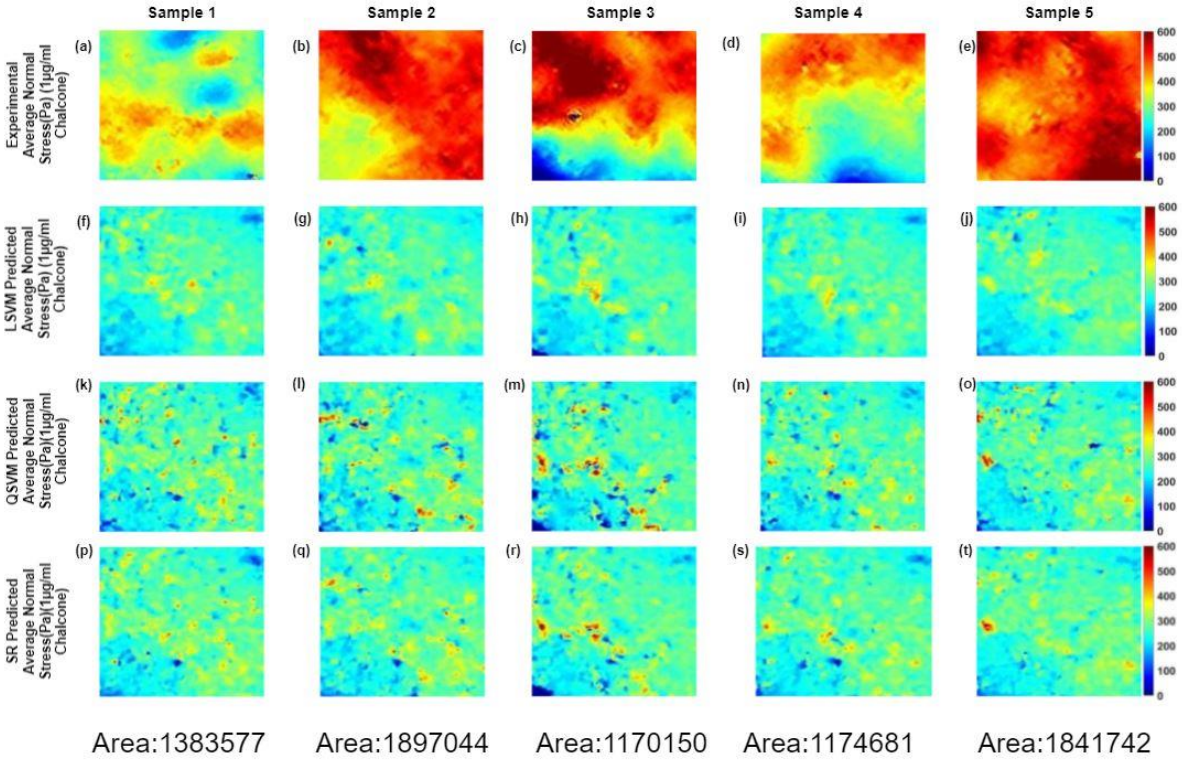

Figure 93: Experimental (a-e) average normal stresses and corresponding LSVM (f-j), and QSVM (k-o), SLR (p-t) predictions utilizing multiple area training sets with monolayer area (Sq.Pixels)

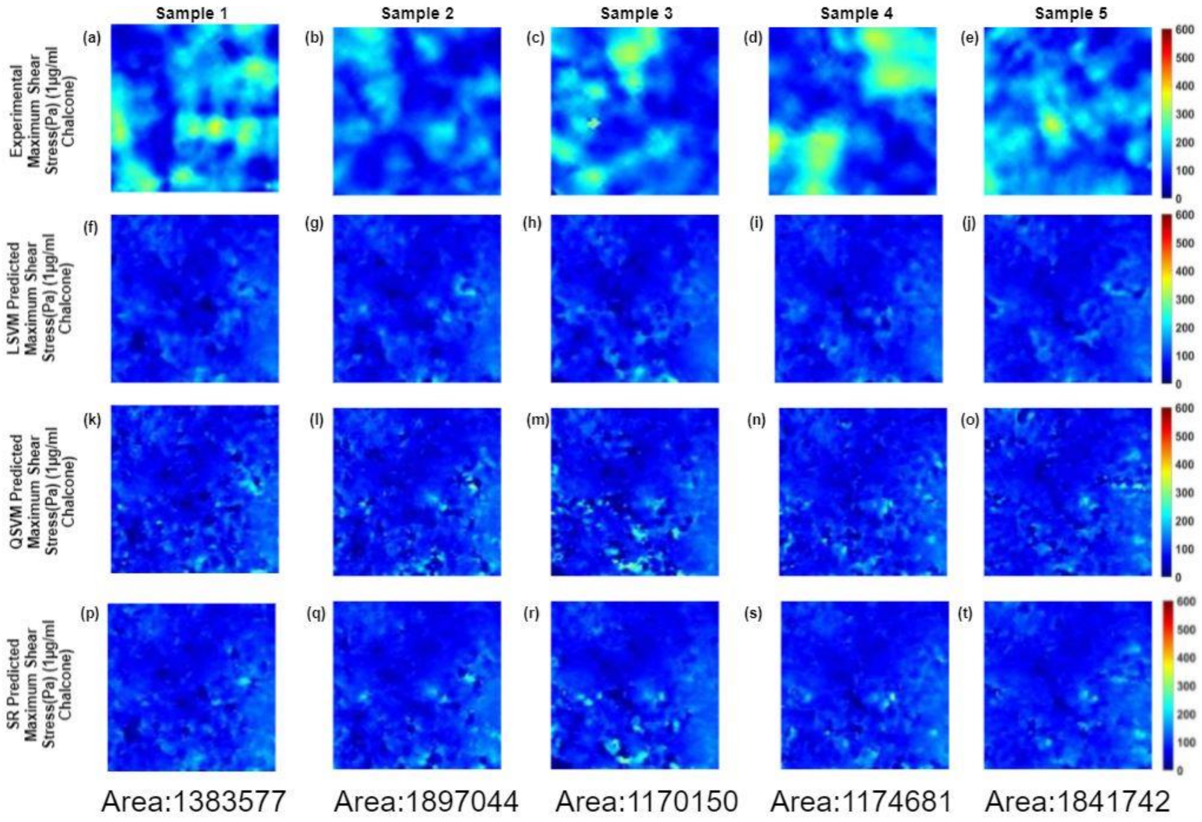

Figure 94: Experimental (a-e) maximum shear stresses and corresponding LSVM (f-j), and QSVM (k-o), SLR (p-t) predictions utilizing multiple area training sets with monolayer area (Sq.Pixels)

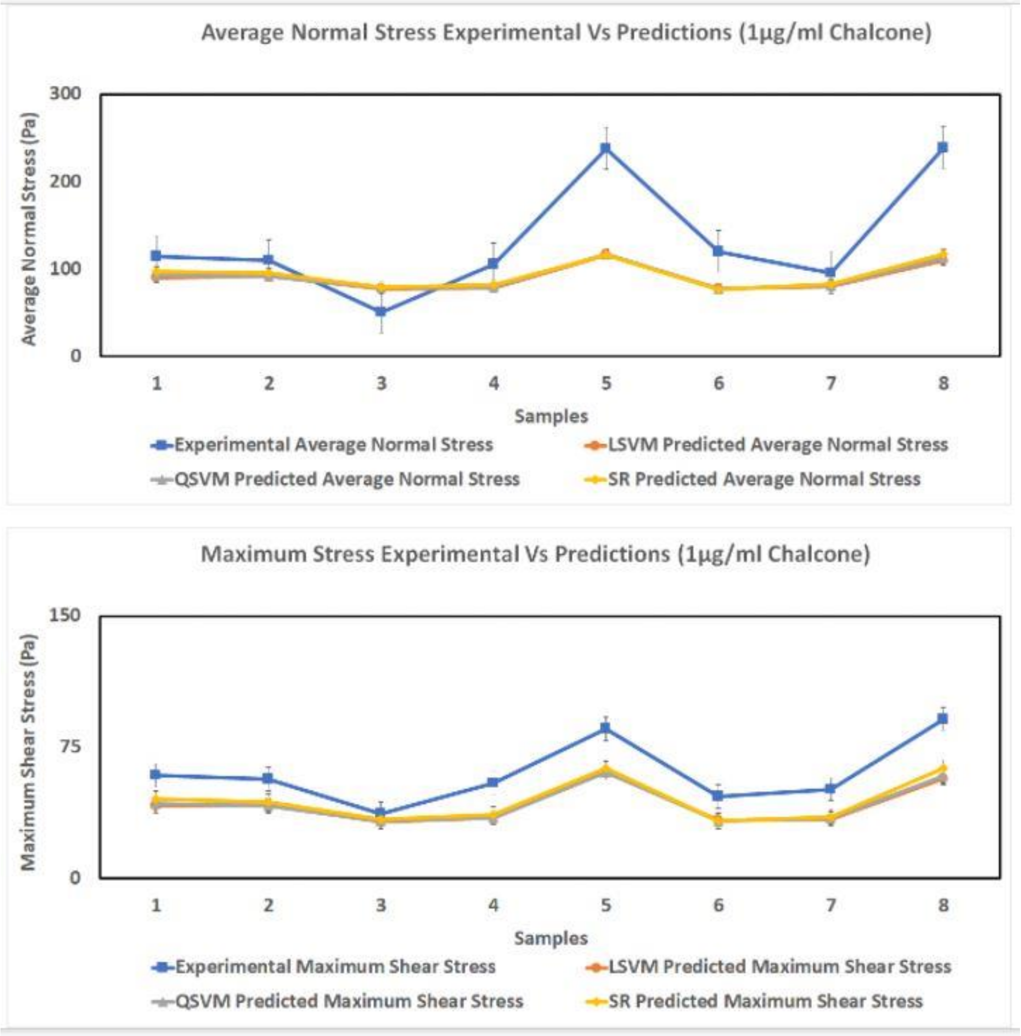

Figure 95: Average experimental results from 8 samples and the corresponding average normal and maximum shear stress predictions using multiple area training sets

Table 7: R and RMSE for QSVM and SLR models utilizing multiple area training sets for 1ug/ml predictions

Avg Normal	**SLR Model**	**QSVM Model**	**LSVM Model**
R	0.897	0.92	0.924
RMSE (Pa)	64.6	66	66.87
Max Shear	**SLR Model**	**QSVM Model**	**LSVM Model**
R	0.967	0.966	0.961
RMSE (Pa)	17.36	19.46	19.84
Max Shear	**SLR Model**	**QSVM Model**	**LSVM Model**
R	0.76	0.785	0.781
RMSE (Pa)	1.56	2.23	2.47

For 1 µg/ml chalcone concentration experiment with 8 samples, R^2 of SLR and QSVM models for average normal stress predictions were 0.70 and 0.73 respectively and for maximum shear stress predictions, R^2 values were 0.78 and 0.86 respectively. The RMSE of SLR and QSVM models were 77.25Pa and 75.15Pa respectively for average normal stress and 15.23Pa and 20.47Pa

respectively for maximum shear intercellular stresses. For RMS tractions, R^2 values were 0.65 and 0.61 for SLR and QSVM with RMSE of 2.05Pa and 4.44Pa respectively.

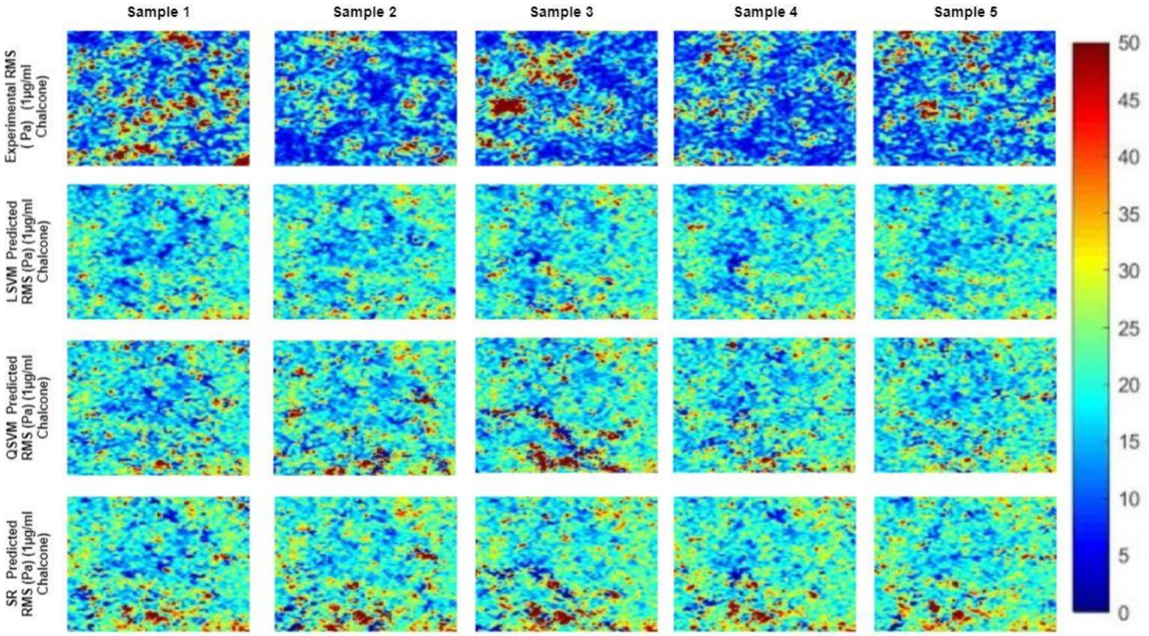

Figure 96: Experimental (a-e) RMS tractions and corresponding LSVM (f-j), and QSVM (k-o), SLR (p-t) predictions utilizing multiple area training sets with monolayer area (Sq.Pixels)

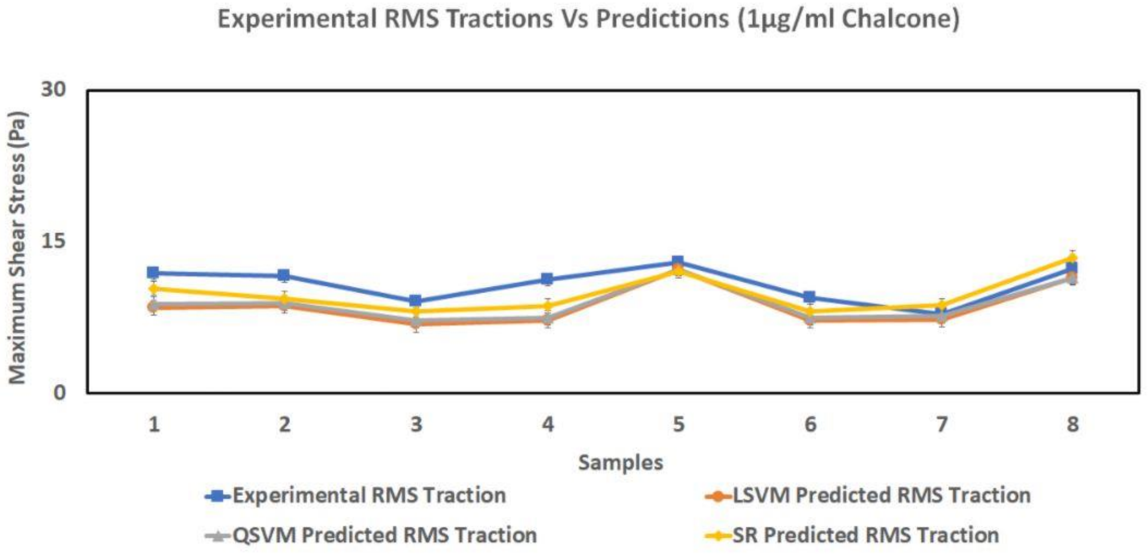

Figure 97: Average experimental results from 8 samples and the corresponding average RMS traction predictions using multiple area training sets

Average (Multiple Area) Training Set Results for 1µg/ml Predictions

For 1 µg/ml chalcone concentration experiment with 8 samples, R^2 of SLR and QSVM models for average normal stress predictions were 0.70 and 0.73 respectively and for maximum shear stress predictions, R^2 values were 0.78 and 0.86 respectively. The RMSE of SLR and QSVM models were 77.25Pa and 75.15Pa respectively for average normal stress and 15.23Pa and 20.47Pa respectively for maximum shear intercellular stresses. For RMS tractions, R^2 values were 0.65 and 0.61 for SLR and QSVM with RMSE of 2.05Pa and 4.44Pa respectively.

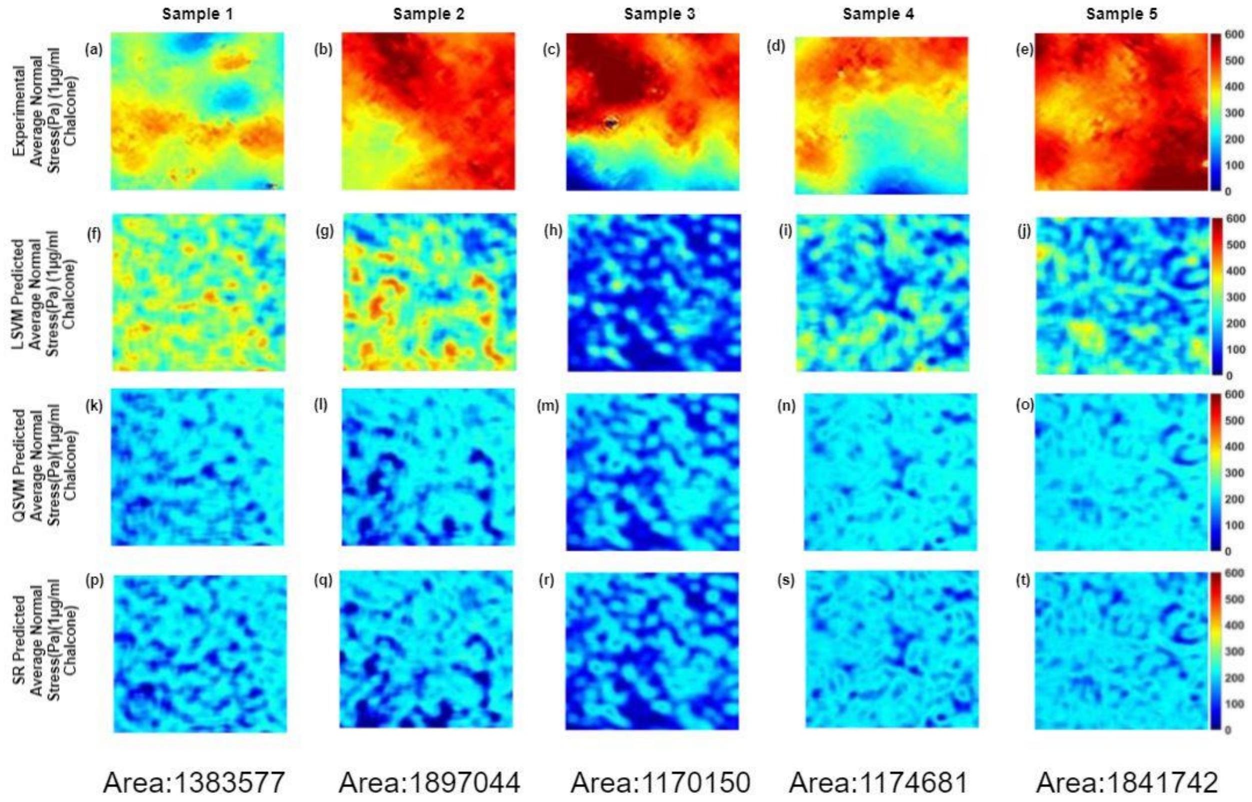

Figure 98: Experimental (a-e) average normal stresses and corresponding LSVM (f-j), and QSVM (k-o), SLR (p-t) predictions utilizing average (multiple area) training sets with monolayer area (Sq.Pixels)

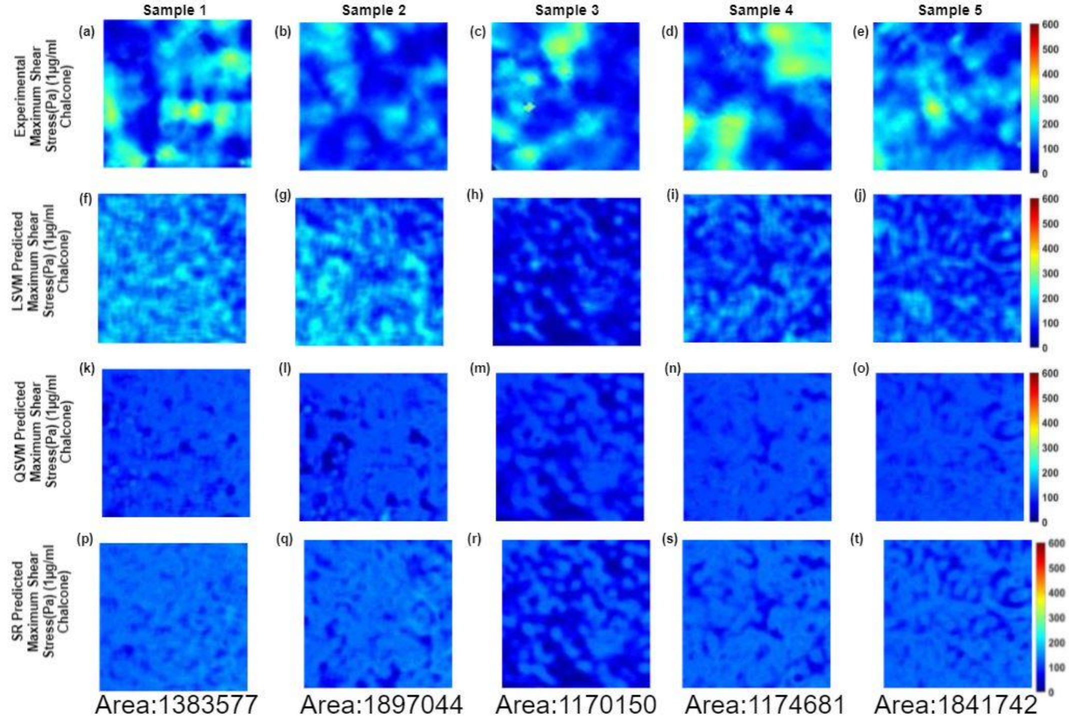

Figure 99: Experimental (a-e) maximum shear stresses and corresponding LSVM (f-j), and QSVM (k-o), SLR (p-t) predictions utilizing average (multiple area) training sets with monolayer area (Sq.Pixels)

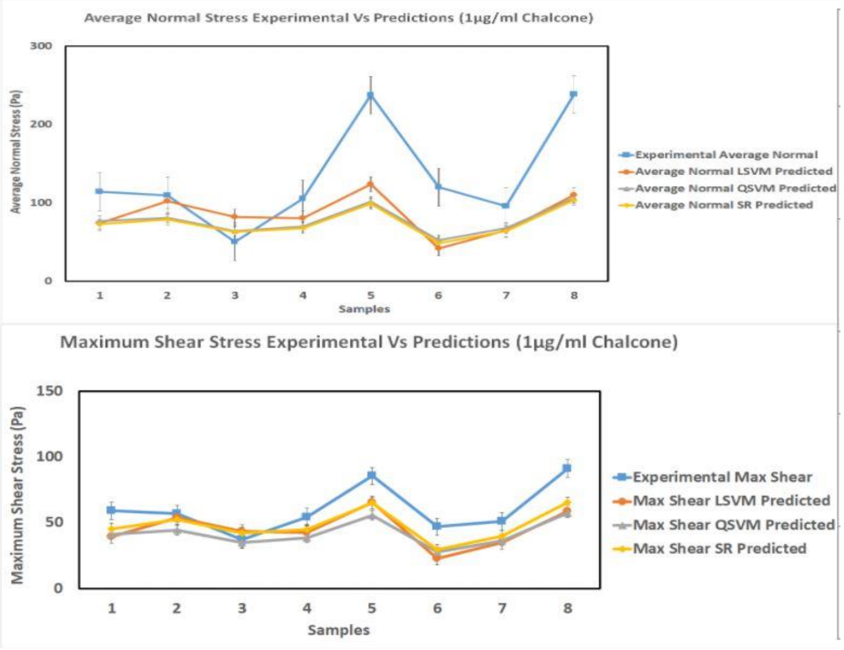

Figure 100: Average experimental results from 8 samples and the corresponding average normal and maximum shear stress predictions using multiple area training sets

Table 8: R and RMSE for QSVM and SLR models utilizing average (multiple area) training sets for 1ug/ml predictions

Avg Normal	**SR Model**	**QSVM Model**	**LSVM Model**
R	0.84	0.85	0.65
RSME	77.25	75.15	70.57
Max Shear	**SR Model**	**QSVM Model**	**LSVM Model**
R	0.88	0.92	0.75
RSME	15.23	20.47	18.94
RMS Traction	**SR Model**	**QSVM Model**	**LSVM Model**
R	0.80	0.78	0.80
RSME	2.05	4.44	4.05

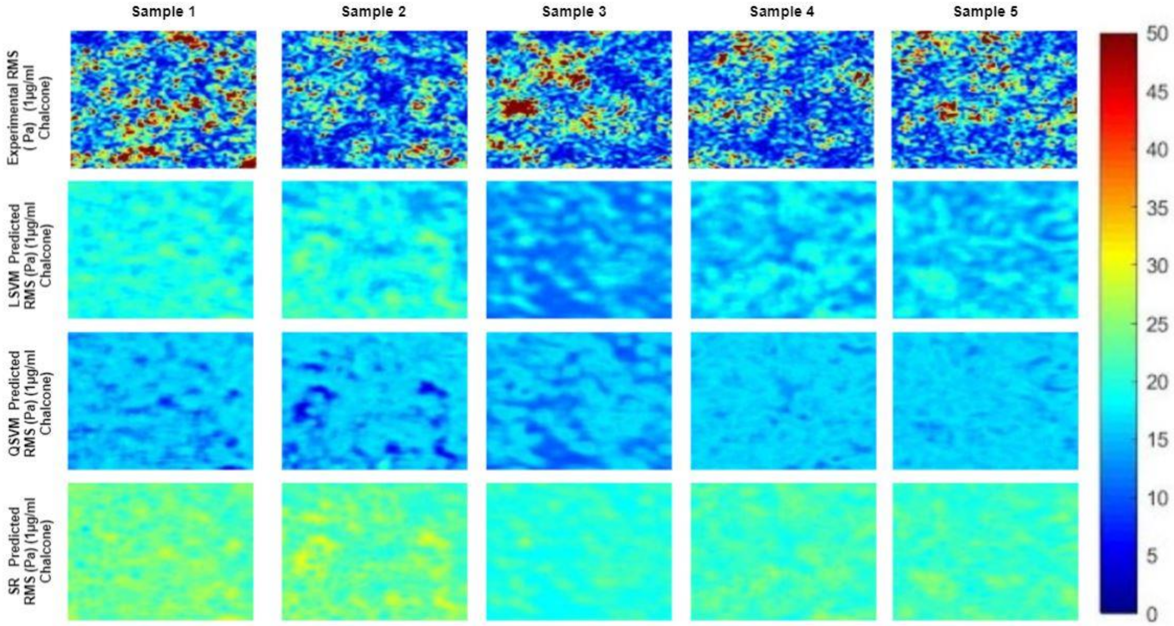

Figure 101: Experimental (a-e) RMS tractions and corresponding LSVM (f-j), and QSVM (k-o), SLR (p-t) predictions utilizing average (multiple area) training sets with monolayer area (Sq.Pixels)

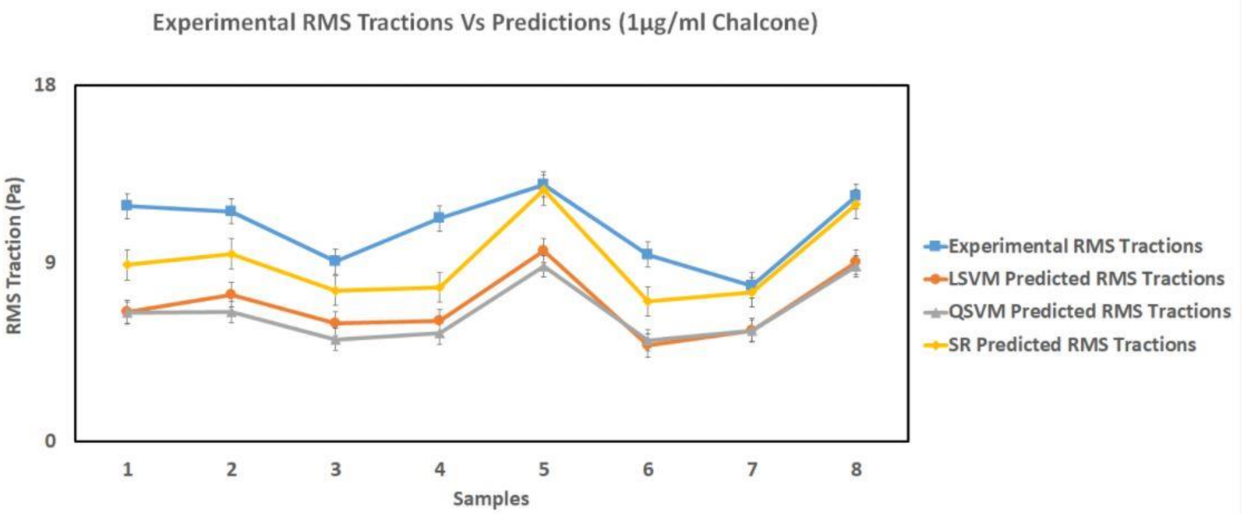

Figure 102: Average experimental results from 8 samples and the corresponding average RMS traction predictions using average (multiple area) training sets

CHAPTER SEVEN: BROADER IMPACTS

Relationship Among ECM Composition, Calcium Signaling, and Cell Mechanics

The changes in ECM composition affect the substrate stiffness which alters the endothelial biomechanics. Stiffening of ECM is associated with many cardiovascular and lung-related diseases [14, 86]. Our results explain how variation in ECM composition alters the endothelial mechanics and morphology. Calcium signaling is linked to nitric oxide release and vasodilation in EC [12]. From the thesis results, the link between intracellular calcium and EC biomechanics could be demystified helping us better understand the complex interaction among ECM, transient calcium, and EC mechanics. This thesis is one of the first attempts to investigate the change in intercellular stresses and other EC mechanics based on ECM composition and transient calcium levels.

Understanding the Influence of External Factors on Cell Mechanics

The proposed machine learning (ML) based prediction methods can investigate the influence of a wide variety of factors on endothelial mechanics. Any new factors such as drug concentration can be added to the existing ML prediction methods by retraining the regression learners with new data. A unified model capable of incorporating a wide variety of microenvironmental, morphological, and biochemical factors to predict the endothelial mechanics can be made possible by utilizing powerful ML-based regression learners. The deployment of ML models could help cut down the number of trials while designing experiments and help study the interaction among different factors affecting cell biomechanics.

Targeted Drug Therapy and Preventive Medicine

Studying the link between substrate composition, endothelial cell-ECM, and cell-cell forces will be helpful in developing and testing more efficient drugs and preventive medicine to counter cardiovascular and other diseases. Results from the studies could be useful in the development of drugs that target cell-cell & cell-ECM junctions and intracellular calcium which are known to regulate endothelial biomechanics and contribute towards alleviating endothelial dysfunction.

Prediction of the Impact of Drugs on Endothelial Mechanics

The impact of different drugs and their corresponding concentrations on cell biomechanics can be studied with ease by utilizing the proposed ML models. The average change in cell mechanics with time owing to different drugs or concentrations can also be estimated with reasonable accuracy. ML models could cut down the number of experiments needed for analysis while giving a comprehensive overview of cell mechanics predictions for various scenarios (change in drug concentration, monolayer shape, etc.) based on the prior information fed to the model.

Extension of Machine Learning Models to 3-D and in vivo Applications

The prediction of traction stresses can be extended to three dimensions using data from 3-D traction force microscopy to train the ML models. A three-dimensional ECM environment is a closer mimicry of cell-cell and cell-ECM interactions in vivo and can act as a more accurate model for quantifying and studying the mechanics of cell clusters.

CHAPTER EIGHT: CONCLUSION AND FUTURE WORK

The research findings demonstrate that TFM & MSM can be powerful tools to investigate the influence of microenvironmental factors (ECM), calcium levels, and drugs on cell mechanics in vitro at the cell-tissue level. Results from the ECM study showed how different concentration ratios of Col-I and FN (ECM compositions) elicited differential endothelial cell mechanical response via tractions, intercellular stresses, cell RMS velocity, and morphological parameters. The future works building on this study include quantifying the endothelial mechanics for more complex ECM compositions mimicking various pathologies or physiological conditions. Shear experiments can be designed to investigate if the differential response was observed and quantitate how fluid shear stresses affect the endothelium mechanics. Investigating the cell dynamics at the protein level can further our understanding of the endothelial mechanics.

The calcium study showed only a very slight increase in traction response to histamine addition which could mean histamine regulates cell mechanics through intercellular stresses rather than tractions at the cell-ECM interface. Maximum RMS tractions were predicted as a function of histamine concentration, cell area, calcium level (% fluorescence) using Regression Learners. Also, high accuracy was observed for classifying high (2mg/ml) and low (1mg/ml) histamine data based on % fluorescence drop in 385nm channel, cell area, and maximum RMS tractions. These results demonstrate the potential of implementing ML models for quantifying cell mechanics.

ML results for the prediction of tractions and intercellular stresses based on chalcone concentration, monolayer geometry, and window-based predictors showed a high correlation to experimental results. The accuracy was higher for QSVM models trained using multiple area sets for intercellular stress predictions. SLR model utilizing multiple area training sets showed the highest accuracy for traction predictions. These promising results showcase the potential of using ML models for quantifying the effect of drugs on endothelial mechanics. The accuracy of the models can be improved by building training sets with more noise-free data and utilizing predictors such as substrate stiffness, cell velocity, cell curvature, cell orientation, cell area, etc. Also, the use of deep learning methods although computationally expensive can increase the accuracy of the predictions along with the addition of the aforementioned new predictors. There is also scope for implementing ML models for predicting tractions and intercellular stresses in 3-Dimensions (x, y, and z).

The upregulation in tractions due to changing ECM properties and calcium levels were linked to higher vascular stiffness and permeability leading to several vascular pathologies such as atherogenesis and hypertension. The research findings presented in this dissertation will be helpful in understanding the dynamics between cell-related mechanical stresses and the cell microenvironment, both of which are important to elucidate the mechanisms of various physiological and pathological processes such as cell proliferation, cell migration, coronary artery disease, and Alzheimer's disease at the mesoscale (cell-tissue level). The cell mechanics studies presented here, along with the proposed machine learning models, have the potential to be helpful in the development and testing of experimental drugs for targeted therapies in the treatment of cerebrovascular and cardiovascular diseases by increasing understanding of the role of cellular mechanical signals in disease progression.

REFERENCES

[1] Y. Gao *et al.*, "The ECM-cell interaction of cartilage extracellular matrix on chondrocytes," (in eng), *Biomed Res Int,* vol. 2014, pp. 648459-648459, 2014, doi: 10.1155/2014/648459.

[2] J. E. Wagenseil and R. P. Mecham, "Elastin in large artery stiffness and hypertension," (in eng), *J Cardiovasc Transl Res,* vol. 5, no. 3, pp. 264-273, 2012, doi: 10.1007/s12265-012-9349-8.

[3] J.-J. Chiu and S. Chien, "Effects of Disturbed Flow on Vascular Endothelium: Pathophysiological Basis and Clinical Perspectives," *Physiological Reviews,* vol. 91, no. 1, pp. 327-387, 2011, doi: 10.1152/physrev.00047.2009.

[4] M.-J. Chow, R. Turcotte, C. P. Lin, and Y. Zhang, "Arterial extracellular matrix: a mechanobiological study of the contributions and interactions of elastin and collagen," (in eng), *Biophysical journal,* vol. 106, no. 12, pp. 2684-2692, 2014, doi: 10.1016/j.bpj.2014.05.014.

[5] Z. Al-Yafeai, A. Yurdagul Jr, J. M. Peretik, M. Alfaidi, P. A. Murphy, and A. W. Orr, "Endothelial FN (Fibronectin) deposition by α5β1 integrins drives atherogenic inflammation," *Arteriosclerosis, thrombosis, and vascular biology,* vol. 38, no. 11, pp. 2601-2614, 2018.

[6] D. Lu and G. S. Kassab, "Role of shear stress and stretch in vascular mechanobiology," *Journal of the royal society interface,* vol. 8, no. 63, pp. 1379-1385, 2011.

[7] R. Amaya, A. Pierides, and J. M. Tarbell, "The interaction between fluid wall shear stress and solid circumferential strain affects endothelial gene expression," *PloS one,* vol. 10, no. 7, p. e0129952, 2015.

[8] S. Löffek, O. Schilling, and C.-W. Franzke, "Biological role of matrix metalloproteinases: a critical balance," *European Respiratory Journal,* vol. 38, no. 1, pp. 191-208, 2011.

[9] J. B. Su, "Vascular endothelial dysfunction and pharmacological treatment," *World journal of cardiology,* vol. 7, no. 11, p. 719, 2015.

[10] H. Haybar, S. Shahrabi, H. Rezaeeyan, R. Shirzad, and N. Saki, "Endothelial cells: from dysfunction mechanism to pharmacological effect in cardiovascular disease," *Cardiovascular Toxicology,* vol. 19, no. 1, pp. 13-22, 2019.

[11] B. Blaus, "Medical gallery of Blausen medical 2014," *Wiki J. Med,* vol. 1, no. 10, 2014.

[12] J. Ando and K. Yamamoto, "Vascular mechanobiology," *Circulation Journal,* vol. 73, no. 11, pp. 1983-1992, 2009.

[13] D. J. McGrail, Q. M. N. Kieu, and M. R. Dawson, "The malignancy of metastatic ovarian cancer cells is increased on soft matrices through a mechanosensitive Rho–ROCK pathway," *Journal of cell science,* vol. 127, no. 12, pp. 2621-2626, 2014.

[14] D. Ingber, "Mechanobiology and diseases of mechanotransduction," *Annals of medicine,* vol. 35, no. 8, pp. 564-577, 2003.

[15] R. Zielinski, C. Mihai, D. Kniss, and S. N. Ghadiali, "Finite element analysis of traction force microscopy: influence of cell mechanics, adhesion, and morphology," *Journal of biomechanical engineering,* vol. 135, no. 7, 2013.

[16] R. Ananthakrishnan and A. Ehrlicher, "The forces behind cell movement," (in eng), *Int J Biol Sci,* vol. 3, no. 5, pp. 303-317, 2007, doi: 10.7150/ijbs.3.303.

[17] L. Kurzawa, B. Vianay, F. Senger, T. Vignaud, L. Blanchoin, and M. Théry, "Dissipation of contractile forces: the missing piece in cell mechanics," *Molecular biology of the cell,* vol. 28, no. 14, pp. 1825-1832, 2017.

[18] G. Patel *et al.*, "Mechanical signaling in a pulmonary microvascular endothelial cell monolayer," *Biochemical and biophysical research communications,* vol. 519, no. 2, pp. 337-343, 2019.

[19] P. W. Oakes *et al.*, "Lamellipodium is a myosin-independent mechanosensor," *Proceedings of the National Academy of Sciences,* vol. 115, no. 11, pp. 2646-2651, 2018.

[20] S. J. Han, K. S. Bielawski, L. H. Ting, M. L. Rodriguez, and N. J. Sniadecki, "Decoupling substrate stiffness, spread area, and micropost density: a close spatial relationship between traction forces and focal adhesions," *Biophysical journal,* vol. 103, no. 4, pp. 640-648, 2012.

[21] C. F. Soon, K. S. Tee, M. Youseffi, and M. C. Denyer, "Tracking traction force changes of single cells on the liquid crystal surface," *Biosensors,* vol. 5, no. 1, pp. 13-24, 2015.

[22] X. Trepat *et al.*, "Physical forces during collective cell migration," *Nature physics,* vol. 5, no. 6, pp. 426-430, 2009.

[23] R. W. Kobs and N. C. Chesler, "The mechanobiology of pulmonary vascular remodeling in the congenital absence of eNOS," (in eng), *Biomech Model Mechanobiol,* vol. 5, no. 4, pp. 217-25, Nov 2006, doi: 10.1007/s10237-006-0018-1.

[24] S. Bao *et al.*, "Stem cell–like glioma cells promote tumor angiogenesis through vascular endothelial growth factor," *Cancer research,* vol. 66, no. 16, pp. 7843-7848, 2006.

[25] J. H. Kim *et al.*, "Propulsion and navigation within the advancing monolayer sheet," *Nature materials,* vol. 12, no. 9, pp. 856-863, 2013.

[26] B. Ladoux and R.-M. Mège, "Mechanobiology of collective cell behaviours," *Nature reviews Molecular cell biology,* vol. 18, no. 12, pp. 743-757, 2017.

[27] A. F. Pegoraro, J. J. Fredberg, and J.-A. Park, "Problems in biology with many scales of length: Cell–cell adhesion and cell jamming in collective cellular migration," *Experimental cell research,* vol. 343, no. 1, pp. 54-59, 2016.

[28] P. Laurila and I. Leivo, "Basement membrane and interstitial matrix components form separate matrices in heterokaryons of PYS-2 cells and fibroblasts," *Journal of cell science,* vol. 104, no. 1, pp. 59-68, 1993.

[29] C.-M. Lo, H.-B. Wang, M. Dembo, and Y.-l. Wang, "Cell movement is guided by the rigidity of the substrate," *Biophysical journal,* vol. 79, no. 1, pp. 144-152, 2000.

[30] R. Krishnan *et al.*, "Substrate stiffening promotes endothelial monolayer disruption through enhanced physical forces," *American Journal of Physiology-Cell Physiology,* vol. 300, no. 1, pp. C146-C154, 2011.

[31] S. Wang, R. Chennupati, H. Kaur, A. Iring, N. Wettschureck, and S. Offermanns, "Endothelial cation channel PIEZO1 controls blood pressure by mediating flow-induced ATP release," *The Journal of Clinical Investigation,* vol. 126, no. 12, pp. 4527-4536, 12/01/ 2016, doi: 10.1172/JCI87343.

[32] A. Doyle, W. Marganski, and J. Lee, "Calcium transients induce spatially coordinated increases in traction force during the movement of fish keratocytes," *Journal of Cell Science,* vol. 117, no. 11, pp. 2203-2214, 2004.

[33] L. M. Worthen and M. U. Nollert, "Intracellular calcium response of endothelial cells exposed to flow in the presence of thrombin or histamine," *Journal of vascular surgery,* vol. 32, no. 3, pp. 593-601, 2000.

[34] M. Junkin, Y. Lu, J. Long, P. A. Deymier, J. B. Hoying, and P. K. Wong, "Mechanically induced intercellular calcium communication in confined endothelial structures," *Biomaterials,* vol. 34, no. 8, pp. 2049-2056, 2013.

[35] M. Islam and R. Steward, "Probing endothelial cell mechanics through connexin 43 disruption," *Experimental Mechanics,* vol. 59, no. 3, pp. 327-336, 2019.

[36] J. H. C. Wang and J.-S. Lin, "Cell traction force and measurement methods," *Biomechanics and Modeling in Mechanobiology,* vol. 6, no. 6, p. 361, 2007/01/03 2007, doi: 10.1007/s10237-006-0068-4.

[37] C. Gayrard and N. Borghi, "FRET-based Molecular Tension Microscopy," *Methods,* vol. 94, pp. 33-42, 2016/02/01/ 2016, doi: https://doi.org/10.1016/j.ymeth.2015.07.010.

[38] J. P. Butler, I. M. Tolic-Nørrelykke, B. Fabry, and J. J. Fredberg, "Traction fields, moments, and strain energy that cells exert on their surroundings," *American Journal of Physiology-Cell Physiology,* vol. 282, no. 3, pp. C595-C605, 2002.

[39] N. Bonakdar. "TRACTION FORCE MICROSCOPY." http://www.cellmechanics.de/Methods/Tractions.html

(accessed.

[40] X. Trepat and J. J. Fredberg, "Plithotaxis and emergent dynamics in collective cellular migration," *Trends in Cell Biology,* vol. 21, no. 11, pp. 638-646, 2011/11/01/ 2011, doi: https://doi.org/10.1016/j.tcb.2011.06.006.

[41] D. T. Tambe *et al.*, "Monolayer stress microscopy: limitations, artifacts, and accuracy of recovered intercellular stresses," *PloS one,* vol. 8, no. 2, p. e55172, 2013.

[42] P. W. Oakes, S. Banerjee, M. C. Marchetti, and M. L. Gardel, "Geometry regulates traction stresses in adherent cells," *Biophysical journal,* vol. 107, no. 4, pp. 825-833, 2014.

[43] K. Ghosh *et al.*, "Cell adaptation to a physiologically relevant ECM mimic with different viscoelastic properties," *Biomaterials,* vol. 28, no. 4, pp. 671-679, 2007.

[44] J. P. Califano and C. A. Reinhart-King, "Substrate stiffness and cell area predict cellular traction stresses in single cells and cells in contact," *Cellular and molecular bioengineering,* vol. 3, no. 1, pp. 68-75, 2010.

[45] K. K. Parker *et al.*, "Directional control of lamellipodia extension by constraining cell shape and orienting cell tractional forces," *The FASEB journal,* vol. 16, no. 10, pp. 1195-1204, 2002.

[46] A. D. Rape, W.-h. Guo, and Y.-l. Wang, "The regulation of traction force in relation to cell shape and focal adhesions," *Biomaterials,* vol. 32, no. 8, pp. 2043-2051, 2011.

[47] C. A. Lemmon and L. H. Romer, "A predictive model of cell traction forces based on cell geometry," *Biophysical journal,* vol. 99, no. 9, pp. L78-L80, 2010.

[48] L. Giomi, "Contour models of cellular adhesion," in *Cell Migrations: Causes and Functions*: Springer, 2019, pp. 13-29.

[49] V. Nier, S. Jain, Chwee T. Lim, S. Ishihara, B. Ladoux, and P. Marcq, "Inference of Internal Stress in a Cell Monolayer," *Biophysical Journal,* vol. 110, no. 7, pp. 1625-1635, 2016/04/12/ 2016, doi: https://doi.org/10.1016/j.bpj.2016.03.002.

[50] V. Nier, G. Peyret, J. d’Alessandro, S. Ishihara, B. Ladoux, and P. Marcq, "Kalman Inversion Stress Microscopy," *Biophysical Journal,* vol. 115, no. 9, pp. 1808-1816, 2018/11/06/ 2018, doi: https://doi.org/10.1016/j.bpj.2018.09.013.

[51] M. Dembo and Y.-L. Wang, "Stresses at the cell-to-substrate interface during locomotion of fibroblasts," *Biophysical journal,* vol. 76, no. 4, pp. 2307-2316, 1999.

[52] H. S. Sonbol, "Extracellular matrix remodeling in human disease," *Journal of microscopy and ultrastructure,* vol. 6, no. 3, p. 123, 2018.

[53] Y. Huang and T. R. Kyriakides, "The role of extracellular matrix in the pathophysiology of diabetic wounds," *Matrix Biology Plus,* vol. 6, p. 100037, 2020.

[54] P. Lu, K. Takai, V. M. Weaver, and Z. Werb, "Extracellular matrix degradation and remodeling in development and disease," *Cold Spring Harbor perspectives in biology,* vol. 3, no. 12, p. a005058, 2011.

[55] G. E. Davis and D. R. Senger, "Endothelial Extracellular Matrix," *Circulation Research,* vol. 97, no. 11, pp. 1093-1107, 2005, doi: doi:10.1161/01.RES.0000191547.64391.e3.

[56] D. Tambe *et al.*, "Collective cell guidance by cooperative intercellular forces," *Nature materials,* vol. 10, pp. 469 - 475, 2011.

[57] R. Steward, Jr., D. Tambe, C. C. Hardin, R. Krishnan, and J. J. Fredberg, "Fluid shear, intercellular stress, and endothelial cell alignment," (in eng), *Am J Physiol Cell Physiol,* vol. 308, no. 8, pp. C657-64, Apr 15 2015, doi: 10.1152/ajpcell.00363.2014.

[58] K. M. Stroka and H. Aranda-Espinoza, "Endothelial cell substrate stiffness influences neutrophil transmigration via myosin light chain kinase-dependent cell contraction," *Blood,* vol. 118, no. 6, pp. 1632-1640, 2011, doi: 10.1182/blood-2010-11-321125.

[59] R. L. Steward, Jr., C. M. Cheng, D. L. Wang, and P. R. LeDuc, "Probing cell structure responses through a shear and stretching mechanical stimulation technique," (in eng), *Cell Biochem Biophys,* vol. 56, no. 2-3, pp. 115-24, Apr 2010, doi: 10.1007/s12013-009-9075-2.

[60] M. H. Jorrisch, W. Shih, and S. Yamada, "Myosin IIA deficient cells migrate efficiently despite reduced traction forces at cell periphery," *Biology Open,* vol. 2, no. 4, pp. 368-372, 2013, doi: 10.1242/bio.20133707.

[61] Y.-T. Shiu *et al.*, "Rho Mediates the Shear-Enhancement of Endothelial Cell Migration and Traction Force Generation," *Biophysical Journal,* vol. 86, no. 4, pp. 2558-2565, 2004/04/01/ 2004, doi: https://doi.org/10.1016/S0006-3495(04)74311-8.

[62] K. E. Kubow *et al.*, "Mechanical forces regulate the interactions of fibronectin and collagen I in extracellular matrix," *Nature Communications,* vol. 6, no. 1, p. 8026, 2015/08/14 2015, doi: 10.1038/ncomms9026.

[63] M. Lin *et al.*, "Adsorption force of fibronectin controls transmission of cell traction force and subsequent stem cell fate," *Biomaterials,* vol. 162, pp. 170-182, 2018/04/01/ 2018, doi: https://doi.org/10.1016/j.biomaterials.2018.01.036.

[64] D. E. Clapham, "Calcium signaling," *Cell,* vol. 131, no. 6, pp. 1047-1058, 2007.

[65] L. I. Brueggemann, B. L. Martin, J. Barakat, K. L. Byron, and L. L. Cribbs, "Low voltage-activated calcium channels in vascular smooth muscle: T-type channels and AVP-stimulated calcium spiking," *American Journal of Physiology-Heart and Circulatory Physiology,* vol. 288, no. 2, pp. H923-H935, 2005, doi: 10.1152/ajpheart.01126.2003.

[66] M. F. Rossier, "T-Type Calcium Channel: A Privileged Gate for Calcium Entry and Control of Adrenal Steroidogenesis," (in English), *Frontiers in Endocrinology,* Review vol. 7, no. 43, 2016-May-20 2016, doi: 10.3389/fendo.2016.00043.

[67] R. Sandoval, A. B. Malik, R. D. Minshall, P. Kouklis, C. A. Ellis, and C. Tiruppathi, "Ca2+ signalling and PKCα activate increased endothelial permeability by disassembly of VE—cadherin junctions," *The Journal of physiology,* vol. 533, no. 2, pp. 433-445, 2001.

[68] D. D. MILLER, D. A. CALLAHAM, D. J. GROSS, and P. K. HEPLER, "Free Ca2+ gradient in growing pollen tubes of Lillium," *Journal of Cell Science,* vol. 101, no. 1, pp. 7-12, 1992.

[69] J. M. Dickenson and S. Hill, "Histamine H1-receptor-mediated calcium influx in DDT1MF-2 cells," *Biochemical Journal,* vol. 284, no. 2, pp. 425-431, 1992.

[70] B. Pfanzagl, V. F. Zevallos, D. Schuppan, R. Pfragner, and E. Jensen-Jarolim, "Histamine causes influx via T-type voltage-gated calcium channels in an enterochromaffin tumor cell line: potential therapeutic target in adverse food reactions," *American Journal of Physiology-Gastrointestinal and Liver Physiology,* vol. 316, no. 2, pp. G291-G303, 2019, doi: 10.1152/ajpgi.00261.2018.

[71] A. B. Ebeigbe and O. O. Talabi, "Vascular effects of histamine," *Nigerian Journal of Physiological Sciences,* vol. 29, no. 1, pp. 07–10-07–10, 2014.

[72] N. Prasain and T. Stevens, "The actin cytoskeleton in endothelial cell phenotypes," (in eng), *Microvasc Res,* vol. 77, no. 1, pp. 53-63, 2009, doi: 10.1016/j.mvr.2008.09.012.

[73] N. Z. Wu and A. L. Baldwin, "Transient venular permeability increase and endothelial gap formation induced by histamine," *American Journal of Physiology-Heart and Circulatory Physiology,* vol. 262, no. 4, pp. H1238-H1247, 1992.

[74] A. B. Moy *et al.*, "Histamine alters endothelial barrier function at cell-cell and cell-matrix sites," *American Journal of Physiology-Lung Cellular and Molecular Physiology,* vol. 278, no. 5, pp. L888-L898, 2000, doi: 10.1152/ajplung.2000.278.5.L888.

[75] M. Guo, J. W. Breslin, M. H. Wu, C. J. Gottardi, and S. Y. Yuan, "VE-cadherin and β-catenin binding dynamics during histamine-induced endothelial hyperpermeability," *American Journal of Physiology-Cell Physiology,* vol. 294, no. 4, pp. C977-C984, 2008, doi: 10.1152/ajpcell.90607.2007.

[76] B. Srinivasan, A. R. Kolli, M. B. Esch, H. E. Abaci, M. L. Shuler, and J. J. Hickman, "TEER measurement techniques for in vitro barrier model systems," (in eng), *J Lab Autom,* vol. 20, no. 2, pp. 107-126, 2015, doi: 10.1177/2211068214561025.

[77] Z. M. Goeckeler and R. B. Wysolmerski, "Myosin light chain kinase-regulated endothelial cell contraction: the relationship between isometric tension, actin polymerization, and myosin phosphorylation," (in eng), *J Cell Biol,* vol. 130, no. 3, pp. 613-27, Aug 1995, doi: 10.1083/jcb.130.3.613.

[78] G. Grynkiewicz, M. Poenie, and R. Y. Tsien, "A new generation of Ca2+ indicators with greatly improved fluorescence properties," *Journal of biological chemistry,* vol. 260, no. 6, pp. 3440-3450, 1985.

[79] W. Henke, C. Cetinsoy, K. Jung, and S. Loening, "Nonmhyperbolic calcium calibration curve of Fura-2: implications for the reliability of quantitative Ca2+ measurements," *Cell Calcium,* vol. 20, no. 3, pp. 287-292, 1996.

[80] C. Kummerow, C. Backes, M. Hoth, and C. Schwindling, "Fura-2 Based Calcium-Imaging Using ZEISS Colibri LED Illumination," *Carl Zeiss Microscopy GmbH,* Technology Note October 2015 2015. [Online]. Available: http://www.zeiss.com/microscopy.

[81] S. U. Kim and J. de Vellis, "Stem cell-based cell therapy in neurological diseases: A review," *Journal of Neuroscience Research,* vol. 87, no. 10, pp. 2183-2200, 2009, doi: https://doi.org/10.1002/jnr.22054.

[82] D. D. Deshpande, D. R. Janero, and M. M. Amiji, "Therapeutic strategies for endothelial dysfunction," *Expert opinion on biological therapy,* vol. 11, no. 12, pp. 1637-1654, 2011.

[83] A. Raj. "Unlocking the True Power of Support Vector Regression." https://towardsdatascience.com/unlocking-the-true-power-of-support-vector-regression-847fd123a4a0#:~:text=Support%20Vector%20Regression%20is%20a,the%20maximum%20number%20of%20points (accessed October 3, 2020.

[84] M. Lewis, "Stepwise versus Hierarchical Regression: Pros and Cons," *Online Submission,* 2007.

[85] S. Sayad. "Support Vector Machine - Regression (SVR)." https://www.saedsayad.com/support_vector_machine_reg.htm (accessed.

[86] G. Burgstaller, B. Oehrle, M. Gerckens, E. S. White, H. B. Schiller, and O. Eickelberg, "The instructive extracellular matrix of the lung: basic composition and alterations in chronic lung disease," (in eng), *Eur Respir J,* vol. 50, no. 1, Jul 2017, doi: 10.1183/13993003.01805-2016.